Development of a Strategy for Simulating Blast-Vehicle Interactions

D. Thompson, E. Luke, J.C. Newman III, J. Mark Janus, E. Blades, X. Tong, and C. Moore
Center for Advanced Vehicular Systems
Mississippi State University
Mississippi State, MS

and

J. Kang
U.S. Army RDECOM-TARDEC
Warren, MI

September 2010

Report Documentation Page

Form Approved
OMB No. 0704-0188

1. REPORT DATE	2. REPORT TYPE	3. DATES COVERED
01 SEP 2010	**N/A**	**-**

4. TITLE AND SUBTITLE	5a. CONTRACT NUMBER
Development of a Strategy for Simulating Blast-Vehicle Interactions	**W56HZV-08-C-0126**
	5b. GRANT NUMBER
	5c. PROGRAM ELEMENT NUMBER
6. AUTHOR(S)	5d. PROJECT NUMBER
D. Thompson; E. Luke; J.C. Newman III; J. Mark Janus; E. Blades; X. Tong; C. Moore;	5e. TASK NUMBER
	5f. WORK UNIT NUMBER
7. PERFORMING ORGANIZATION NAME(S) AND ADDRESS(ES)	8. PERFORMING ORGANIZATION REPORT NUMBER
Center for Advanced Vehicular Systems Mississippi State University Mississippi State, MS US Army RDECOM-TARDEC 6501 E 11 Mile Rd Warren, MI 48397-5000, USA	**21200RC**
9. SPONSORING/MONITORING AGENCY NAME(S) AND ADDRESS(ES)	10. SPONSOR/MONITOR'S ACRONYM(S)
US Army RDECOM-TARDEC 6501 E 11 Mile Rd Warren, MI 48397-5000, USA	**TACOM/TARDEC**
	11. SPONSOR/MONITOR'S REPORT NUMBER(S) **21200RC**

12. DISTRIBUTION/AVAILABILITY STATEMENT
Approved for public release, distribution unlimited

13. SUPPLEMENTARY NOTES
The original document contains color images.

14. ABSTRACT

This report describes research and development activities supported by contract W56HZV-08-C-0126, which was funded under the SimBRS program, to develop a strategy to perform high-fidelity simulations of blast-vehicle interactions including complex phenomena such as detonation, coupled fluid-structure interactions, and non-linear structural response to severe, time-dependent pressure loads and debris impact. The contract leveraged ongoing development efforts for the high-fidelity flow solver Loci/CHEM to produce a fully Eulerian numerical capability to simulate blast phenomena in fluids and solids. The resulting code was christened Loci/BLAST. Included in this report are: an assessment of existing technology; a discussion of the implementation of the Jones-Wilkins-Lee equation of state and a prescribed burn function within Loci/BLAST; results from simulations of blast interactions with realistic rigid geometries; a discussion of the implementation of the models needed to simulate blast-soil interactions within Loci/BLAST and the associated validation activities; results from simulations of blast interactions with debris; and preliminary results from coupled fluid-structure interaction simulations using Loci/BLAST and LS-DYNA. The results reported here demonstrate that it is possible to perform blast simulations, including both fluids and solids, within a unified Eulerian framework. These results lay the groundwork for the new strategy that is described in the report.

15. SUBJECT TERMS

16. SECURITY CLASSIFICATION OF:			17. LIMITATION OF ABSTRACT	18. NUMBER OF PAGES	19a. NAME OF RESPONSIBLE PERSON
a. REPORT **unclassified**	b. ABSTRACT **unclassified**	c. THIS PAGE **unclassified**	**SAR**	**140**	

Standard Form 298 (Rev. 8-98)
Prescribed by ANSI Std Z39-18

Abstract

This report describes research and development activities supported by contract W56HZV-08-C-0126, which was funded under the SimBRS program, to develop a strategy to perform high-fidelity simulations of blast-vehicle interactions including complex phenomena such as detonation, coupled fluid-structure interactions, and non-linear structural response to severe, time-dependent pressure loads and debris impact. The contract leveraged ongoing development efforts for the high-fidelity flow solver Loci/CHEM to produce a fully Eulerian numerical capability to simulate blast phenomena in fluids and solids. The resulting code was christened Loci/BLAST. Included in this report are: an assessment of existing technology; a discussion of the implementation of the Jones-Wilkins-Lee equation of state and a prescribed burn function within Loci/BLAST; results from simulations of blast interactions with realistic rigid geometries; a discussion of the implementation of the models needed to simulate blast-soil interactions within Loci/BLAST and the associated validation activities; results from simulations of blast interactions with debris; and preliminary results from coupled fluid-structure interaction simulations using Loci/BLAST and LS-DYNA. The results reported here demonstrate that it is possible to perform blast simulations, including both fluids and solids, within a unified Eulerian framework. These results lay the groundwork for the new strategy that is described in the report.

Table of Contents

List of Figures

List of Tables

Section 1: Introduction and literature review

Predicting blast-vehicle interactions is a daunting task. Typically, extensive experimental testing is performed, utilizing obsolete or damaged vehicles, thereby precluding an accurate indication of blast response for vehicles currently deployed in the field. As an alternative, numerical simulation can be employed to predict these interactions. The fidelity of the numerical simulations can vary from hydrocode simulations to decoupled Computational Fluid Dynamics (CFD) and Computational Structural Dynamics (CSD) simulations to fully-coupled fluid structure CFD/CSD simulations.

This report describes research and development activities supported by contract W56HZV-08-C-0126, which was funded under the SimBRS program, to develop a strategy to perform high-fidelity simulations of blast-vehicle interactions, including complex phenomena such as detonation, coupled fluid-structure interactions, and non-linear structural response to severe, time-dependent pressure loads and debris impact. This effort leveraged ongoing development efforts for the high-fidelity flow solver Loci/CHEM to produce a fully Eulerian numerical capability to simulate blast phenomena in fluids and solids. The resulting code was christened Loci/BLAST. Included in this report are the following: an assessment of existing technology; a discussion of the implementation of the Jones-Wilkins-Lee equation of state and a prescribed burn model within Loci/BLAST; results from simulations of blast interactions with realistic rigid geometries; a discussion of the implementation of the models needed to simulate blast-soil interactions within Loci/BLAST and the associated validation activities; results from simulations of blast interactions with debris; and preliminary results from coupled fluid-structure interaction simulations using Loci/BLAST and LS-DYNA. The remainder of this section consists of a review of the state-of-the-art in several blast-related topic areas.

1.1 Blast wave interactions with vehicles and structures

Simulations for simple and complex geometries

In designing new armored vehicle concepts, protection against landmine explosions is of utmost importance. The level of mine protection and occupant safety largely defines the vehicle structure and configuration of the crew compartment. Therefore, determination of the pressure loads applied to the vehicle structure is a necessary first step in the design of protective measures for vehicles.

Computing the pressure loading and determining the structural response is a demanding task requiring the use of numerical simulations. The numerical simulations can vary from hydrocode simulations to decoupled Computational Fluid Dynamics (CFD) and Computational Structural Dynamics (CSD) simulations to fully-coupled fluid structure CFD/CSD simulations.

Numerous experimental and numerical blast simulations have been conducted using a simplified geometry consisting of a plate structure [Gupta, 1999, Gupta, 2001, Jacinto et al., 2002]. Showichen et al. [Showichen et al., 2005] simulated the response of a plate to an anti-tank blast using LS-DYNA. The loading was computed using CONWEP [Hyde, 1991], which provides semi-empirical blast loading functions produced by a variety of weapon configurations. Kambouchev et al. [Kambouchev et al., 2006, Kambouchev et al., 2007a, Kambouchev et al., 2007b] examined the influence of the fluid-structure interaction in the dynamic response of a

plate subject to blast loading. The understanding developed through these types of analyses is crucial for modeling more complex structures.

Löhner et al. [Löhner et al., 2008] described methods for handling geometrically complex, body-fitted, unstructured grids that contain embedded surfaces and immersed bodies. These methods allow for fluid-structure interaction, i.e. CSD/CFD coupling, using unstructured flow solvers. Examples include the interaction of an explosion with a generic ship hull and a generic weapon fragmentation. Tai et al. [Tai et al., 2007b] presented a similar method, referred to as the immersed object method, for flows around multiple bodies with overlapping, unstructured grids. Swensen et al. [Swensen et al., 2006] described a blast computational framework for performing simulations of soil bound explosion and their effects on vehicles and their human occupants. The framework couples the MPMICE CFD code with DYNA3D and LS-DYNA finite element codes.

Simulations for buildings and urban environments

Simulations to predict blast loadings on buildings and urban environments have also been conducted where the buildings are represented by simple geometric shapes [Smith et al., 2000, Xu and Lu, 2006]. Remennikov [Remennikov and Rose, 2005] modeled a blast load in an urban environment using an uncoupled analysis with buildings modeled as rigid blocks and plates. A decoupled CFD code was used to determine blast loads on the buildings. Hayhurst et al. [Hayhurst et al., 1996] simulated a vapor cloud explosion of an onshore petro-chemical plant using a CFD code. The plant equipment consisted of a large number of vessels, pumps, piping, and other apparatus. The geometrical entities consisted of simple primitives. In addition, a simulated detonation of an explosive in a storage building, using the hydrocode AUTODYN-3D, demonstrated explosions for storage areas with a common roof, fixed walls, and a relocatable sliding wall, with all walls represented as plates. Rose et al. [Rose et al., 2005b, Rose et al., 2005a] performed an explosive blast simulation of a city landscape using an adaptive mesh CFD code to predict peak overpressure and impulse along the rigid geometry. Tang [Tang, 2007] conducted similar simulations using the same urban setting.

Lu [Lu and Wang, 2006] conducted a simulation to determine the response of a multi-story building to an above-ground blast using a coupled approach. Using the AUTODYN-3d code, the air around the building was modeled using an Eulerian approach and the building frame and soil were modeled using a Lagrangian approach. Baylot [Baylot and Bevins, 2007] performed a similar simulation and varied the standoff distance of the airblast using the DYNA3D code for the structural response of the building and the CTH shock physics code to compute the pressure boundary conditions to apply to the finite element model.

Clutter [Clutter and Stahl, 2004] performed blast simulations using the CEBAM hydrocode to assess facility vulnerability. The vulnerability assessments were conducted to evaluate the explosion process in numerous complex geometric configurations. The scenarios ranged from settings which included only a few structures to larger domains such as urban environments that included cooling towers and surrounding buildings, a car bomb in a dense urban setting, and an offshore platform.

Simulations for vehicles

In developing mine protection characteristics for a vehicle, the design of the occupant protection systems can be performed only in the context of the complete vehicle. However, notably few published studies have addressed the fluid-structure interactions between blast waves and a complete vehicle.

Tai et al. [Tai et al., 2007a] investigated the interactions and impact effect between air-blast waves and an armored vehicle. The geometry consisted of a simplified model of a six-wheeled armored tank, including the muzzle, turret, wheels, and hull. The decoupled inviscid CFD simulations (i.e. assuming a rigid vehicle) were used to examine the pressure variation and shock wave interaction with the vehicle. It was found that the geometry of the vehicle is a key factor in determining the intensity of impact during the propagation of the shock waves. Silver [Silver, 2006] used a commercial CFD code to predict the overpressure of a large caliber gun mounted upon a simplified, rigid tank geometry. Similarly, Kim [Kim and Han, 2006] used a commercial CFD code and a structural response code (GUNBLAST) to predict the response of and damage to an aircraft wing and equipment mounted in the aircraft that were subjected to repetitive blast waves from a gun mounted on the aircraft.

Honlinger et al. [Honlinger et al., 1996] modeled the occupant compartment of a 6x6 vehicle, including components above the vehicle floor such as the transfer boxes, axle shafts, and tank and floor liners. This simulation decoupled the loading simulation from the structural simulation. The time-dependent pressure distribution was calculated using a 2D Euler, explicit, higher-order finite difference code. This pressure distribution was then applied to the finite element model, using LS-DYNA to compute the structural response.

Lottati et al. [Lottati et al., 1996] used a coupled CFD/CSD approach to design a blast deflector to improve the survivability of a tactical vehicle subject to mine blasts at different locations under the crew cab and wheels. The pressures were calculated using the AUGUST-3D Euler CFD code. The assessment of the structural response to the blast load was computed using the DYNA CSD code. A simplified geometry model of the eight-wheeled vehicle included the cab, body, frame, wheels, transmission, and axles.

Fairlie and Bergeron [Fairlie and Bergeron, 2002] used a coupled Euler-Lagrangian approach with AUTODYN hydrocode to perform mine blast loading simulations to assess blast effects on a light armor vehicle.. The blast simulations demonstrated both above ground (air blast) and buried charges and were used to extract local velocity measurements from various parts of the vehicle. For these simulations, a complete model of the vehicle structure, suspension system, and wheels was created in order to ensure a realistic response to a mine detonation under one of the vehicle wheels. The model also included other bulky and heavy components such as the engine gearbox, differentials, leaf springs, axles, shock absorbers, wheels, and tires. .

Grujicic et al. [Grujicic et. al., 2007a] performed numerical simulations demonstrating the effects of a mine blast on a commercial truck. The simulations modeled the interactions between the detonation-products/soil ejecta resulting from the explosion of a shallow-buried mine and a Ford F800 single-unit commercial truck. The simulations were performed using the Eulerian-Lagrangian coupling options with the AUTODYN hydrocode. An especially detailed geometric model of the truck was used. The geometric components included the body, cabin, transmission, suspension, gear box, fuel tank, wheels, tires, spokes, bumpers, fenders, brakes, engine and mount, batteries, fuel tank, and other structural members. The results showed that: 1) the kinematic response of the vehicle to a landmine detonation and the amount of blast momentum transfer is sensitive to the proportion of water in the sand into which the landmine is buried – for saturated sand, the tunneling-effect gives rise to localized damage while for dry sand, the damage is spread out over a larger area – and 2) the presence of frequency components in the initial blast-loading impulse, which match the vehicle's natural frequency, plays a significant role in the kinematic response and damage of the vehicle.

Similar to the previous reference, Grujicic et al. [Grujicic et al., 2008c] also conducted simulations to determine the survivability of a 1994 Chevrolet C1500 commercial pick-up truck

subjected to the detonation of landmines buried in different soil types. These simulations were also performed using the Eulerian-Lagrangian coupling options with the AUTODYN hydrocode. Again, a very detailed model of the pick-up truck was used, including the cabin, bed, transmission, suspension, gear box, fuel tank, wheels, tires, rims, bumpers, fenders, brakes, engine and mount, batteries, radiator, fuel tank, and other structural members. The results demonstrated that the soil type and moisture content affect both the extent and spatial distribution of the damage and the kinematic response of the vehicle and that the blast load contains minimal low-frequency content and therefore does not provoke a whole-vehicle resonance response when subjected to the mine-detonation loading.

Fallet [Fallet, 2008] conducted a simulation of an explosion of a buried landmine under the front wheel of a civilian pickup truck. The simulation was performed using a coupled Eulerian/Lagrangian approach with the HyperWorks RADIOSS model. The geometry included the complete vehicle, specifically a detailed model of the cabin, tires, wheels, suspension, and underbody. The results of the simulation were used to determine where to reinforce the vehicle structure with armor plates to limit blast penetration into the vehicle. It was also used to design energy absorbers for the vehicle seats to limit the acceleration level on the passenger.

Additional references to simulations of vehicles subjected to mine blasts are available [Williams, 2002a, Williams, 2002b, Grujicic et al., 2008, Grujicic et al., 2008b]; however, they were not accessible during the course of the review.

1.2 Generic blast wave modeling

Blast wave modeling can be performed using methods of varying fidelity. Classical method use analytical self-similar solutions for a spherical blast wave originating from a point source [Taylor, 1950a, Taylor, 1950b]. This theory can be expanded to more practical scenarios by including effects such as the contributions of the source mass [Freiwald and Axford, 1975]. The ConWep [Hyde, 1991] software package can be used to provide semi-empirical blast loading functions produced by a variety of weapon configurations. These blast loading functions can be used to compute structural responses to various blast scenarios. However, these prescribed loading functions cannot predict effects due to reflections or obstructions and thus are generally applicable only at sufficiently large distances from the blast source. In order to model these effects, a more detailed Computational Fluid Dynamics (CFD) solution is required.

CFD solutions for blast wave modeling can range in detail from modeling an initial sphere of hot dense gas, to modeling the detonation and chemical decomposition that occurs within the explosive material, and possibly the after-burning that occurs when the explosive gases mix with the surrounding air. The simplest of these models treats the explosion as the spontaneous rupture of an isothermal sphere. When using an ideal gas solver, this is accomplished by defining a region of ideal gas with a density equivalent to the explosive material, and an energy equivalent to the energy released by the explosive. Such models do not perform well in the near-field region, but they can predict reasonably well the peak overpressure and impulse at a suitable distance from the explosive charge [Grujicic et al., 2007a].

To obtain a better near-field prediction, one can employ the same isothermal sphere methodology, except replace the ideal gas equation of state with one that better represents the non-idealities of the explosive gases (i.e., non-idealities of the air under high pressure may also be required to correctly capture near field physics). Under high pressures, gases depart from the ideal gas model due to the increasing influence of short-range intermolecular forces such as van der Waals forces. For explosive gases, there are many candidate equations of state that can

describe the explosive gases. Most are empirically derived to match shock front velocity data from explosive tests. The most common of these are the Jones-Wilkins-Lee (JWL) [Lee and Tarver, 1980] and the Becker-Kistiakowsky-Wilson (BKW) equations of state.

The JWL EoS gives pressure as a function of density and energy, as defined by the equation:

$$P = A\left(1-\frac{\omega\rho}{R1\rho_0}\right)\exp\left(-R1\frac{\rho_0}{\rho}\right)+B\left(1-\frac{\omega\rho}{R2\rho_0}\right)\exp\left(-R2\frac{\rho_0}{\rho}\right)+\frac{\omega E\rho}{\rho_0}, \qquad (1.1)$$

where A, B, $R1$, and $R2$ are constants associated with the material and ρ_0 is the density of the unexploded explosive solid at standard temperature. In some cases, it is desirable to have the temperature of the exploded gas (e.g., temperature is required to model the secondary burning of the explosive products upon mixing with air). This requirement poses a problem for equations of state that describe pressure as a function of density and energy. However, in such cases, a thermodynamically consistent temperature can be derived by using the Helmholtz free energy function, $\psi = e - Ts$, where the constraint that entropy, s, cannot be destroyed yields the relations [Baer and Nunziato, 1986a]

$$e = \psi(\rho,T) - T\frac{\partial\psi(\rho,T)}{\partial T} \qquad (1.2)$$

and

$$P = \rho^2\frac{\partial\psi(\rho,T)}{\partial\rho}. \qquad (1.3)$$

Using these relations, one finds that the temperature for the JWL EoS is given by [Baer and Nunziato, 1986a]

$$T = \frac{1}{C_v}\left[e + \Delta H_{\text{det}} - A\frac{\omega\rho}{R1\rho_0}\exp\left(-R1\frac{\rho_0}{\rho}\right) - B\frac{\omega\rho}{R2\rho_0}\exp\left(-R2\frac{\rho_0}{\rho}\right)\right]. \qquad (1.4)$$

Alternatively, a temperature dependent form of the JWL EoS [Lee and Tarver, 1980] can be employed whereby pressure is expressed as

$$P = A\exp\left(-R1\frac{\rho_0}{\rho}\right)+B\exp\left(-R2\frac{\rho_0}{\rho}\right)+\omega C_v T\frac{\rho}{\rho_0}. \qquad (1.5)$$

The BKW EoS provides pressure as a function of density and temperature as well as providing a mixing rule. This is a mixed parameter EoS that defines pressure using

$$P = \rho\tilde{R}T\left[1+\chi\exp(\beta\chi)\right], \qquad (1.6)$$

where $\tilde{R}$ is the mixture gas constant, β is a tuned constant, and χ is a mixture coefficient given by the mixing rule

$$\chi = \frac{\kappa \sum n_i k_i}{V(T+\theta)^{\alpha}} \tag{1.7}$$

where θ, α, κ are tuned constants, while n_i and k_i are coefficients of the gas species which are available through standard references [Mader, 1979]. This approach is advantageous because the mixture rule, although simple, still provides a temperature of the mixture. In addition, this mixture rule correctly reduces mixtures to thermally perfect as densities decrease. However, a disadvantage of the BKW EoS is that all of the species must utilize it.

Mixture rules

When performing a blast-wave simulation in an Eulerian context, it is crucial to determine the method for evaluating the thermophysical properties of the mixture of materials. For example, as the explosive gases expand into the surrounding atmosphere, the cells at the interface between the explosive gases and air will contain both air and explosive gases. Similarly, when modeling a detonation front through the explosive material, an evaluation of a mixture of EoS will be needed. The implementation of the mixture rule can affect interface dynamics as well as the numerical robustness of the solver. There are several approaches to consider for formulating the mixture EoS from the component material EoS, as outlined below.

The straightforward approach to treating a mixture of materials is to assume that each component of the mixture is immiscible and that these components are in pressure and thermal equilibrium [Luke and Cinnella, 2007]. A standard framework exists to compose individual material EoS functions into a mixture EoS using these assumptions. However, in the case of short time-scale events such as blasts, it is unlikely that sufficient time elapses so that thermal equilibration can occur. Without a separate energy equation for each species, there is little justification for a specific alternative. Nevertheless, many mixture rules that depart from thermal equilibration have been used in simulations of explosive blasts. Usually, these approaches can be justified because of their simplicity. Otherwise, the proper accounting for thermal nonequilibrium would require evolving independent energy equations for each material in addition to specifying a mixture rule. One such approach volume-averages the pressure from each material equation of state, assuming that each material occupied the entire volume and possessed the total energy [Colella and Glaz, 1985]. Other approaches [Clutter and Belk, 2002] assume a mass-weighted energy partition between species with pressure equilibrium. In the end, these different mixing rules have three potential impacts on the simulation of explosive events: 1) some of these simplified mixing rules may improve the performance of EoS queries, 2) the effective sound speed of the mixture is controlled by the mixing rule thus impacting the behavior of the interface region, and 3) as a result of thermodynamic improprieties in some of the ad-hoc mixing rules, temperature is not properly defined. Therefore, these approaches are not suitable for considering temperature-dependent models such as post-detonation burning of gases released by the detonation.

Detonation models

In the near field region, accurate modeling of an explosive event may require modeling the progression of the detonation wave through the explosive material. In some studies [Fiserova, 2006] using numerical models, peak over-pressure and impulse were found to be sensitive to the

point of initiation (and by implication resolving the detonation wave propagation). Generally, the importance of modeling these effects depends upon the objective and distance from the target.

Frequently, modeling the progress of the detonation front is more important for design of explosives than for damage evaluation. If the detonation phenomena are important, however, then there are several levels of detail that can be employed to model the propagation of the detonation front. Perhaps the simplest of these is to prescribe a known detonation velocity and force decomposition of the explosive material into gas products based on the distance to the initiation point. Generally these models include some sort of smoothing parameter whereby the detonation front is distributed over several cells to improve numerical robustness. Models such as these are implemented in standard commercial codes such as LS-DYNA and AUTODYN.

More detailed models are also available whereby the decomposition reactions are employed [Menikoff, 2006, Saurel and Massoni, 1998, Tarver et al., 1997]. These models require a much finer mesh resolution than the prescribed detonation front approach described earlier, and generally they are much more computationally expensive. For the applications of interest to this research—modeling the effects of a relatively generic blast source—these schemes offer much more fidelity than is required, thus no further discussion of detailed detonation front modeling will be included.

1.3 Modeling blast-soil interactions

Soil plays an important role in characterizing landmine or IED explosive loads. The soil can both dissipate as well as focus explosive energy. In addition, the ejected soil material can comprise a significant fraction of the impulse loading on the vehicle. Broadly speaking, soil can be classified into two categories: cohesionless (sandy) soils and cohesive (clay-based) soils. Each type of soil brings its own modeling requirements. There have been significant investigations into modeling blast-soil interactions. Most of these models have employed general purpose simulation codes such as LS-DYNA or AUTODYN with soil modeled as a solid material with specific equation of state and strength models [Fiserova, 2006, Grujicic et al., 2007b, Grujicic et al., 2008d, Wu et al., 2004, Gupta, 2001, Hlady, 2004, Martin and Link, 2003, Fairlie and Bergeron, 2002, Wang et al., 2004]. In all of these models, the soil material was treated as a plastic solid material and the failure model was based on a simple limit on the tensile strength. The three components of most of these models included an equation of state, a strength model, and a failure model. Fiserova gives a detailed account of many of the modeling approaches [Fiserova, 2006].

In most of the soil models, a three phase mixture of solids, water, and air was used to obtain the equation of state [Fiserova, 2006, Wang et al., 2004, Grujicic et al., 2006]. Typically, these equations of state were implemented by prescribing a look-up table to define a density vs. pressure relationship as well as a sound speed vs. density relationship. In most of these models, values from lower pressures were extrapolated to high pressure regimes where no experimental data was available. For strength models, sophisticated models were developed based on mechanistic analogies of springs and dampers to describe the soil micro-structure response [Wang et al., 2004].

There are several common themes in all of the above models. First, they all make use of a three phase model to derive an equation of state; however, none of them represent the soil as having independent velocities for the different phases in a multi-phase model. Thus, the explosive gases released by detonation do not pass through a cloud of soil particulates, but instead escape (along with some chunks of soil) as the soil is torn open by the blast. In addition, depending on how the damage progresses through the soil, some of the soil may erode through

the use of free nodes. These free nodes represent the material removed through failure, and although they are removed from the simulation, they can then continue on their trajectory and impact nearby surfaces. However, since these free nodes do not occupy volume or have drag or have a pressure coupling to the fluid flow, this numerical approach is not particularly physical, and certainly does not respect the full complexity of a more complete multi-phase model. Because the models reviewed did not consider these effects, we considered additional literature regarding models used in similar circumstances where dense multi-phase flows experienced highly energetic events such as shocks and explosions. An overview of this review is provided in the following section.

Modeling energetic dense multi-phase flows

Soil presents a challenge for accurate modeling of the explosive interactions because it is a multi-phase mixture composed of air, water, and solids. In an event such as an explosion, a portion of the soil, in particular the overburden, becomes a dense, highly energetic, multi-phase cloud of material that ejects out of the developing crater. We are interested in determining what physical phenomena may be significant to modeling such a dense multi-phase cloud of soil material. In this section we outline models that have successfully been employed in multi-phase shock interaction problems. While some of the soil models did build upon a multi-phase model to construct the equation of state, they did not consider non-equilibrium effects such as independent velocities of the solid and gas phases, or the effects of energy transfer through particle-particle collisions. However, there have been numerous studies on the solid particles dispersion under shock or explosion. We outline a sample of these models in order to better understand the physics of a dense cloud of soil particulates that forms when a buried explosive is detonated.

In the explosive dispersal process of a packed bed of solid particles saturated with explosive, the flow topology ranges from a granular flow during the propagation of the detonation within the charge to a dilute gas-solid flow at distances far from the source. In the dilute flow, where distance between particles is great enough, no pressure terms and shear stress would be required to describe the particulate phase. In the early stage of the explosion, the soil particles are densely packed and particle-particle collisions have to be taken into account.

In the literature, we have identified several proposed two-phase models appropriate for describing a dense gas-solid, or a granular flow, in which particle-particle collisions are important. Baer and Nunziato [Baer and Nunziato, 1986b] (BN model) presented a two-phase mixture theory to describe the deflagration-to-detonation (DDT) in reactive granular material. This theory, which was based on a continuum assumption and included the effects of compressibility for all of the phases and compaction for the granular material, described a granular explosive in terms of a gas phase that filled the interstitial pores between chemically reacting solid grains. The velocity, temperature, and pressure of the two phases were allowed to be unequal. With the introduction of Helmholtz free energy and by requiring the model to satisfy the entropy inequality (second law of thermodynamics), specific constitutive equations representing important aspects for granular materials were developed. A dissipation inequality for the mixture was employed to formulate coupling source terms, requiring that at each point the mixture entropy not decrease with time. In the BN model, the pressure in the solid grains equaled the pressure in the gas phase plus the pressure due to contact force between the grains (i.e., configuration pressure) which depends on the rate of change of Helmholtz free energy with solid volume fraction. Later, Powers et al. [Powers et al., 1990] noted some inconsistency in the treatment of the solid free energy's volume fraction dependence and developed a more general

model that incorporated most features of the BN model plus a set of specific constitutive relations. Bdzil et al. [Bdzil et al., 1999] examined the BN mixture model, with particular attention paid to the manner in which its constitutive functions were formulated. Deficiencies and inconsistencies in the derivation in the BN model are cited, and improvements are suggested. It is noted that the entropy inequality constraints do not uniquely determine the phase interaction terms. The resulting flexibility is exploited to suggest improved forms for the phase interaction. The BN model treats each phase as compressible and in complete thermodynamic nonequilibrium, Therefore, it is suited for description of the various thermal and mechanical processes leading to detonation.

In contrast to the BN model, many two-phase fluid models assume pressure equilibrium. The volume fraction of the solid phase is determined by an algebraic equation rather than a particle differential equation. In a conventional two-fluid model for a dense phase flow, additional forces due to the particle-particle interaction are added to the momentum equation for particulate phase. These forces include the pressure and shear in the solid phase. Several proposed formulas have modeled the solid shear stress and pressure terms [Harris and Amsden, 1994, Gidaspow, 1994]. Among them, Gidaspow's model [Gidaspow, 1994], based on the application of kinetic theory, has drawn significant attention in the community. Because of similarities between particle-particle interactions and molecular interactions in a gas, the concepts from kinetic theory were applied to develop the governing equations for dense flows: particle-particle collisions are responsible for momentum and energy transfer in a dense flow in the same way that molecular interactions are responsible for pressure wave propagation and viscosity in a single phase fluid. Thus, the fluctuating kinetic energy associated with particle-particle collisions is defined as granular temperature and one extra governing equation for granular temperature based on the Boltzmann equation is added to the equations for the particulate phase. The granular temperature θ is defined as one-third mean square fluctuational velocity of particle motion as follows:

$$\theta = \frac{1}{3}\langle C^2 \rangle, \tag{1.8}$$

where C is the fluctuational velocity of the particle motion. Granular temperature can be produced by a shearing action in granular flow and by hydrodynamic forces. Dissipation can occur through inelastic particle-particle and particle-wall collisions and dissipation in the fluid. Granular temperature can also be diffused in the same manner as heat. The interaction of the fluctuating and mean motion of the particles gives rise to an effective shear viscosity for the particulate phase, and particle-particle collisions also generate the pressure of particle phase. Both shear viscosity and pressure of particulate phase can be expressed as the function of granular temperature, which provides complete closure models for the equation system. Gidaspow's approach has the advantage of being able to clarify many physical concepts raised by particle-particle collisions using granular temperature.

There are some heuristic constitutive models for solid flow. Zhang et al. [Zhang et al., 2001] estimated the pressure and sound speed of the particle system using a heuristic interpolation method, which is realized by applying a weighting function to the solid volume fraction between the solid limit and the dilute flow limit.

Models for shocked multi-phase flows

The literature extensively documents models that account for the interaction between solid particles and an incident shock wave. For example, Fan et al. [Fan et al., 2007] investigated both experimentally and numerically the interaction of a planar shock wave with a loose, dusty bulk layer,. Experiments were conducted in a shock tube. The incident shock wave velocity and particle diameters were measured with the use of pressure transducers and a Malvern particle sizer, respectively. The flow fields of both the gas and dense particle phase induced by shock waves were visualized by means of shadowgraphs and pulsed X-ray radiography with particle tracers added. The particles, which were deposited homogeneously inside the test chamber, were ultra-fine starch particles with a mean diameter of 15μm. In their numerical work, the Gidaspow model [Gidaspow, 1994] was employed to provide closure for the particle-particle interactions. Both experimental measurements and numerical results showed that interaction of the shock with the granular particle layer produced curvature in the incident shock in the downstream direction. This interaction is caused by the large acoustic impedance of the granular material compared to that of the gas. In addition, under the action of incident shock wave, the transmitted shock wave, which is induced inside the granular material, makes an oblique angle. Particles are most concentrated at the oblique interface where the gas and particles meet behind the shock. Numerical results revealed that the fluctuating motion of the particles, which dominates the collision pressure, the collision momentum transfer, and the granular conductivity, happened mainly in the region behind the transmitted shock in the granular material.

Experimental and numerical studies of shock impingement on a particle bed were conducted in a vertical shock tube [Rogue et al., 1998]. The shock-induced motion of particle beds of various thicknesses was investigated. Analysis of shock formation showed that the particle bed acted as an obstacle to the gas flow, leading to a reflected shock that propagated upstream, a complex refracted shock that passed through the bed, and a weak transmitted shock propagating downstream. While the dilution of the particle bed proceeded (the front layer of particles moved faster than the lower layer of particles, leading to the dilution of particle bed), a rarefaction propagated toward the upstream and a compression toward the downstream. While the rarefaction waves overtook the reflected shock and weakened it, the compression waves merged with the transmitted waves and strengthened it. Due to the stronger blockage effect of a double layer (compared to a single layer), the strength of the reflected shock was stronger for the double layer. In contrast, the strength of transmitted shock through the particle bed was weaker for a double layer. The effect of inter-particle collisions has been illustrated with the two-layer bed, which became more dilute than a single particle layer (the front layer of particles moved faster than the lower layer of particles, leading to the dilution of particle bed). The collisions between particles in the two-layer bed permitted a faster dilution of the particle cloud and hence presented less of an obstacle to the gas flow. Therefore, the gas flows faster through a two-layer particle bed than a single layer one, which implies that a single-layer bed presented more of an obstacle to the gas flow. The dynamics of a thicker bed (thicker than two layers) were also characterized by faster dilution; however, in this case, the rise in the number of particle layers did not allow a rapid gas flow through the cloud particles. The high particle density, in spite of an important dilution of the cloud, still exerted a significant resistance to the gas flow. In their numerical simulations, Saurel et al. [Saurel et al., 1992] investigated one-dimensional flows. The drag coefficient used comes from an experimental investigation for a single particle. The collisions between particles were taken into account by the use of a particle interaction tensor, which is a function of the particle volume fraction. In their numerical model, artificial diffusion was

introduced to handle solution discontinuities. The numerical results showed that the drag force is the main factor contributing to the dynamics of the dense particle cloud. Inter-phase heat transfer scales and particle-particle collisions at the early stage of cloud motion had only a minor effect.

Large solid volume fraction effects in multi-phase flows

For very dense multi-phase flows, the effects of large volume fractions of the solid and liquid phases must be taken into account. In addition to the particle-particle collision effects outlined in the previous section, the existence of the large volume fraction modifies the effective speed of sound of the respective phases. The speed of sound drops, sometimes significantly, at large volume fractions. The effects of the change of sound speed can be accommodated by utilizing an integrated equation of state that incorporates the compressibility of each phase. Alternatively heuristic models can be used. For example, Zhang et al. employed an asymptotic rule [Zhang et al., 2001] and developed a heuristic model to describe the dependency of particulate phase sound speed on the solid volume fraction. Another challenge is characterizing the drag coupling between the phases when the volume fraction is large. The drag of particles in dense two-phase flows differs from the drag in dilute flows: The influence of neighboring particles on the gas flow renders traditional drag correlations invalid. Also, analytical models are difficult to derive because an adequate model must account for the surface of every nearby particle. Experimental studies are prevented by the difficulties of measuring the force and the local flow field for an individual particle in a cloud. Most of the data for particle drag have been inferred from sedimentation and fluidization bed studies in which drag force on particles balances with the pressure drop in a packed bed. Based on Ergun's pressure drop equation [Ergun, 1952], Gidaspow [Gidaspow, 1994] provided a particle drag coefficient formulation that characterized drag in a two-phase flow with large solid volume fraction (solid volume fraction larger than 80 percent).

Modeling impulse in a multi-phase explosion

The damage to a nearby structure from a homogeneous explosive is primarily due to the momentum transferred from the gas flow. In the near field, the high momentum flux of the gas-solid flow from a heterogeneous explosive can generate particularly large forces on adjacent bodies. In multi-phase explosive events, the momentum of the blast wave is augmented by the solid fragment impact. Frost et al. [Frost et al., 2007] carried out an experiment and numerical work to characterize the particle momentum flux generated by the detonation of a heterogeneous explosive consisting of a packed bed of inert particles to determine the relative contribution of the particles and the gas blast wave to the impulse exerted on the nearby structure. In their experimental work, the momentum flux was measured by the bending work done on a cantilever gage or the momentum imparted to a free piston. In their numerical model, nonequilibrium processes between each phase in the explosive were considered and BN [Baer and Nunziato, 1986b] model to represent the constitutive laws and the evolution of solid volume fraction was adopted. In the simulations, only drag force and pressure gradient of solid phase were included in the particulate phase momentum equation. Other forces such as the pressure gradient within the gas, the Basset force (this term addresses the temporal delay in boundary layer development as the relative velocity changes with time) and added mass force (this term represents the force to accelerate the gas near the particle surface) are neglected. When particles are added to a homogeneous liquid explosive, the peak blast wave overpressure and the positive pressure impulse (only from gas) are decreased in comparison with a homogeneous charge. This is caused

by the fact that a portion of energy and momentum released from the gas goes into heating and accelerating the particles. The total impulse applied to a nearby structure by a particle-laden flow is the sum of the impulse applied by the gas dynamics and that from the particle collision with the structure. Comparing the impulse from the heterogeneous charge (a packed bed of steel beads saturated with sensitized nitromethane) with that of homogeneous charge with the same amount of explosive, the heterogeneous charge produce larger impulse on the nearby structure by a factor of two in their experimental setup. Since the addition of particles reduces the gas-phase impulse by a factor of two, the integrated momentum flux from the particles in the near field therefore must increase by a factor of about four over the gas momentum. They concluded that the total impulse applied to a nearby body was dominated by the impulse due to particle impacts for the heterogeneous charge.

Simulation of blast interactions with debris

Within the study of clouds of small particles (dusty gas flows), it is difficult to ascertain the interaction effects between an incident shock and a particle. Hence, in experimental studies with a single or small number of small particles, it is difficult to arrive at the dependency between the drag coefficient and Reynold's number. Due to refraction, reflection, and diffraction, the geometry and amplitude of the wave fronts are altered due to the interaction of the shock wave with particles. These interaction effects become significant when large debris/fragments are present and thus numerous experimental investigations have been performed, particularly with spherical geometries. Simulations treating these large debris/fragments as rigid bodies and tracking their interactions with forces due to blast waves demonstrated that six degree of freedom trajectory computations can be employed in the validation of phenomenological debris/fragment models. To follow is a brief review of methods for simulating and tracking moving objects in fluid fields and a list of exemplary experimental studies by which the current models may be compared.

Although other approaches have been proposed, the two most appropriate techniques for simulating and tracking moving objects in fluid fields when large motion is present consist of embedded domain and over-set mesh methodologies. To this end, the volume of literature using these approaches for moving body simulations in aerodynamic and hydrodynamic applications is vast. Representative examples of embedded approaches may be found in [Löhner et al., 1999, Murman et al., 2003, and Pember et al., 1995], and for the over-set mesh method in [Buning et al., 2004, Chen et al., 2008, and Lijewski and Suhs, 1994].

The over-set mesh method overlaps body-fitted grids for all objects within the field. The governing equations are then solved on each grid, and inter-grid communication is accomplished via interpolation at boundaries of their domains. Similar to embedded approaches discussed below, cells that fall within solid bodies may be deactivated. Additionally, since the inter-grid communication is typically accomplished at outer boundaries, large portions of the grids that are overlapped may be deactivated as well. This approach requires substantially less code complexity, and may be implemented in parallel software in a scalable manner. Search algorithms are required to search adjacent grids in order to reestablish the interpolation stencils for moving bodies as the simulation proceeds. The body-fitted grids allow a precise description of the geometry and no issues arise with regards to boundary resolution for viscous simulations. Special care must be taken in the case of contact between objects, with regards to boundary condition enforcement as well as potential overlapping between regions of the mesh with disparate grid resolutions. In the latter case, mesh refinement may be used to address this

disparity. Another critical issue arises with topological changes of a given body, such as those associated with general facture of a structure. The original structure would be discretized with a given mesh. A priori details of the fracture are not readily known. This concern remains problematic due to the fact that each of the individual fragments/debris would require new grids to be generated. Additionally, each fragment would essentially be in contact or near contact with many others.

The embedded domain method, or Cartesian grid method, inserts the objects onto a mesh that discretizes the entire domain. A search algorithm then identifies the cells/edges that intersect or fall within the body. The cells that fall within the body are deactivated. For those that intersect the body, boundary coefficients are formed to ensure flux balance. This embedded boundary treatment is an approximation and introduces errors into the solution. Adaptive mesh refinement may be used to reduce these errors by better representing the geometric surface. Additionally, viscous simulations, which require highly stretched meshes near the surface for boundary layer resolution, are problematic. This issue stems from the fact that, since the mesh is not body-fitted, regions of the mesh would essentially be refined in nearly an isotropic manner and, hence, may result in prohibitively large grid sizes. Furthermore, as simulations for moving body applications proceed, the geometric description would need to be retained, while the search algorithm used to re-identify the cells that intersect and fall within the body, extrapolation of the solution for cells that re-enter the domain (i.e., deactivated points become part of the computational domain), and adaptive refinement all performed again. However, topological changes and general fracture of a structure does not pose any difficulties within the embedded domain method.

There are numerous experimental investigations concerned with studying the interaction between large particles and shock waves. A short list of potential studies for comparison includes [Britan et al., 1995, Ingra and Takayama, 1993, and Susuki et al., 2005]. These studies consisted of utilizing shock tubes to accelerate spherical particles of various diameters and densities. Within these experimental investigations, the trajectories and velocities of the particles were measured. From these, calculations of the drag coefficient were made and typically presented as a function of the relative Reynold's number. Additionally, in Susuki et al. 2005, due to large vertical components of the trajectories, the rotational speed of the particles was also measured to ascertain the influence of the Magnus effect. Although large rotational speeds were measured, it was concluded that the Magnus force had little influence and did not significantly contribute to the lift of the particles. Studies performed in smooth and rough wall horizontal shock tubes indicated that the floor conditions had the strongest influence.

1.4 Blast generated fluid-structure interaction (FSI)

Generally, there are two approaches by which the structure is encompassed within the surrounding fluid media. One approach represents a non-overlapping technique whereby the CFD and CSD domains share a common wetted surface (outer mold line). In this approach the surface discretizations and corresponding volume meshes must be adapted to reflect the structural deformations. MSU currently has well-validated software to accommodate this methodology [Blades and Newman, III, 2007a,b] for FSI of aerospace vehicles. It is recognized that this approach is computationally the most efficient, but it has potential bottle necks for large structural deformations that could cause a failure in the volume adaptation process as well as an inability to accommodate geometry fragmentation. The other approach is an overlapping (embedded) technique whereby the CSD mesh is overlapped onto the CFD domain. Although more algorithmically complex and computationally expensive, this approach suffers no such

shortcomings with regard to geometry fragmentation. However, the interdisciplinary transfer of data in the cases of surface cracking or fragmentation may require solution adaptive meshing techniques in order to ensure adequate resolution. Technology for this approach is currently under development within the Loci/CHEM framework/code.

Newman [Newman, III, 1997] provided an early, comprehensive review of non-overlapping approaches for FSI; his effort will not be duplicated here. More recently, Jaiman et al. [Jaiman, et al., 2006] further classified these non-overlapping approaches into point-to-point, point-to-element, and common-refinement schemes. Within this context, the current MSU technology falls into the point-to-point category. Jaiman then additionally subdivided the point-to-element schemes into node-projection [Farhat, et al., 1998] and quadrature-projection [Cebral and Löhner, 1997] methods. Jaiman compared the two traditional point-to-element methods with their developed common-refinement scheme for a variety of FSI applications. Both point-to-element approaches illustrated an oscillatory solution for interface displacements and shear stress for blast wave-solid interaction. Furthermore, errors in excess of 20% were present when compared to results from matching meshes. Within the study of [Jaiman, et al., 2006], point-to-point schemes were not considered and, hence, will require investigation for their applicability and accuracy to blast wave-structural interactions.

Although an exhaustive list will not be given here, there are many researchers currently using loosely coupled CFD/CSD methodologies to simulate blast-structure interaction problems. Probably the most notable contributions have been given by Baum, Löhner, and their co-workers [Baum, et al., 2003, Löhner, et al., 2004b,c, Baum, et al., 2004a, Löhner, 2004a, Baum, et al., 2006, Rice, et al., 2006, Baum and Löhner, 2006, Soto, et al., 2008, Baum, et al., 2008]. In these references, the Euler/Reynold's Averaged Navier-Stokes solver FEFLO98 [Löhner and Baum, 1992] and MARS3D [Pelessone and Charman, 1998] (a derivative of DYNA3D [Whirley and Hallquist, 1991]) were utilized for the CFD and CSD analyses, respectively. Early work by these researchers utilized the non-overlapping quadrature-projection scheme of [Cebral and Löhner, 1997], but later adopted the embedded approach [Baum, et al., 2004b]. A variety of blast wave-structure interactions were analyzed within this body of work. These simulations ranged from blast loading on plates to building structures. Furthermore, the fidelity of the simulations also ranged from relatively coarse grid Euler simulations to detailed analyses of blast wave evolution. Of particular interest to the current work are Baum, et al., 2006 and Baum, et al., 2008, which dealt with the blast-wave structural interaction on plates. For example, in Baum, et al., 2006 the numerical solutions of bare charges within a cylindrical tunnel were directly compared with experimental results. Pressure-time histories were compared for blast wave impingement on rigid end walls and deformations compared for deformable end plates. Additional examples of the loosely coupled CFD/CSD methodology, as applied to plates and shells, may be found in [Liang and Hsu, 2001] and [Chan, 2004]. In [Liang and Hsu, 2001] unsteady cylindrical blast-wave interaction with a flat plate was simulated, whereas in [Chan, 2004] the FSI of a flexible tent structure was modeled.

As directed by the COR, the FSI coupling shall utilize the LS-DYNA code [LS-DYNA User Manual, 2007] for the CSD analyses in this study. LS-DYNA is a commercial code, and currently no API exists for coupling with general purpose CFD codes. Hence, coupling must be accomplished via the development of an I/O file management system. Similar-type management systems have been developed in the past for this purpose. For example, NASA's FIDO framework [Weston, et al., 1994], as well as a system developed at Boeing [Borland, 1990], was used to couple government/industrial CFD codes with commercial CSD software such as

NASTRAN. More recently, CFDRC developed the commercial package MDICE [Sheta, et al., 1999] for managing data produced from multidisciplinary analyses involving various single-discipline software packages. Within the scope of this task, although representing an added computational expense, this approach is feasible for the demonstrations to assess the FSI capabilities to be delivered. Additionally, for one-way coupling, this procedure should be very useful.

The developed coupled air-blast-wave-structure interaction analysis capability will be evaluated with simplified components and numerical results compared with experimental data. These simulations shall include analyzing the shock-structure interaction of bare explosives of different charge weights at various stand-off distances as it impinges on plates. The utilization of plates for this purpose is three fold. First, it provides a reduction in geometric complexity. This reduction facilitates the use of the non-overlapping approach to FSI (in the absence of fragmentation), as well as lowering the computational requirements associated with data management between the single-discipline software components. Second, vast amounts of experimental data (briefly reviewed below) have been produced for the purpose of preliminary validation of blast-wave FSI. Third, plates are one of the most basic elements in structures and thus are representative of the FSI that will be simulated in future blast wave-vehicle interaction analyses.

Numerous experimental results are present in the literature for metallic, composite, and cellular solid plates. The current review is limited to experimental data obtained for metallic plates only. Within this body of literature, recorded data takes the form of measured pressures on both the plate and the support structures, surface accelerations (particularly when used to validate transient dynamic analyses), and structural deflections during and after the blast event. Jacinto et al., [Jacinto, et al., 2001] presented an experimental and computational study of non-stiffened metallic (steel) plates subjected to air blast loadings. Within this data set, four different tests with various amounts of explosive were carried out on two plates. One plate was clamped at the base while the other was clamped at the four edges. Experimental pressure-time and acceleration-time histories were recorded. Trzcinski and Cudzo [Trzcinski and Cudzo, 2004] experimentally studied edge-clamped rectangular steel and steel-composite plates subjected to air blast waves generated by cylindrical TNT charges of various masses. Available data for this series of experiments is comprised of resultant force-time, displacement-time at numerous plate locations, and final displacment distributions along the plate center line. Bonorchis and Nurick [Bonorchis and Nurick, 2009] ran a series of blast loading experiments on rectangular plates to ascertain the influence on the experimental set-up and demonstrate its importance on subsequent numerical simulations. Additionally, Langdon and Suhleyer [Langdon and Suhleyer, 2005] conducted experimental investigations aimed at studying the influence of connection details whereby large plastic deformations were produced in the panels without rupture. Similar experimental and computational investigations were presented in [Louca and Pan, 1998] and [Pan and Louca, 1999]. In these articles, stiffened and unstiffened plates were studied, and the data presented included displacement-time, acceleration-time, and strain-time histories. Neuberger et al., [Neuberger, et al., 2009] conducted a series of experiments in which the peak transient dynamic and the final residual deflection were measured in order to study the elastic springback of metallic plates. Moreover, Galiev [Galiev, 1996] presented counter-intuitive behavior of plates. Experiments were conducted that demonstrated the appearance of final deflections that were contrary to the direction of the impulsive loading. An explanation of this behavior was developed using theoretical techniques and aerodynamic/structural dynamic models.

Section 2: Simulation of blast interactions with realistic rigid geometries

2.1 Geometric model definition

The objective of this effor is to perform blast simulations on a complex, realistic vehicle using the Loci/CHEM code where the vehicle is assumed to be rigid. To perform said blast simulations required a sufficiently detailed geometric definition of the vehicle, including underbody components, tires, wheels, handles, and mirrors, that also adequately represented a military High Mobility Multi-purpose Wheeled Vehicle (HMMWV or Humvee). Mississippi State University (MSU) does not possess a geometric definition of a HMMWV type vehicle, so multiple web sites were searched to find potential candidate models. Neither computational fluid dynamics (CFD) models or finite element models (FEM) suitable for analysis were found. The initial model was obtained from [3dcadbrowser.com_a]. However, this model was deemed to have insufficient underbody detail. A second HMMWV model with much more geometric detail was obtained from [the3dstudio.com]. This model, however, was not approved by TARDEC.

It was then decided that a commercial sport utility vehicle (SUV) would be used for the blast simulation. A Nissan XTrail 4x4 SUV geometry model was obtained from [3dcadbrowser.com_b], which TARDEC approved for use on December 17, 2008. The SUV geometric model definition is discrete (i.e. composed of polygons and vertices), rather than a mathematical model like a NURBS definition. The discrete SUV geometric model consists of 204,062 triangles and 108,372 vertices (Figure 2.1). The underbody definition is not complete. There are no surfaces for the wheel wells or the section underneath the engine compartment. In addition, the suspension and exhaust components are floating in space, dettached from the rest of the vehicle.

2.2 Geometric model creation

The original approach to generate the volume mesh used the discrete model as the geometry definition to build the CFD surface mesh. SolidMesh, MSU's in-house-developed CAD and unstructured mesh generation software, has the capability to use a discrete model as the underlying geometric definition. The discrete geometry definition can then be re-meshed with an appropriate resolution suitable for a CFD mesh. In order for the discrete geometry capability to work correctly, the discrete model must be topologically valid or watertight. That is, all of the components must connect to one another. However, the chosen discrete SUV model is not topologically valid and thus is not suitable for use as a discrete geometry definition. As illustrated in Figure 2.2, the triangles representing the window trim do not match those representing the window glass or door panel, leaving the window trim floating in space. In fact, none of the models obtained from either the 3DCADBrowser or 3DStudio web sites were topologically valid.This situation appears to be typical for models of this type available on the web. Their purpose is for visualization, which does not require models that are topologically valid, rather than for analysis..

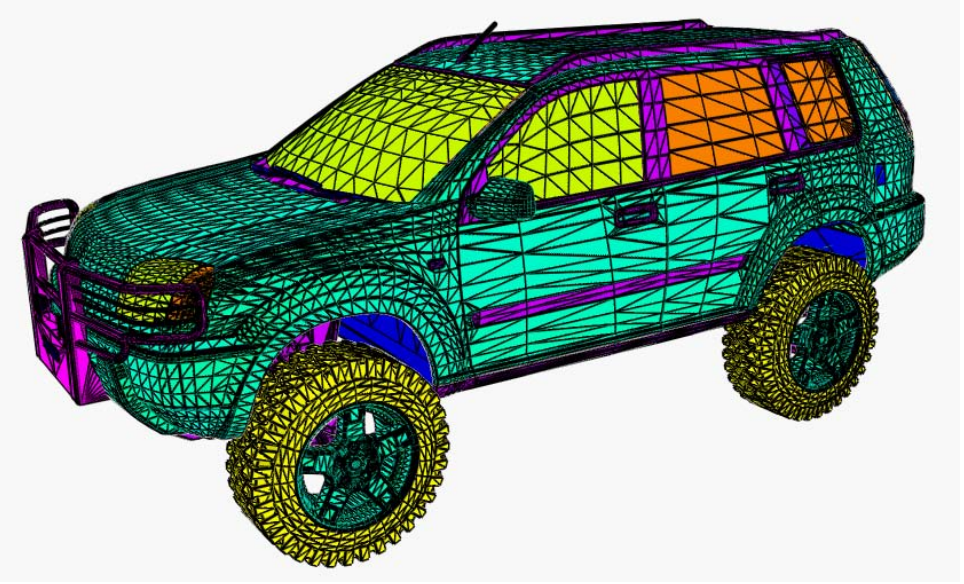

(a) Top side view

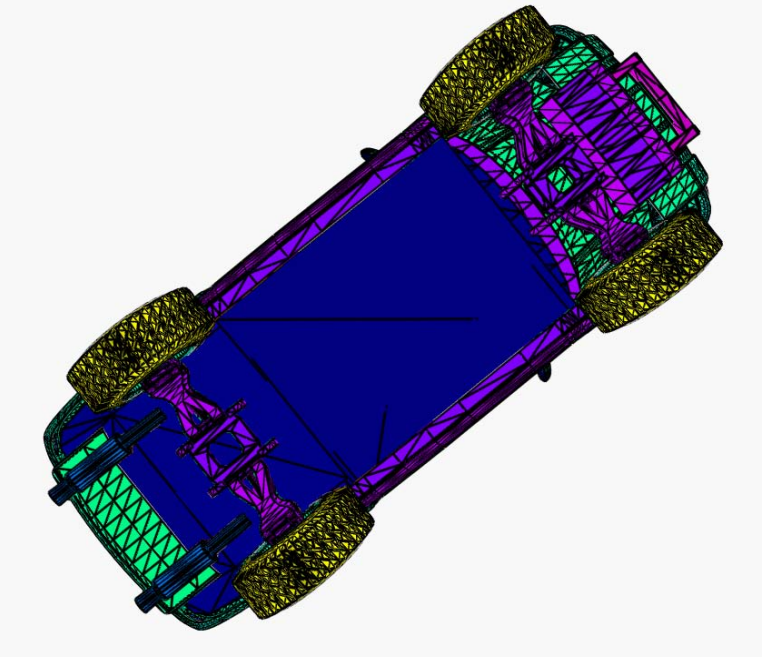

(b) Underside view

Figure 2.1: Discrete geometry definition of the Nissan XTrail sport utility vehicle.

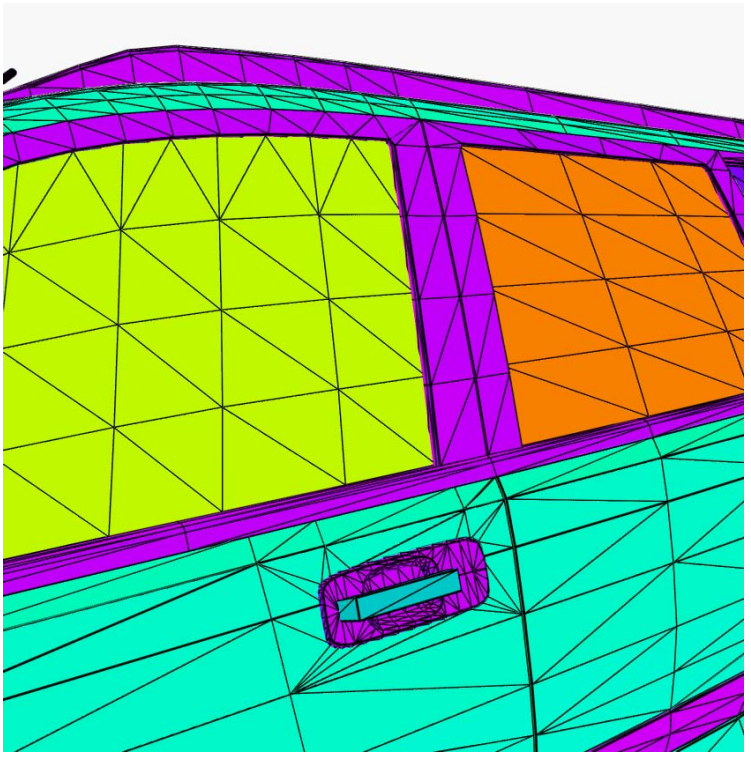

Figure 2.2: Topology problems with the discrete model definition.

The grid repair toolkit within SolidMesh was unable to repair all of the problems with the model, requiring significant manual labor to rectify the indentified issues. Therefore, the discrete SUV model was treated as a cloud of points. Although labor and time-intensive as well, geometric curves and surfaces were then manually created from the cloud of points using curve and surface generation CAD tools within SolidMesh. NURBS curves were generated using splines, and NURBS surfaces were generated from the curves using multiple surface generation techniques, including transfinite interpolation, lofting, and ruled surfaces. A half-plane geometric model of the Nissan XTrail 4x4 sport utility vehicle (SUV) was constructed using this approach. Every effort was made to retain as much geometric detail as possible. A comparison of the points from the original discrete model and the manually generated NURBS surfaces is shown in Figure 2.3. The white points shown in these images represent the vertices from the discrete model. As illustrated, the geometric CAD surfaces pass through the points of the discrete representation and thus represent the surface accurately.

The completed model is shown in Figure 2.4(a) and details of the front and rear underbody components are shown in Figures 2.4(b) and 2.4(c). Detailed views of the wheel and suspension are shown in Figures 2.5 and 2.6, respectively. The underbody definition for the original discrete model was not complete. There was no surface definition for the wheel wells and the section underneath the engine compartment. In lieu of these missing surfaces, reasonable approximations were made for these components. In order to create a topologically-valid, watertight model, a ground plane and hemispherical outer boundary were added to the domain. The diameter of the outer boundary surface was 40 meters, which is approximately 10 body lengths.

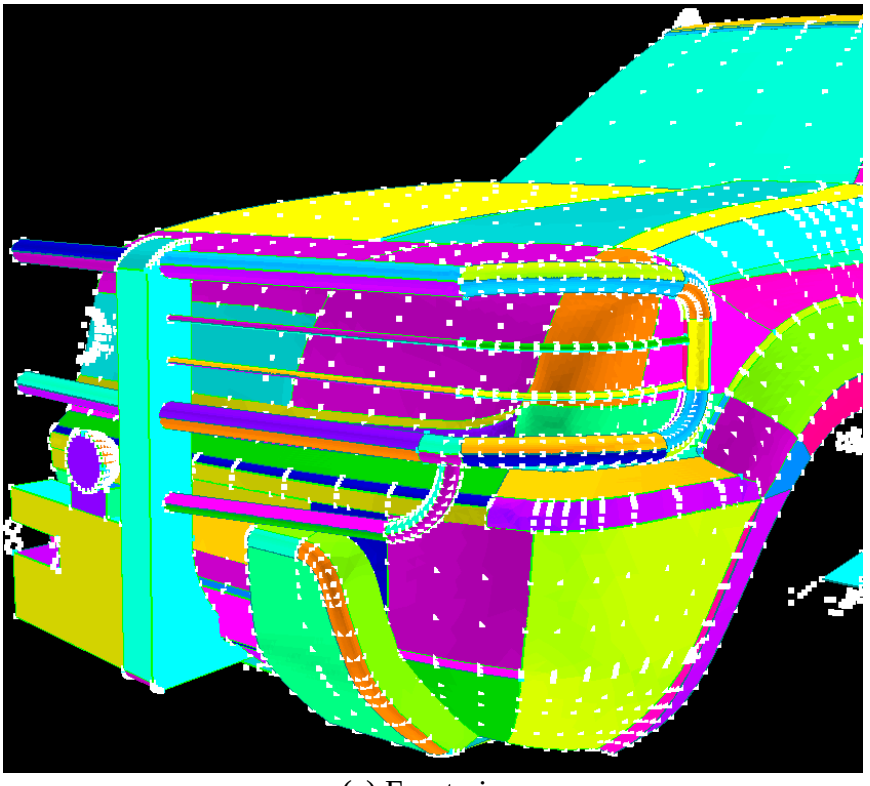

(a) Front view

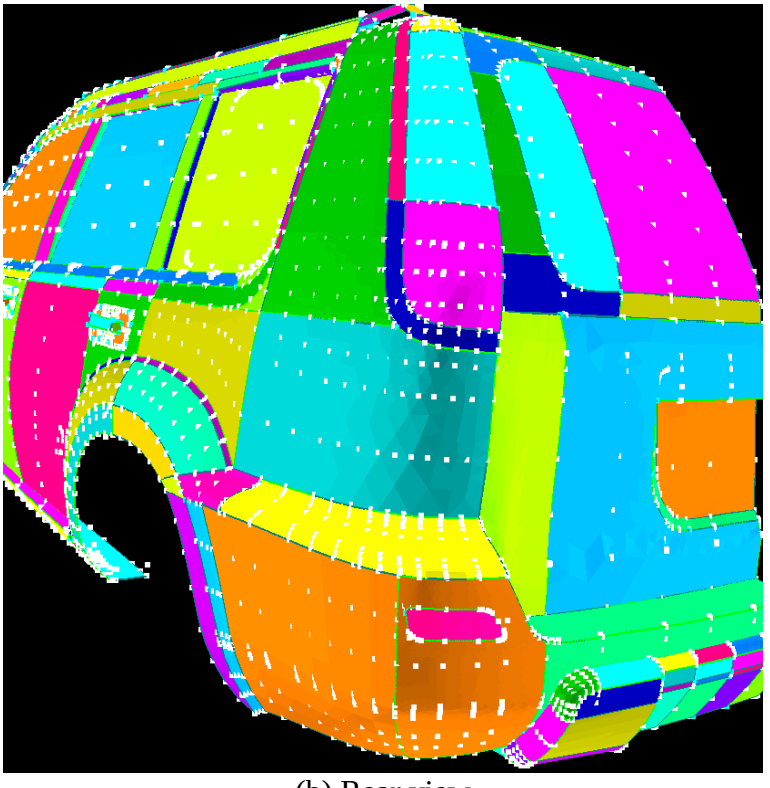

(b) Rear view

Figure 2.3: Comparison of the CAD surfaces with the original discrete model definition.

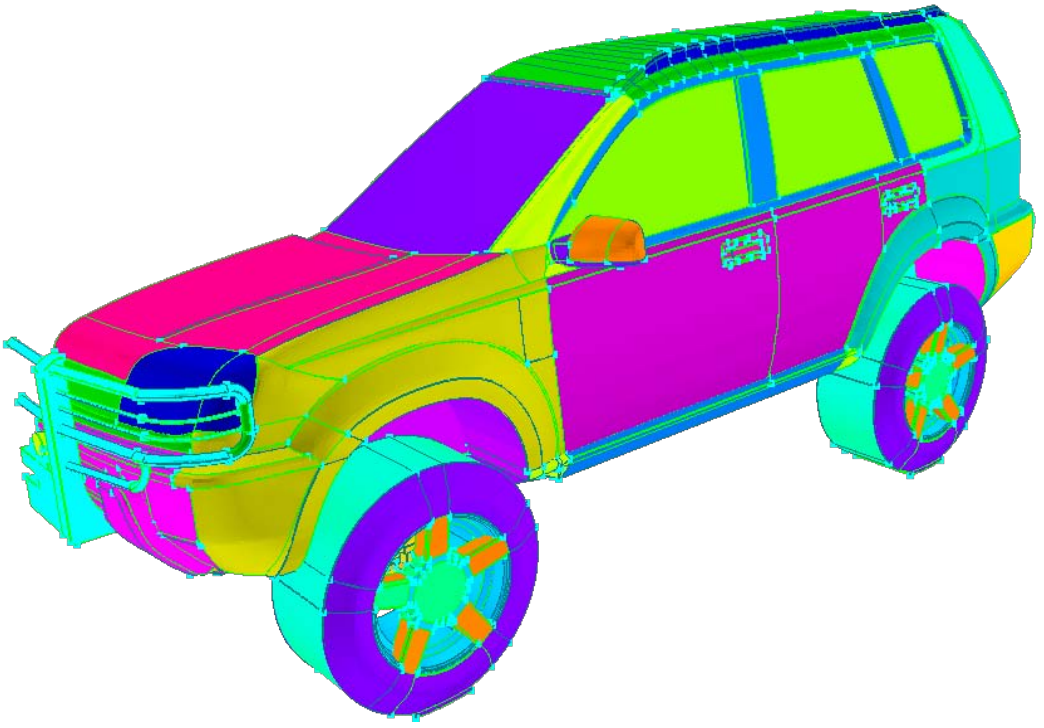

(a) Entire vehicle

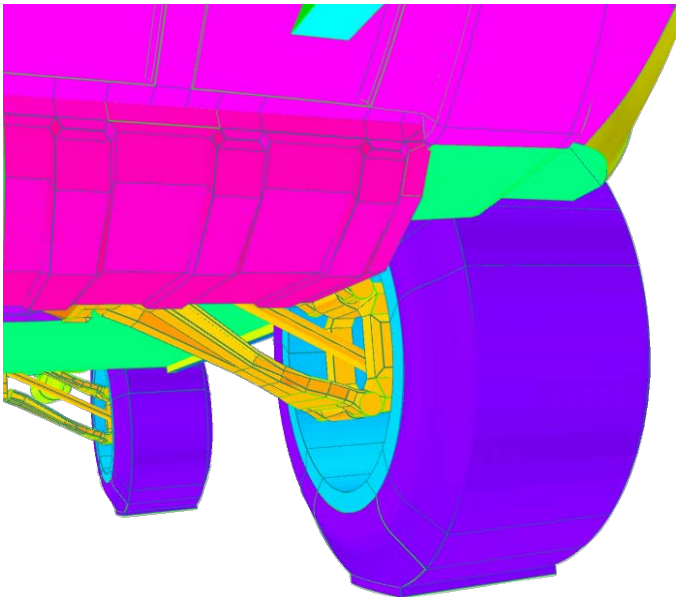

(b) Front underbody components

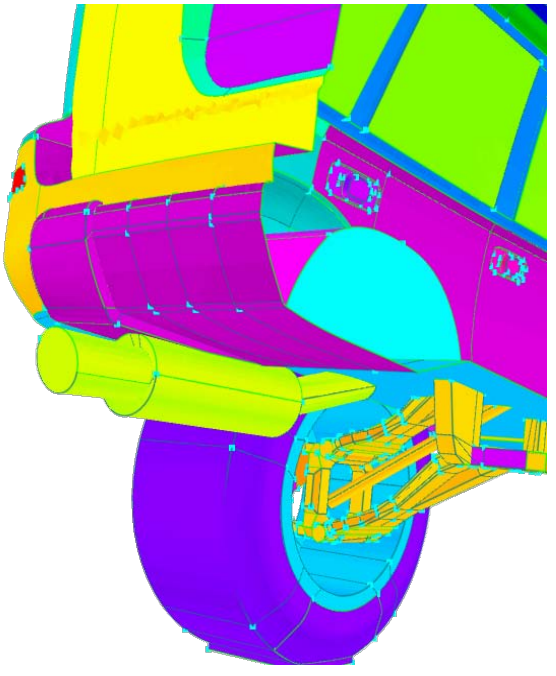

(c) Rear underbody components

Figure 2.4: Geometric model of the Nissan XTrail sport utility vehicle.

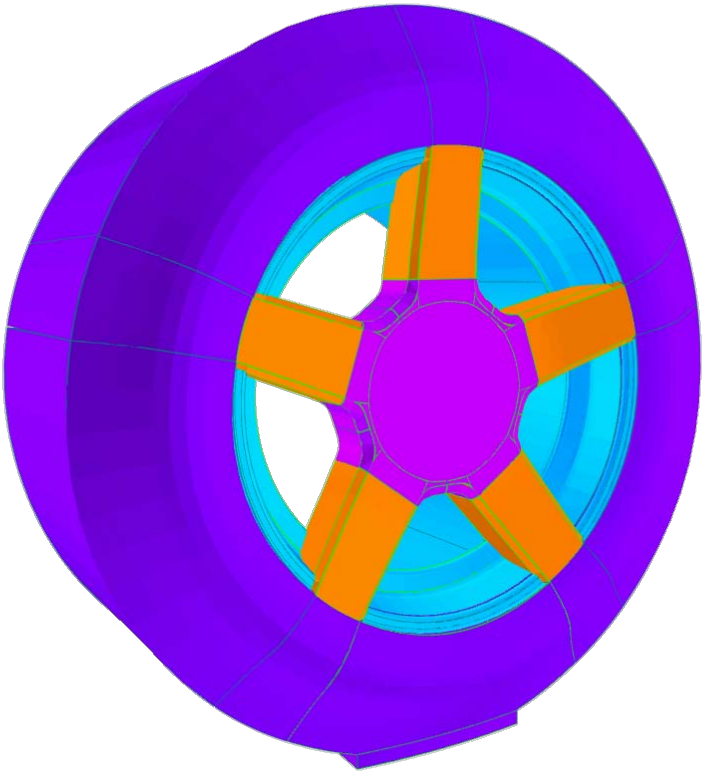

Figure 2.5: Geometric model of the tire, wheel, and rim.

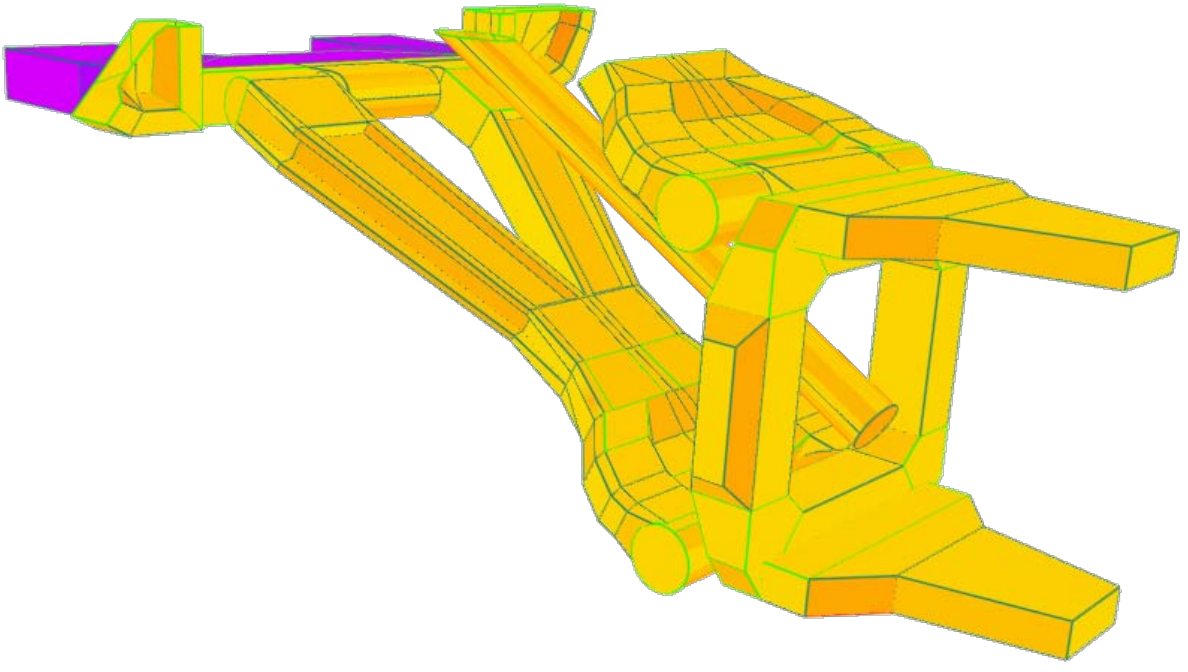

Figure 2.6: Geometric model of the suspension.

2.3 Mesh generation

After the completion of the topologically valid geometric model, the next step involved suitably discretizing the model for the blast simulation. To discretize the model in SolidMesh, grid point spacings were applied to all of the geometric vertices. The point spacing values were used to control the local element size. The nominal point spacing on the vehicle body wass 1.25*cm*. Some regions required a locally smaller point spacing to adequately represent the geometric detail. For the suspension, wheels, brush guard, underbody and other geometric details, a nominal spacing of 3.125*mm* was used. The global surface grid was then generated surface by surface.

Mesh generation using SolidMesh is an automated process using advancing front/local reconnection algorithms. The edge grid generation is automatically generated using a one-dimensional advancing front along the curves advancing from the geometric vertices. The surface mesh generation is automatically generated using a two-dimensional advancing front advancing from the surface boundaries (i.e., the curves). The volume mesh generation is automatically generated using a three-dimensional advancing front advancing from the surfaces.

The geometric model shown in Figure 2.4 consists of 1,834 geometric surfaces. In order to create a watertight or topologically valid geometric model, some of the created surfaces had highly acute angles, i.e., sliver surfaces, which can negatively impact the surface mesh quality and present difficulties for the flow solver. Therefore, the composite surface capability within SolidMesh was used to generate a surface mesh of suitable quality. A composite surface is a collection of surfaces that, for mesh generation purposes, is treated as a single topological entity.

An example of a sliver surface is illustrated in Figure 2.7(a). This highlighted region, isolated and magnified in Figure 2.7(b), is part of the vehicle trim molding on the front quarter panel. It consists of nine surfaces, for which the mesh is shown in Figure 2.7(c). As illustrated, the mesh quality is poor due to the surface topology. A composite surface was created using these nine component surfaces, and the resulting surface mesh is shown in Figure 2.7(d). Without the constraints of the interior geometric edges, the composite surface mesh is more isotropic and results in a better quality mesh. The minimum angle in the composite surface mesh is increased from 7.2 degrees to 30.7 degrees and the maximum angle decreased from 122.5 degrees to 98.1 degrees. Significantly, there is no approximation in the final composite surface mesh, i.e., the surface grid points for the composite surface lie on the original geometric surface. The composite surface does not modify the underlying geometric definitions of a geometric surface, unlike a carpet surface which projects and interpolates the data. A total of 76 composite surfaces, consisting of 383 component surfaces, were defined. The locations of the composite surfaces (highlighted in yellow) are shown in Figure 2.8.

For the blast simulation, an isotropic (i.e. no boundary-layer resolution) unstructured volume mesh is suitable. In order to decrease the volume grid generation time, a volume mesh was generated for the half-plane geometric model. This half-plane volume mesh was then reflected about the vehicle plane of symmetry to obtain the volume mesh of the full vehicle. The final SUV surface mesh is shown in figure 2.9 and consists of 626,843 nodes and 1,253,858 triangles. The full vehicle volume mesh contains 4,765,060 nodes and 26,429,880 tetrahedra. The minimum dihedral angle of the volume mesh = 9.75 degrees and the maximum dihedral angle = 159.7 degrees. To provide a sample of the field resolution, cutting planes were taken at various locations throughout the volume mesh (Figure 2.10). A cutting plane taken along the vehicle symmetry plane is shown in figure 2.10(a), and cutting planes taken near the suspension, brush guard, and side view mirror are shown in figures 2.10(b), 2.10(c), and 2.10(d), respectively.

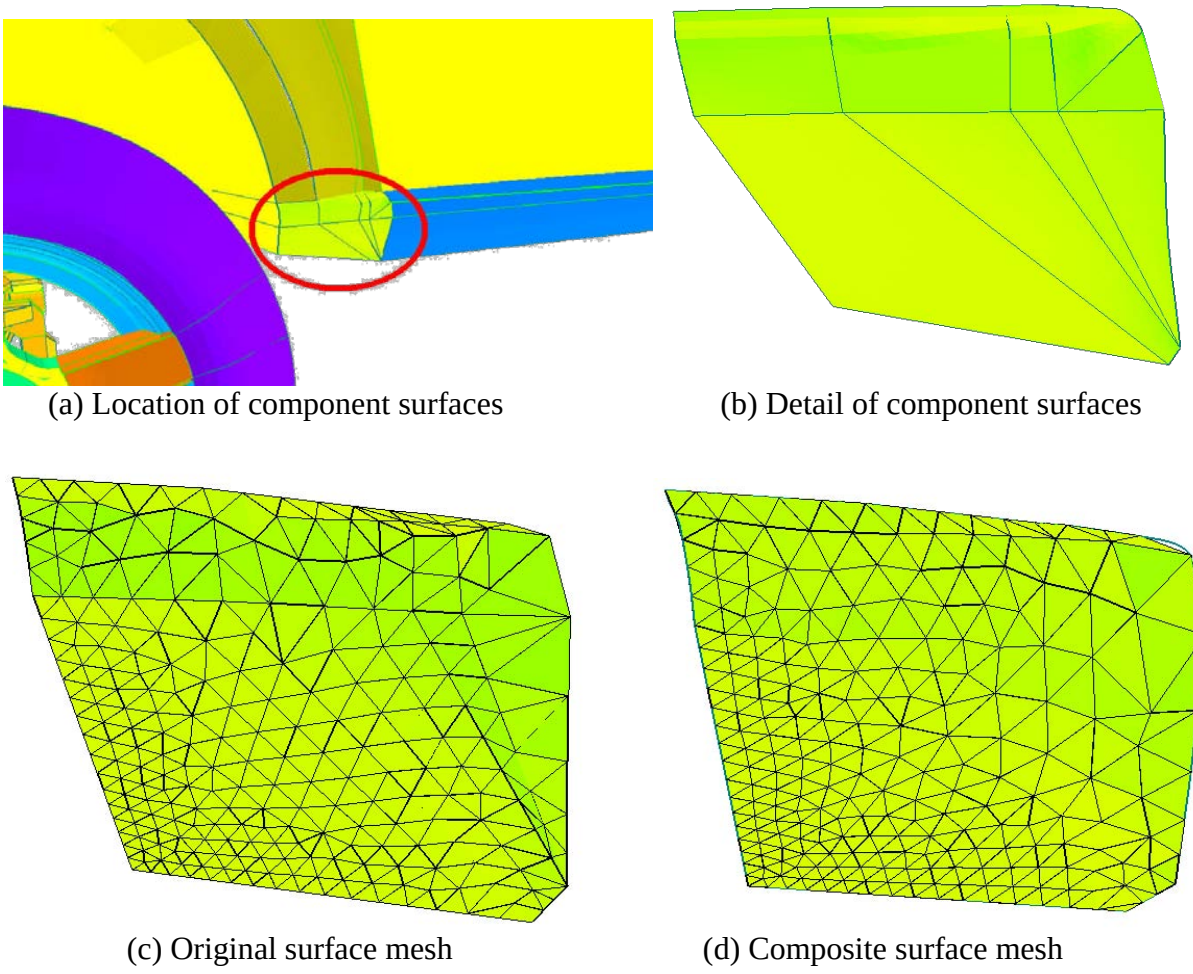

(a) Location of component surfaces (b) Detail of component surfaces

(c) Original surface mesh (d) Composite surface mesh

Figure 2.7: Composite surface example for surfaces with poor topology.

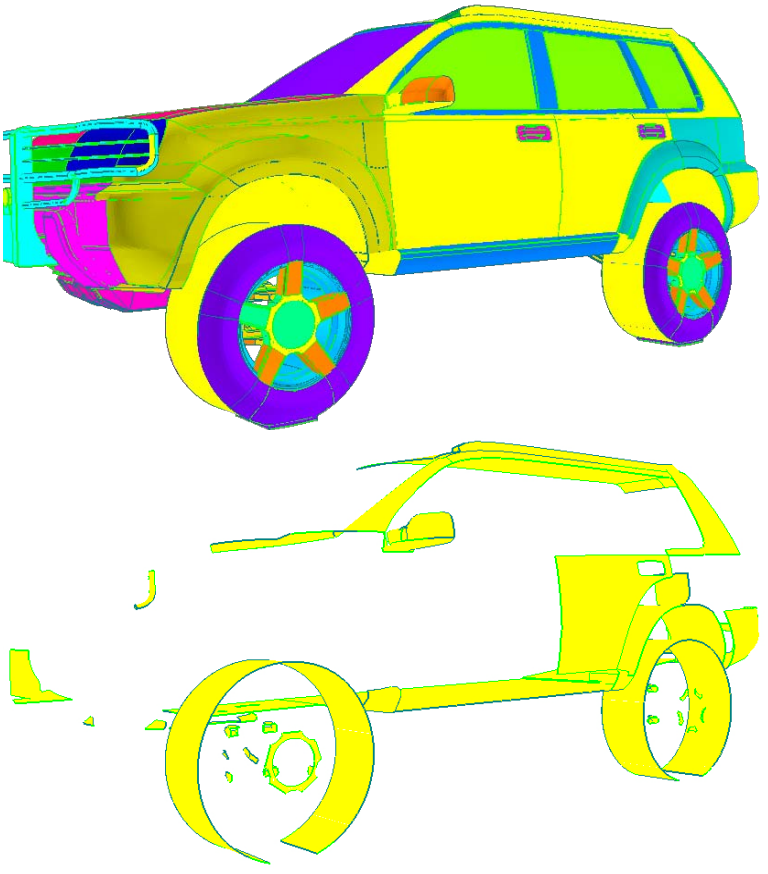

Figure 2.8: Composite surface definitions for the Nissan XTrail sport utility vehicle.

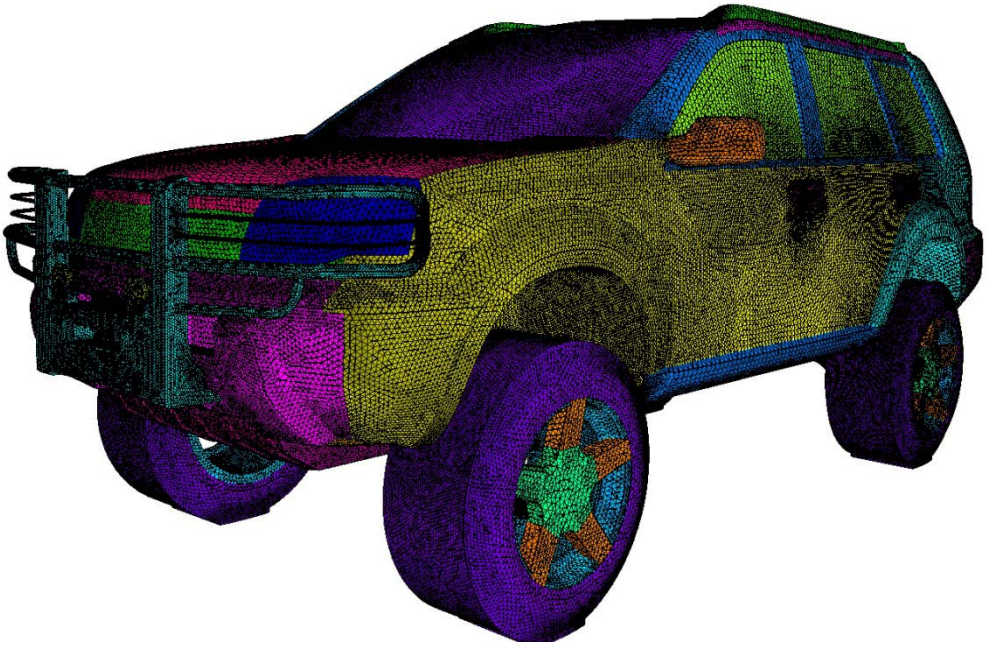

Figure 2.9: Surface mesh for the Nissan XTrail sport utility vehicle.

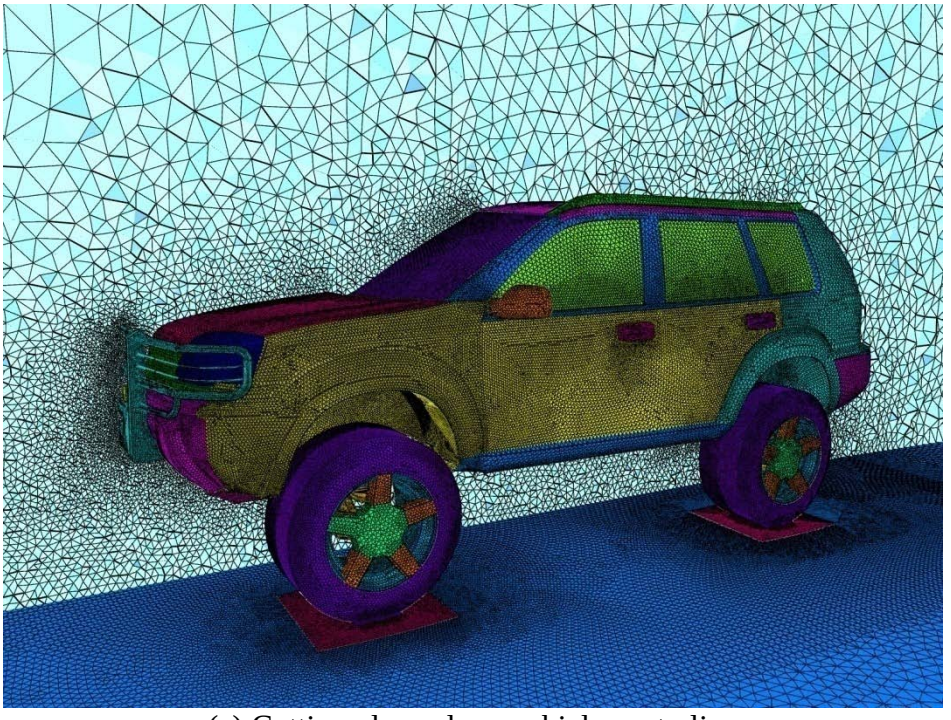

(a) Cutting plane along vehicle centerline

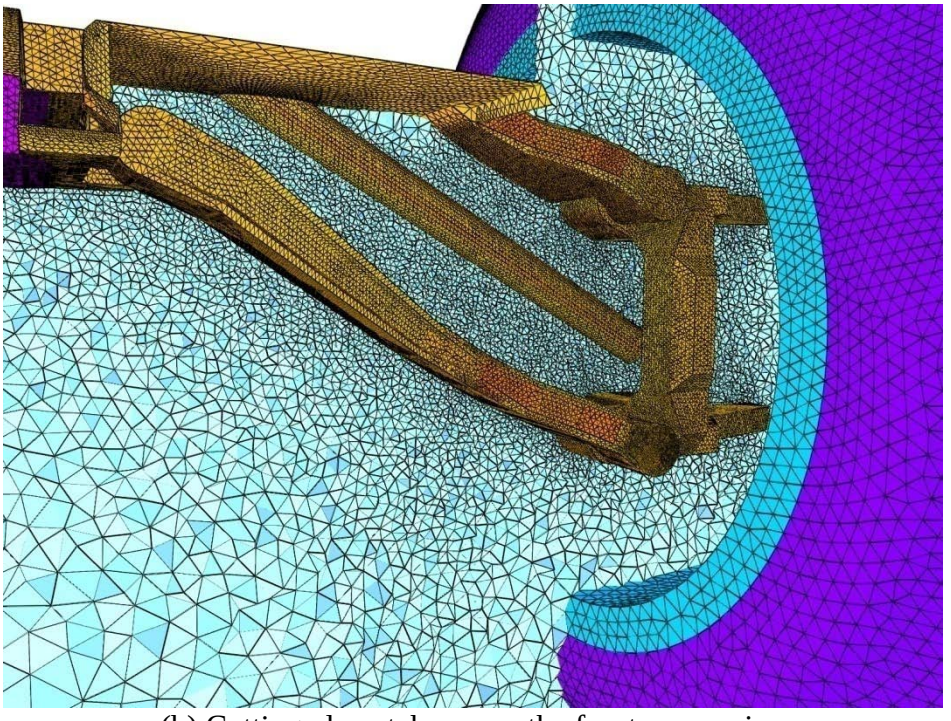

(b) Cutting plane taken near the front suspension

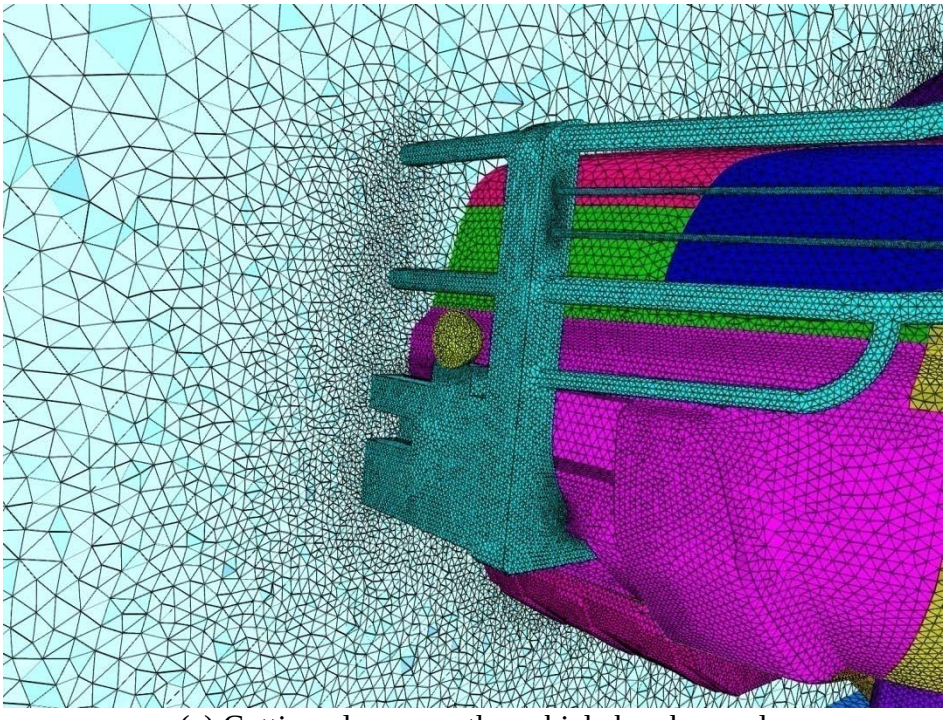

(c) Cutting plane near the vehicle brush guard

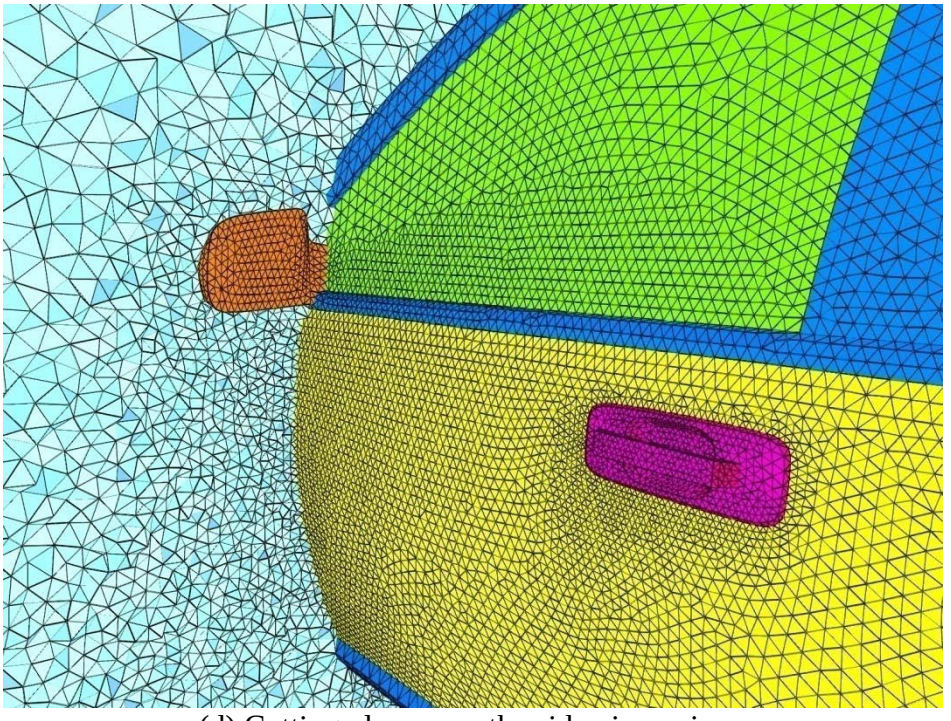

(d) Cutting plane near the side view mirror

Figure 2.10: Volume grid cutting planes.

2.4 Blast simulations for rigid vehicle

Our previous validation results indicate that O(1) *mm* mesh spacings are necessary to capture the initial phases of the detonation. However, this spacing can be relaxed significantly as the blast wave evolves. To reduce computational costs, the approach we employed for the blast-vehicle interaction initiated the blast simulation for a cylindrical charge as an axisymmetric computation and ran this simulation until the outer shock wave had propagated a suitable distance. At this point, the axisymmetric blast solution was interpolated onto the SUV mesh and the computation initiated.

WD0019 does not specify the number of cases to be simulated nor does it specify the position, mass, or composition of the charge. In an email (dated June 18, 2009), TARDEC personnel suggested that we use 15kg C-4. The C-4 charge was defined to be a cylinder with a diameter of 35.76418cm and a height of 8.9410cm. Two cases were simulated using different charge locations. In the first case, hereafter refered to as the "undertire" case, the geometric center of the bottom face of the charge was located on the ground plane 31.558cm ahead of the front axle and 2.8379cm to the right of the tire symmetry plane at the point labeled "A," as shown in Figure 2.11. The second case, denoted as the "centerline" case, had the charge placed under the occupants on the vehicle centerline appoximately 98.525cm behind the axle. In the "centerline" case, the vehicle plane of symmetry was used as a plane of symmetry in the computational domain in order to reduce the cost. Each simulation was run until a physical time of 1000μs elapsed. In each case, detonation was initiated at the center of the charge. The HLLE flux definition was used [Einfeldt, 1988]. An explicit, second-order Runge-Kutta time integration algorithm was employed with the time step defined based on a maximum permitted CFL number of 0.75. The approach employed to simulate the detonation and subsequent blast is discussed in detail in Section 3.

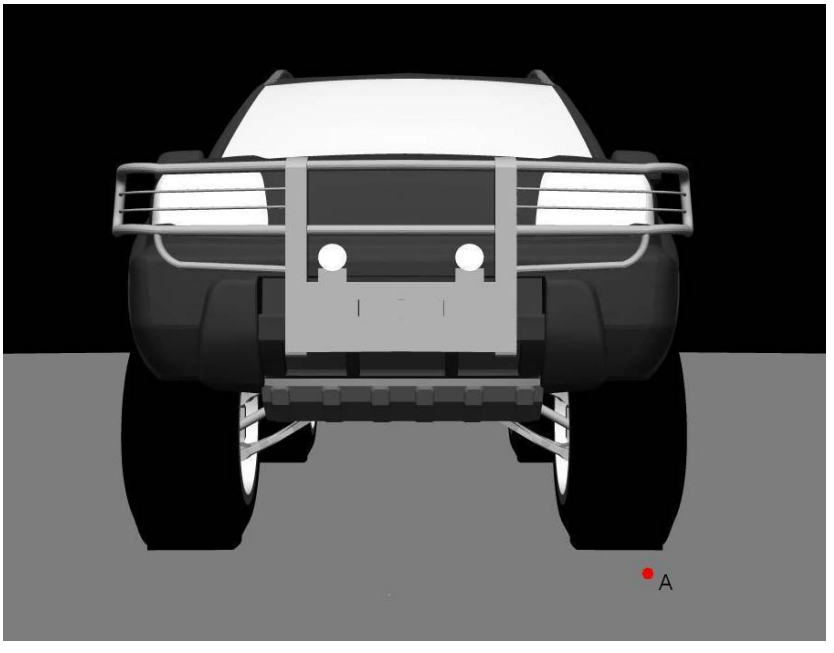

Figure 2.11: Position of 15kg C-4 charge for "undertire" case.

Two sets of animations were generated, one for each charge position. Many of the phenomena visible in the animations are also visible in static images. Figures 2.12-2.14 show sequences of images generated from the "undertire" simulation at times t=207μs, 407μs, 607μs, 807μs, and 1007μs. Figure 2.12 illustrates the evolution of an isosurface of the JWL gas mass fraction colored by local pressure (in units of Pa). This variable was chosen for the isosurface because it provides a good approximation to the blast front. The impact of the cylindrical shape of the charge on the blast front is evident in Figure 2.12(a). The complexity of the flow interactions with the wheels and wheel wells is apparent in Figures 2.12(b)-2.12(e). Figure 2.13 shows the vehicle and the ground plane shaded by local pressure. Numerous complex wave patterns due to wave interactions and flow interations with the geometry are present on the vehicle and the ground plane. Of interest are the diffraction patterns shown in Figures 2.13(c) and 2.13(d) due to the interaction of shocks with the front tires. Figure 2.14 shows the vehicle underbody shaded by local pressure. Again, the numerous wave interactions illustrate the complexity of the flow underneath the vehicle. This is particularly evident in figure 2.14(c), which clearly shows several shock-shock interactions. By approximately 1000μs from the initiation of the blast, the pressure over most of underbody shown in the image is approaching the original pressure.

Figures 2.15-2.17 show a similar set of plots for the "centerline" case. The complexity of the resulting flow is evident from the figures. Figure 2.16 shows complex diffraction patterns in the ground plane due to the interaction of shock waves with the tires. Complex wave interactions are again present on the underbody, as shown in figure 2.17.

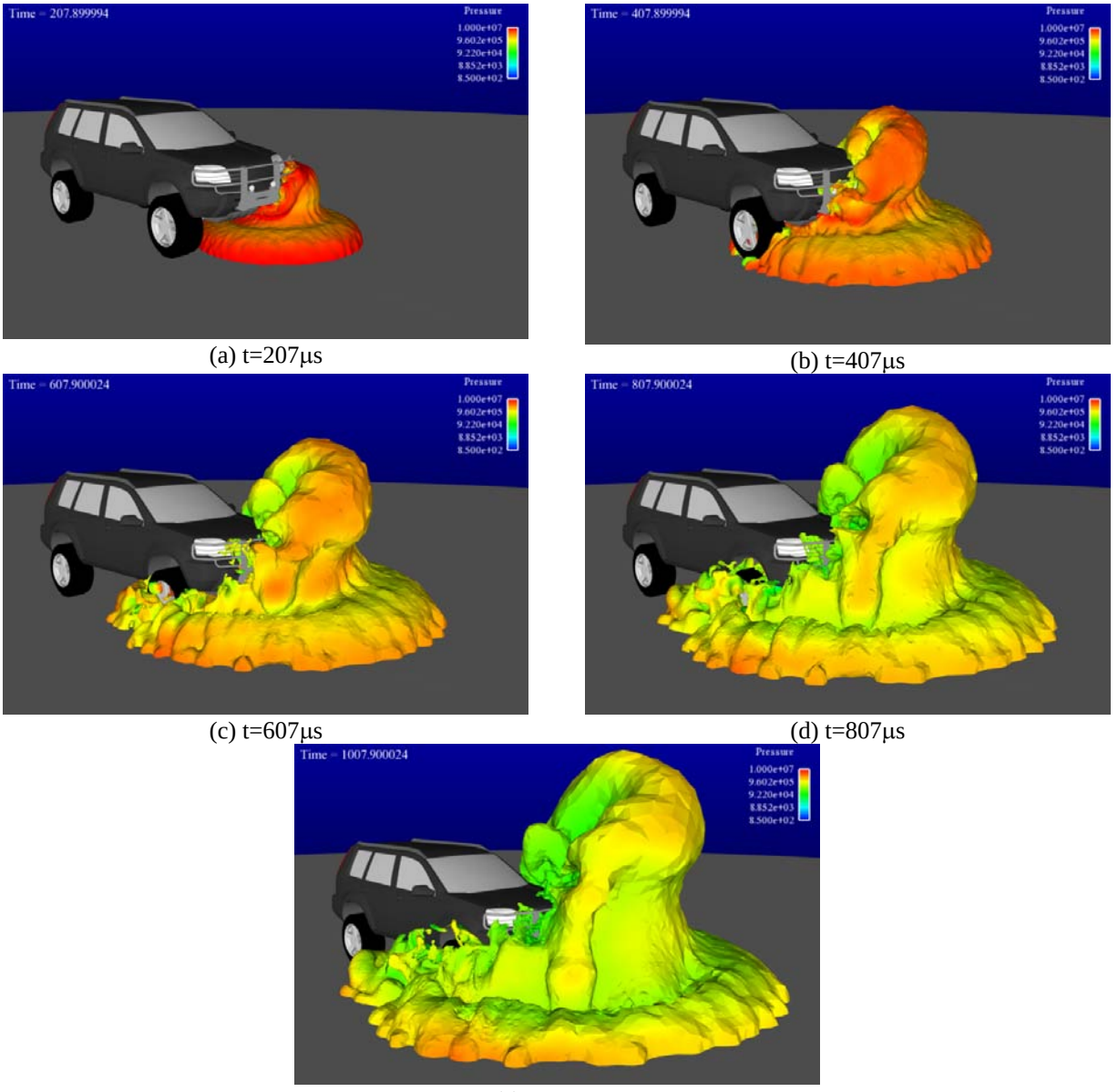

(a) t=207μs (b) t=407μs

(c) t=607μs (d) t=807μs

(e) t=1007μs

Figure 2.12: "Undertire" blast simulation – Isosurface of JWL gas mass fraction colored by local pressure.

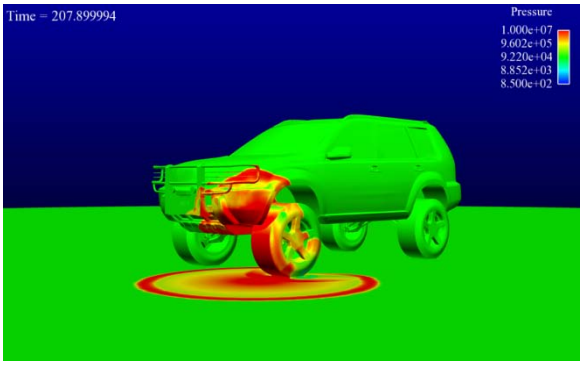

(a) t=207μs

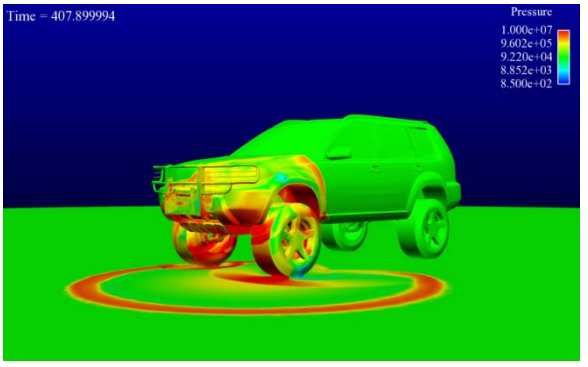

(b) t=407μs

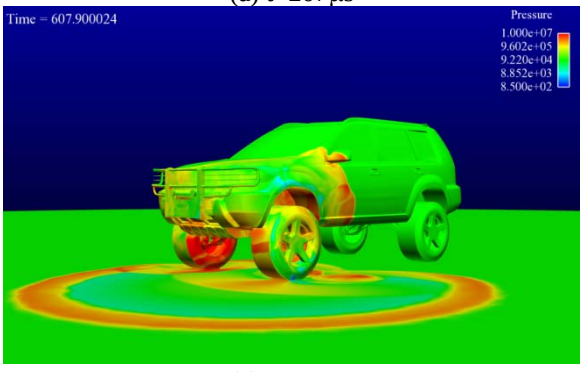

(c) t=607μs

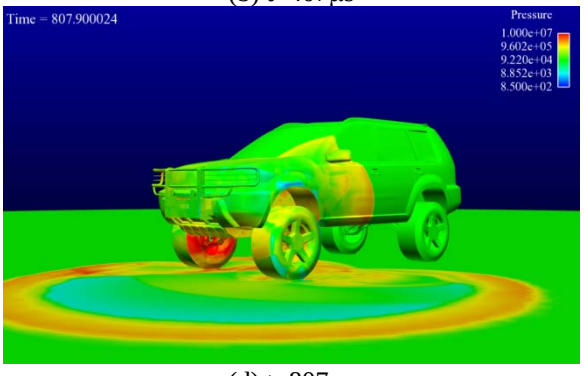

(d) t=807μs

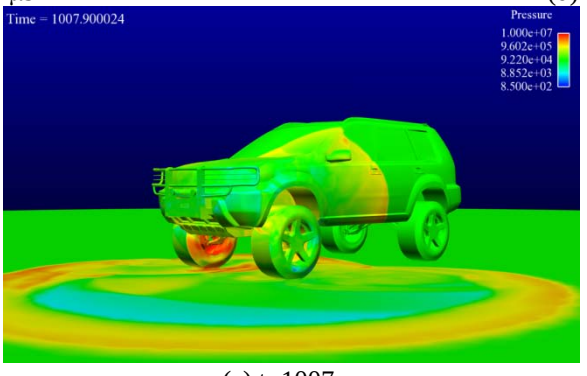

(e) t=1007μs

Figure 2.13: "Undertire" blast simulation – Surfaces shaded by local pressure.

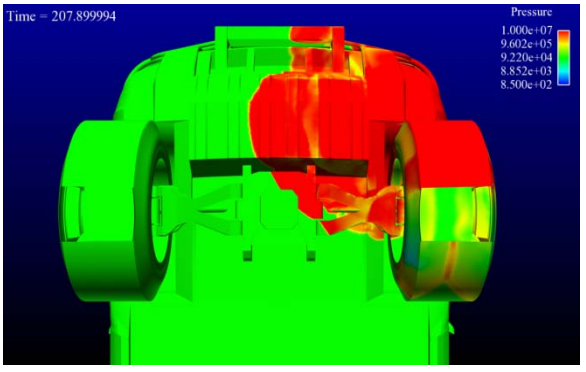

(a) t=207μs

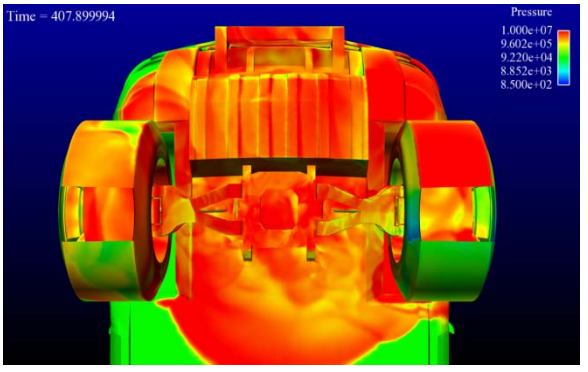

(b) t=407μs

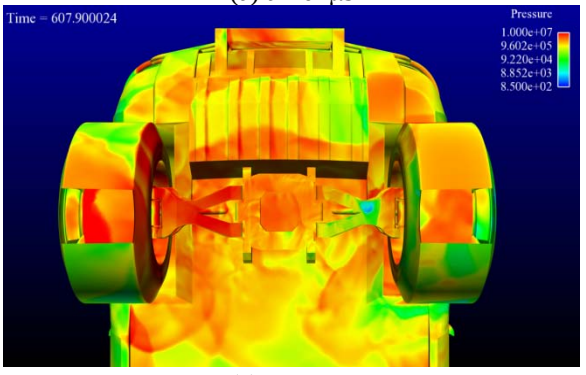

(c) t=607μs

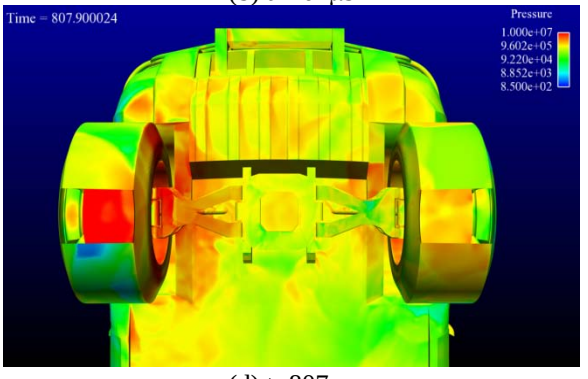

(d) t=807μs

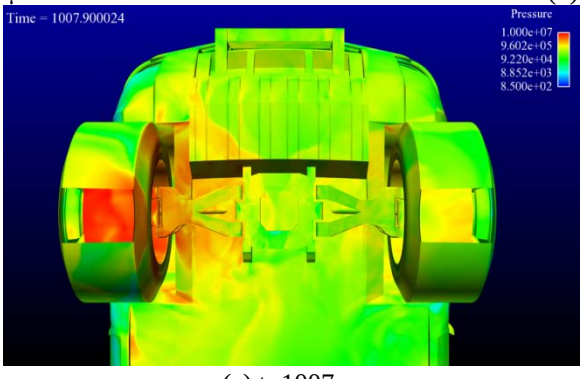

(e) t=1007μs

Figure 2.14: "Undertire" blast simulation – Surfaces shaded by local pressure.

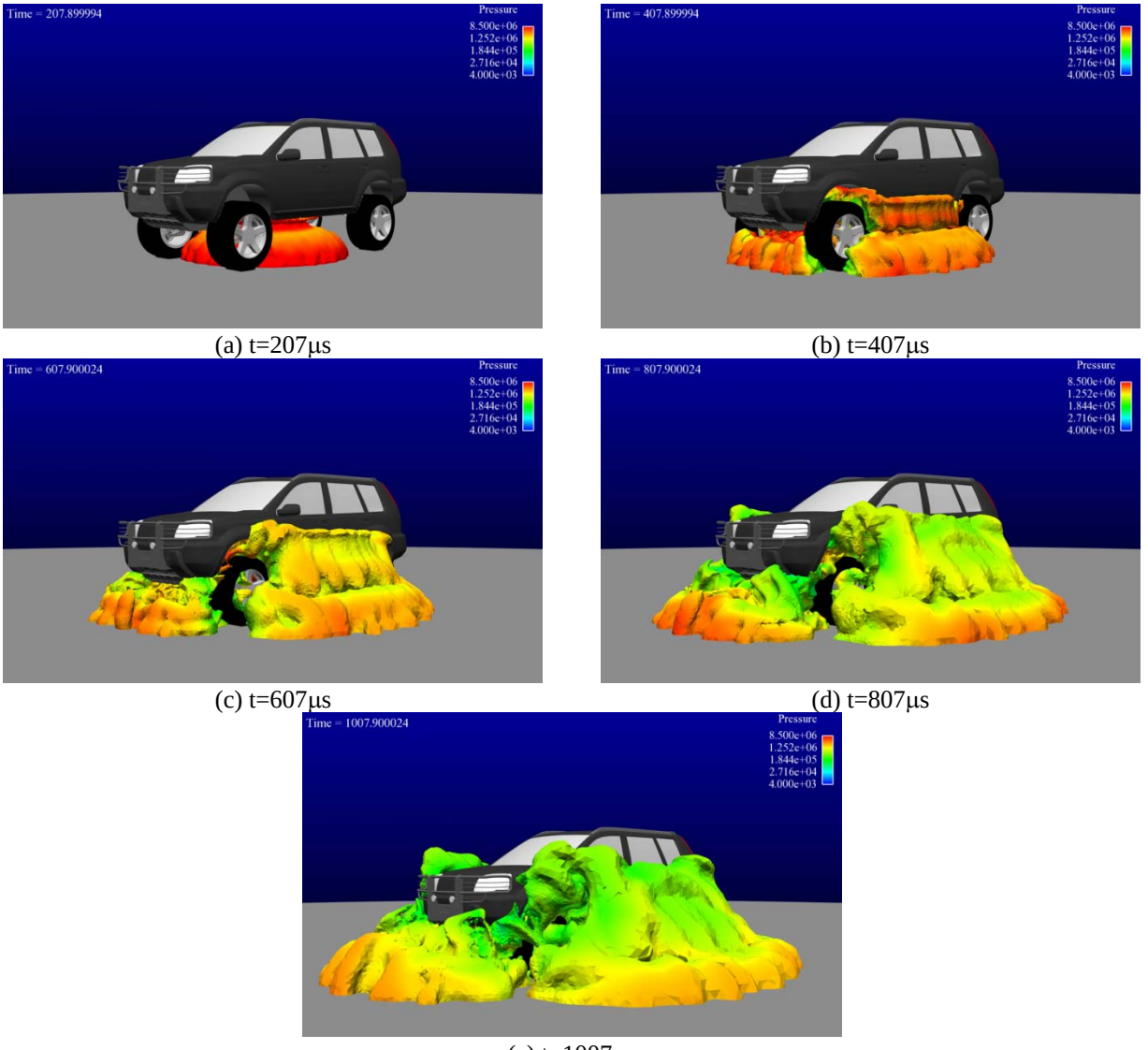

(a) t=207μs (b) t=407μs

(c) t=607μs (d) t=807μs

(e) t=1007μs

Figure 2.15: "Centerline" blast simulation – Isosurface of JWL gas mass fraction colored by local pressure.

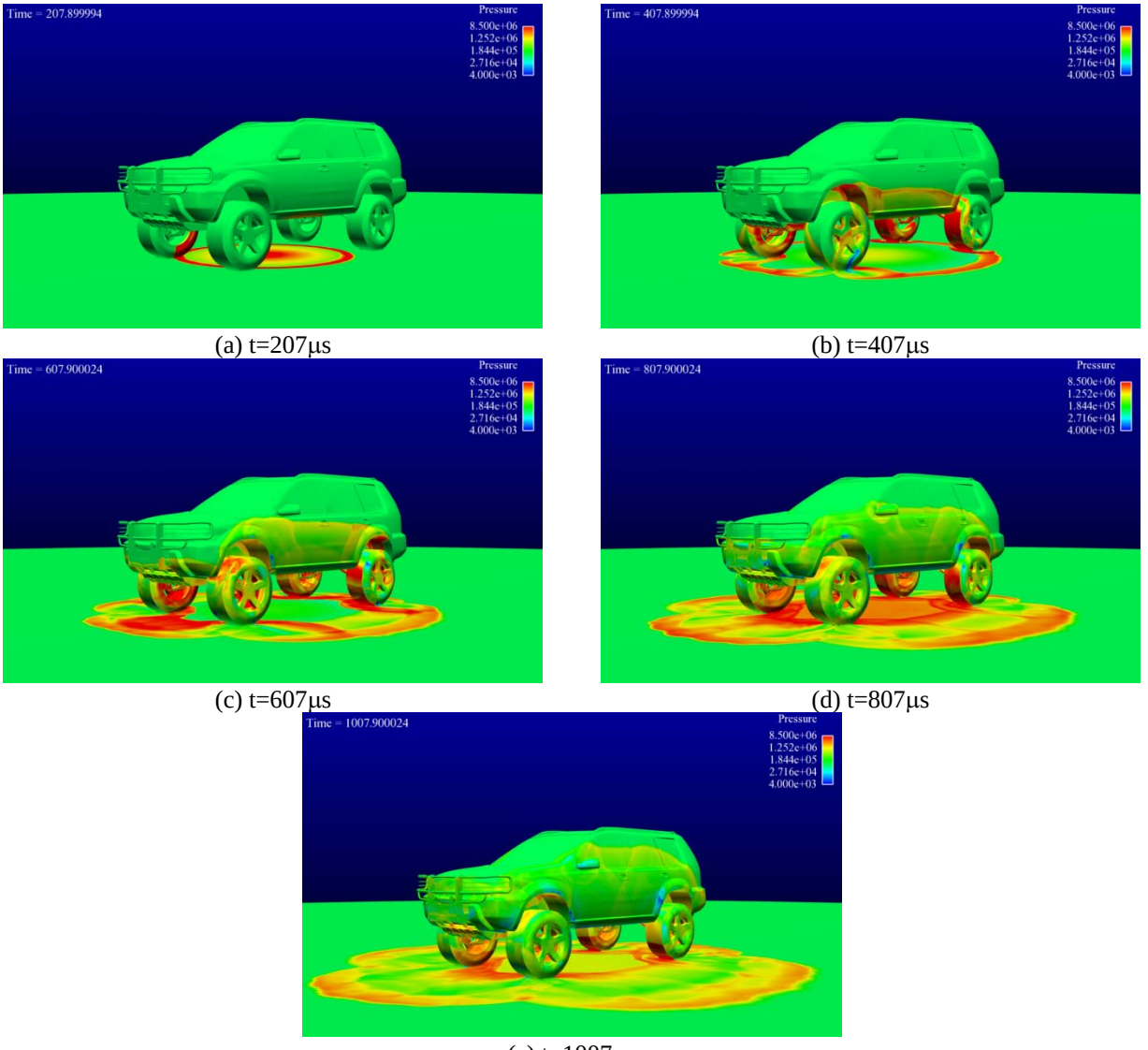

(a) t=207μs (b) t=407μs

(c) t=607μs (d) t=807μs

(e) t=1007μs

Figure 2.16: "Centerline" blast simulation – Surfaces shaded by local pressure.

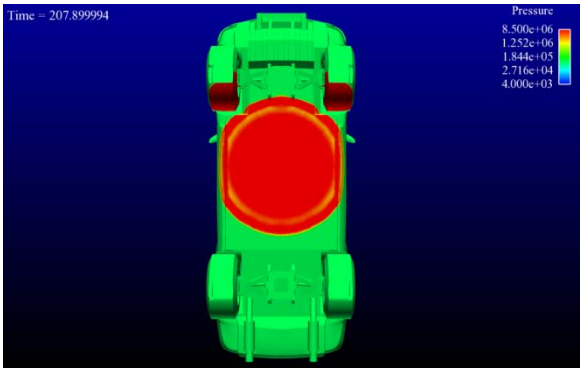

(a) t=207μs

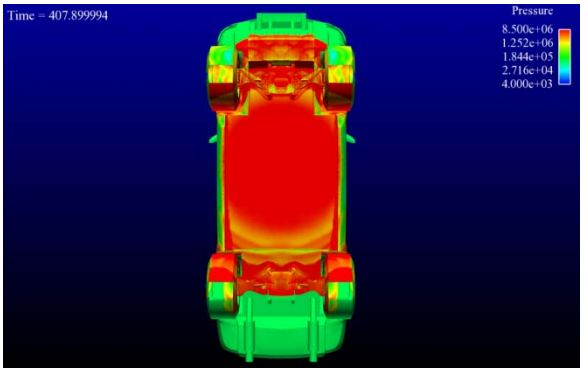

(b) t=407μs

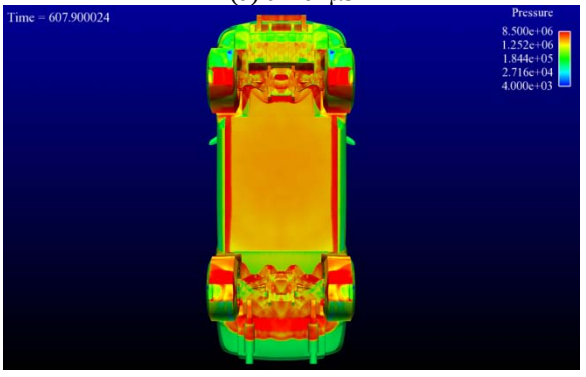

(c) t=607μs

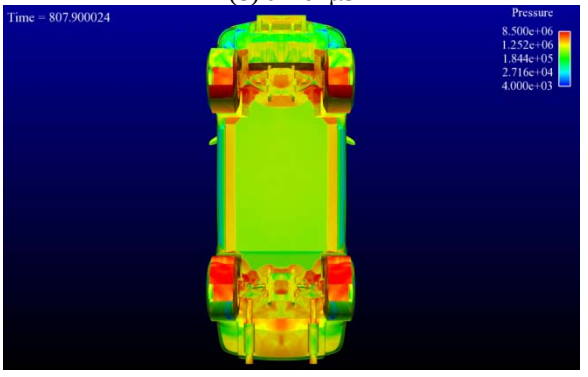

(d) t=807μs

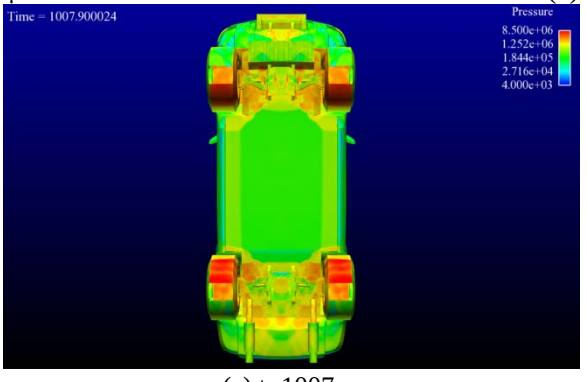

(e) t=1007μs

Figure 2.17: "Centerline" blast simulation – Surfaces shaded by local pressure.

Section 3: Implementation of models to simulate blast-soil interactions

3.1 Governing equations for the soil/blast modeling

The governing equations for our soil-blast model is that of a multicomponent inviscid flow assuming thermal, pressure, and velocity equilibriation between all materials in any given location of space. These equations are given by the conservation of component mass, momentum, and energy. The conservation of component mass is given by the equation

$$\frac{\partial \rho_i}{\partial t} + \nabla \bullet (\rho_i \vec{u}) = 0, \forall i \in \{1 \ldots NS\}, \tag{3.1}$$

where ρ_i is the component density of material i, and $\vec{u}$ is the material velocity vector. Note that the overall material density at any point in space is given by $\rho = \sum_{i=1}^{NS} \rho_i$. The momemtum conservation equation is given by

$$\frac{\partial \rho \vec{u}}{\partial t} + \nabla \bullet (\rho \vec{u} \vec{u}) = \nabla p, \tag{3.2}$$

where p is the pressure of the component mixture. The conservation of energy is given by the equation

$$\frac{\partial \rho e_0}{\partial t} + \nabla \bullet [(\rho e_0 + p)\vec{u}] = 0, \tag{3.3}$$

where e_0 is the total of fluid kinetic energy and internal energy given by the expression

$$e_0 = \frac{1}{2}\vec{u} \cdot \vec{u} + e_{\text{int}\,ernal}. \tag{3.4}$$

These equations are closed by a multicomponent equation of state that relates pressure to the material densities of the components and the internal energy as represented by $p = P(\rho_1, \rho_2, \cdots, \rho_{NS}, e_{\text{int}\,ernal})$. The formulation of this equation-of-state will be central to the soil and blast gas models, They will be derived from a mixture rule that combines single component equations of state for each material, assuming pressure and thermal equilibriation.

3.2 A multicomponent equation of state for blast modeling

To support non-ideal equations of state for blast modeling using the explicit time integrator, we required a highly robust density-energy query capability. Our mixing rule assumes that our materials are immiscible and are in mechanical (pressure) and thermal equilibrium. In this mixing rule, we assume that we have a mixture of species equations of state which define pressure as a function of density and temperature. Using the immiscible assumption, we find the volume of the mixture is the sum of the volume occupied by each species, or

$$\frac{1}{\rho} = \sum_{i=1}^{NS} \frac{Y_i}{\rho_i^*}, \tag{3.5}$$

where Y_i is the species mass fraction and ρ_i^* is the density of pure material i at a given temperature and pressure.

$$p=p_i(\rho_i^*,T)\forall i\in[1..NS], \tag{3.6}$$

where $p_i(\rho_i^*,T)$ is the equation of state for species i, and p is the system pressure. The energy of mixture is given by the mass averaged species energies, as in

$$e=\sum_{i=1}^{NS} Y_i e_i(T,\rho_i^*), \tag{3.7}$$

where the species energy equation is given by

$$e_i\left(T,\rho_i^*\right)=e_{f,i}+\int_{T_o}^{T} c_{v,i}(\tau)d\tau+\left[e_i\left(T,\rho_i^*\right)-e_i(T)_{pg}\right], \tag{3.8}$$

where the last term of this expression is the departure function that accounts for the effects of non-ideality in the equation of state. Note, equation (3.8) is simply a trivial regrouping of the energy components that allows us to view the energy of a species as a division of thermally perfect and thermally imperfect components. Thus the departure function is viewed as the deviation of the energy equation from a thermally perfect gas. The departure function can be computed using the relation:

$$\left[e_i\left(T,\rho_i^*\right)-e_i(T)_{PG}\right]=\int_0^{\rho_i^*}\left[p-T\frac{\partial p\left(\rho_i^*,T\right)}{\partial T}\right]\frac{d\rho_i^*}{\rho_i^{*2}}. \tag{3.9}$$

Equations (3.5), (3.6), and (3.7) describe *NS*+2 nonlinear equations and *NS*+4 unknowns (the unknowns are the species specific volumes, $1/\rho_i^*$, and the thermodynamic variables P, T, ρ, and e). Given any two thermodynamic state variables, this system of equations can be solved to find the remaining thermodynamic variables along with the specific volumes implied by the species pure substance densities, ρ_i^*. Due to the non-linearities in these equations, robustly solving for the thermodynamic state, given the fluid density and energy (as will be required by the explicit time integrator), can be a significant challenge. The most straightforward approach is to use a multi-dimensional Newton method. However, when the initial guess is far away from the final solution, it can be difficult to reliably converge to a solution. We have developed an alternative approach that is robust, but perhaps with a sacrifice in computational efficiency.

To obtain a robust solution to the above non-linear equations, we have made the observation that if we solve for pressure and temperature instead of density and energy, the pressure equation, i.e., equation (3.6), decouples and we can then solve *NS* non-linear scalar equations. Since non-linear root finding for scalar equations can be made robust using root bracketing techniques, a pressure-temperature query has a very robust solution. Can we utilize this observation to make a robust density-energy EoS query? Yes, through an indirect route. First, we can obtain a robust

density-temperature query by performing a bracketed-scalar solve for the pressure. This iterative solve can utilize the robust pressure-temperature query; in addition, it is expected that pressure will increase monotonically with temperature. Finally, given a robust density-temperature query, a robust density-energy query can be formulated by solving for the temperature that gives the specified energy. All of these queries are solved using a bracketed Newton method whereby the values that bracket a solution are identified. If the Newton method overshoots the bracket, the robust bisection method is utilized for that step. The resulting EoS query evaluator has been shown to be robust in practice.

3.3 Species equations of state

This section will outline the species equations of state implemented for blast wave modeling and provide a description of the definition of pressure and energy for each species. The energy for each of these species is derived using the departure function in equation (3.9).

Perfect gas

The perfect gas equation of state provides the basic equation of state for thermally and calorically perfect materials. The equation of state for a perfect gas is given by the relation:

$$p_i(\rho_i^*, T) = \rho_i^* \frac{\hat{R}}{m_i} T, \tag{3.10}$$

where m_i is the molecular mass of species i and $\hat{R}$=8314.3J/($Kkmol$) is the universal gas constant. The energy is given by the relation:

$$e_i(\rho_i^*, T) = n_i \frac{\hat{R}}{m_i} T + h_{fi}, \tag{3.11}$$

where h_{fi} is the heat of formation for species i and is defined by the reference enthalpy at the specified reference temperature. For air, the perfect gas model is specified in the Loci/CHEM `.mdl` file as

```
// Air as an ideal gas
_Air   = < m=28.89, n=2.5, href=0, sref=0, Tref=298.0,
Pref=10000.0 > ;
```

JWL gas

The JWL equation of state defined in density-temperature form as utilized by Lee and Tarver [Lee and Tarver, 1980] defines pressure as the relation:

$$p_i(\rho_i^*, T) = A\exp\left(-R1\frac{\rho_0}{\rho_i^*}\right) + B\exp\left(-R2\frac{\rho_0}{\rho_i^*}\right) + \omega C_v T \frac{\rho_i^*}{\rho_0}, \tag{3.12}$$

where ρ_0 is the density of the explosive material pre-detonation, ω, A, B, $R1$, and $R2$ are coefficients of the JWL EoS, and C_v defines the gas specific heat of the expanded gas. Note, the default units for A and B are Pascals, while C_v is Pascal/kelvin. Utilizing the departure equation, equation (3.3.9), the energy for this species is found to be defined by the following relation:

$$e_i(\rho_i^*,T)=\frac{A}{R1\rho_0}\exp\left(-R1\,\frac{\rho_0}{\rho_i^*}\right)+\frac{B}{R2\rho_0}\exp\left(-R2\,\frac{\rho_0}{\rho_i^*}\right)+\frac{C_vT}{\rho_0}. \tag{3.13}$$

A species is prescribed by the JWL EoS by assigning the EoS parameter in the Loci/CHEM model file. For example, the JWL EoS for the explosive C-4 is given by the following species model definition:

```
// Explosive gases released under detonation of C-4
_jwlgas   = <m=45,n=3.3, href=0,sref=0.0,Tref=0,Pref=0,mf=0 > ;
_jwlgas: <eos=JWL(A=609.77e9,  B=12.95e9, omega=0.25,
R1=4.5,R2=1.4,
                  rho_0=1601,Cv=1e6)> ;
```

Note, the molecular weight, `m` and partition function parameter, `n`, do not need to be set to a specific values as they will be redefined to match the ω and C_v provided in by the JWL EoS.

Elastic solid

The equation of state for a perfectly elastic solid can be defined by the simple linear barytropic equation of state given by the relation:

$$p_i(\rho_i^*,T)=K\left(\frac{\rho_i^*}{\rho_0}-1\right)+P_0, \tag{3.14}$$

where K is the bulk modulus of the material, and ρ_0 is the material density at a given reference pressure, P_0. Utilizing equation (3.3.9), the energy[1] for the elastic solid EoS is given by

$$e_i(\rho_i^*,T)=\frac{K-P0}{\rho_i^*}+\frac{K}{\rho_0}\ln(\rho_i^*)+n_i\frac{\hat{R}}{m_i}T+h_{fi}. \tag{3.15}$$

Note, in describing an elastic solid, the following properties must be defined: the material density at a given reference pressure, the material bulk modulus, and set `m` and `n` to achieve the material C_v. For example, the material quartz has a specific heat, C_v=733J/kgK; thus if we set the

[1]Note: We cannot integrate to a zero density for an elastic solid. However, the relation will hold for any arbitrary constant of integration with the interpretation that we are integrating from some given reference density, ρ_0. Since the absolute value of the energy is not critical we absorb this constant of into the heat of formation term, h_{fi} of this species.

molecular weight to 1 we can compute $n=C_v/\hat{R}=0.0882$. Since quartz has a density of $2650 kg/m^3$ and a bulk modulus of $K=36.4\times10^9 Pa$, the model for quartz using an elastic solid is specified as:

```
// Quartz as an elastic solid
_quartz = < m=1,n=.0882,href=0, sref=0.0,Tref=0,Pref=0,mf=0 > ;
_quartz : <eos=ElasticSolid(rho_0=2650,K=36.4e9,P0=1e5) > ;
```

Tait EoS for liquid water

The Tait EoS is a simple and accurate barytropic equation of state for liquid water under high pressure. This equation of state is given by the relation:

$$p_i\left(\rho_i^*, T\right) = B\left[\left(\frac{\rho_i^*}{\rho_0}\right)^{\gamma} - 1\right] + A, \quad (3.16)$$

where ρ_0 is the material density at reference pressure given by coefficient A, B is an empirically determined coefficient, and γ is the material exponent. This equation of state can model liquid water with the following coefficients: $A=10^5 Pa$, $B=3.31\times10^8 Pa$, $\rho_0=1000 kg/m^3$, and $\gamma=7.15$. The energy as defined by the departure function for this EoS is expressed by the relation:

$$e_i\left(\rho_i^*, T\right) = \frac{B-A}{\rho_i^*} + \frac{B}{(\gamma-1)\rho_0}\left(\frac{\rho_i^*}{\rho_0}\right)^{\gamma-1} + n\frac{\hat{R}}{m}T + h_{fi}. \quad (3.17)$$

For this equation of state, the material specific heat, C_v can be set using the same procedure as described for the elastic solid. The model input to describe liquid water is given by the following material definition:

```
_water= <m=1,n=.50341,href=0,sref=0,Tref=0,Pref=0,mf=0 > ;
_water: <eos=Tait(A=1e5,B=3.31e8,gamma=7.15,rho_0=1000) > ;
```

3.4 Modeling a prescribed explosive burn

We have developed a prescribed burn capability that can be used to simulate the propagation of a detonation front through the explosive material. The current model assumes that the explosive is initiated from a single point and that there are no obstructions to the detonation front. In the prescribed explosive burn methodology, the initiation point and a detonation velocity are provided by the user. The explosive burn is accomplished by converting the solid explosive material into the corresponding gas material as the detonation wave passes each given point in the mesh. Usually the solid explosive before detonation is modeled as an elastic solid, while gasses released by the burn are modeled using the JWL EoS. To accomplish the appropriate energy release during the burn, the heat of formation of the solid explosive material is set such that the proper heat release is achieved.

The detonation front is computed by enforcing a burn fraction that is a function of the lighting time, t_1. The lighting time is the computed time that the detonation front will arrive at a given cell and is computed by dividing the distance to the initiation point by the detonation velocity, D. The burn fraction, F, is zero if $t \le t_1$. When $t > t_1$, the burn fraction is defined by

$$F = \max\left(\frac{(t-t_1)D}{4\Delta}, \frac{1-V}{1-V_{CJ}}\right), \tag{3.18}$$

where t is the current simulation time, t_1 is the current cell lighting time, D is the detonation velocity, $V = \frac{\rho_0}{\rho}$ is the relative volume, V_{CJ} is the relative volume at the Chapman-Jouguet conditions, and Δ is an estimated grid spacing for the mesh where the detonation front is propagating.

The explosive burn is enabled by adding the `explosiveBurnModel` option to the Loci/CHEM `.vars` file. This input specifies the initiation point, the detonation velocity, the Chapman-Jouguet pressure, and the species that describe the solid and gas components of the explosive material. An example used for C-4 explosive is as follows:

```
// initiate in center of charge
explosiveBurnModel: < initiationPoint =
[-40mm,0.0,0.005],D=8193m/s,P_CJ=28e9,
                        solid=_c4,gas=_jwlgas >
```

Creating a detonation model

In order to determine heat release from the solid to gas species decomposition, the correct heat of formation must be determined for each such that the resulting energy release is achieved when the detonation front passes a particular region.. Here we give an example of how to set up these parameters for the material C-4. The properties form the JWL EoS for C-4 are as follows: $\rho_0 = 1601 kg/m^3$, $D = 8193 m/s$, $P_{CJ} = 28\times10^9 Pa$, $E = 9\times10^9 J/m^3$, $A = 609.77\times10^9 Pa$, $B = 12.9\times10^9 Pa$, $R1 = 4.5$, $R2 = 1.4$, and $\omega = 0.25$. Note, the detonation velocity, D, and the Chapman-Jouguet pressure, P_{CJ}, are provided to the explosive burn input given in the `.vars` file as specified above. The gas species is covered by a JWL equation of state (note C_v must also be provided to obtain the correct specific heat of the expanded detonation products.) The example is repeated here:

```
// Explosive gases released under detonation of C-4
_jwlgas   = <m=45,n=3.3, href=0,sref=0.0,Tref=0,Pref=0,mf=0 > ;
_jwlgas: <eos=JWL(A=609.77e9,  B=12.95e9, omega=0.25,
R1=4.5,R2=1.4,
                    rho_0=1601,Cv=1e6)> ;
```

Note that in the above model, setting `href=0` and `Tref=0` ensures that the heat of formation for this species is identically zero. To describe the explosive burn, we must also specify the solid explosive material EoS. For this we utilize the elastic solid with $\rho_0 = 1601$, $K = 10\times10^9$, $P0 = 10^5$, $m = 1$, and $n = .18$. These parameters are set to approximate the properties of the solid explosive

material as an elastic solid. If we set `Tref=0` and `m=1`, then we can compute the value `href` to release E units of energy as given by the expression (note h_f is in the units of $J/kmol$ and m has the units $kg/kmol$):

$$h_f = m\frac{E - \left(1+\ln\left(\rho_0\right)\right)K - P_0}{\rho_0} - n\hat{R}T_0. \quad (3.19)$$

Assuming T_0=300 Kelvin we can then compute the reference enthalpy at absolute zero because the solid material can be computed as:

$$h_f = 1\frac{9\times10^9 - (1+\ln(1601))10\times10^9 - 10^5}{1601} - 0.18(8314.3)(300) = -47159739 \quad (3.20)$$

Thus, the solid C-4 material will be defined by the following specification:

```
_c4= <m=1,n=.18, href=-47159739, sref=0.0,Tref=0,Pref=0,mf=0 > ;
_c4: <eos=ElasticSolid(rho_0=1601,K=10e9,P0=1e5) > ;
```

3.5 Techniques to preserve positive mass fractions

When simulating multicomponent flows, it is possible to take a time-step such that the material in a cell is completely depleted, resulting in the time evolution of negative mass fractions of material. This non-physical circumstance is unacceptable because advancing the solution becomes nearly impossible. For first-order spatial approximations, depletion of the material from a cell is avoided if a time-step is employed that satisfies the stable CFL condition. However, when reconstructing higher-order mixture fractions, it is possible to deplete a material even when using a much smaller time-step To allow for second-order spatial reconstruction of species mass fractions, we first limit the mass fraction extrapolations so that a negative mass fraction will not occur (assuming a first-order upwind convection). While such limiting helps avoid the evolution of negative mass fractions, they can still evolve. Therefore, to provide an effective strategy that avoids negative mass fraction evolution in the time-stepping algorithm, we limit the stable time-step to include the time required to deplete a cell of all species material using the first time-step residual.. However, for multicomponent simulations, a CFL setting between 0.75 and 0.5 still may be required to avoid the evolution of negative mass fractions.

3.6 Validation studies

Hemispherical surface explosion

To test our JWL EoS and our explosive burn model, we compared the results of simulations of a rigid, surface-laid hemispherical charge of TNT with a radius of 144*mm* and a mass of 10.19*kg*, and we compared the blast strength and impulse with results provided in the Fiserova PhD dissertation [Fiserova, 2006]. The resulting blast wave parameters, namely overpressure and specific impulse, were examined at distances between 200*mm* and 700*mm* above the ground. JWL equation of state and perfect gas equation of state for modeling the explosive gas were both

evaluated. Two different cases using the JWL EoS were studied: one utilizing the prescribed explosive burn detonation model and the other utilizing a bursting high pressure sphere with initial pressure given by the equilibrium pressure of the volume-confined explosive gases. Our simulation findings were compared with empirical data obtained from CONWEP and simulation results from AUTODYN provided by Fiserova [Fiserova, 2006].

When the explosive burn model was used in this study, the TNT solid material was modeled as an elastic solid with a bulk modulus K=10GPa and density at ambient conditions of ρ_0=1630kg/m^3. The explosive gas was modeled using the JWL equation of state with A=371.2GPa, B=3.231GPa, ω=0.3, $R1$=4.15, and $R2$=0.95. Air was modeled as a perfect gas with a γ=1.4 and an average molecular weight of m=28.89. The explosive burn was initiated from the center of the sphere that formed the hemispherical charge with a detonation velocity of D=6900m/s and a Chapman-Jouguet pressure of P_{CJ}=21GPa.

Grid convergence was studied using 5mm, 3mm, 1mm, 0.75mm and 0.375mm cell sizes. Figures 3.1, 3.2 and 3.3 are time histories of the overpressure obtained from the JWL EoS with detonation model, the JWL EoS without detonation model, and the perfect gas EoS, respectively. The overpressure-time histories were recorded at distances between 200mm and 700mm above the ground at 100mm increments. For the models using the perfect gas EoS and the JWL EoS without detonation, it was observed that the cell size had little effect on the resulting blast wave parameters except at the closest distance above the ground. However, the results using the JWL EoS with the explosive burn model were shown to be more dependent upon the grid size. For cell sizes of 0.5mm and 0.375mm, the maximum over-pressures are convergent. For the finest grid size in JWL EoS with detonation, oscillations in the pressure after the initial shock are apparent in the results. Investigation of these oscillations showed that they were caused by apparent Richtmyer-Meshkov and Rayleigh-Taylor instabilities forming in the contact discontinuity between the explosive products and air as is shown in Figure 3.4. Some of these instabilities seem to have been seeded by irregularities created by the unstructured mesh used in the simulation. However, such turbulent mixing of the contact discontinuity is physical and expected based on high speed photographic recordings of the fireball in explosive events.

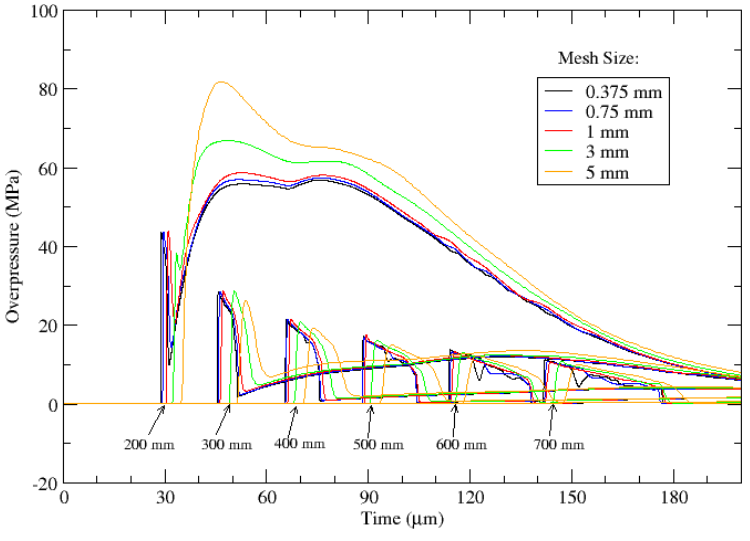

Figure 3.1: Time history of overpressure for TNT charge with explosive burn model using JWL EOS.

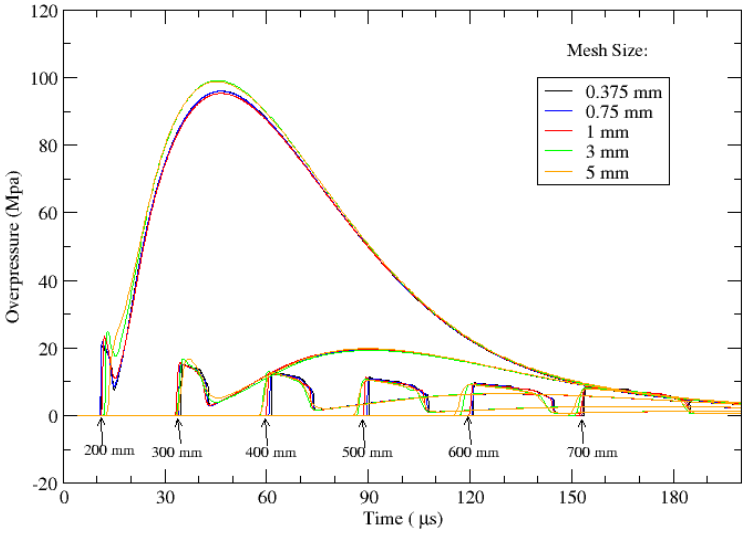

Figure 3.2: Time history of overpressure for TNT charge without explosive burn model using JWL EOS.

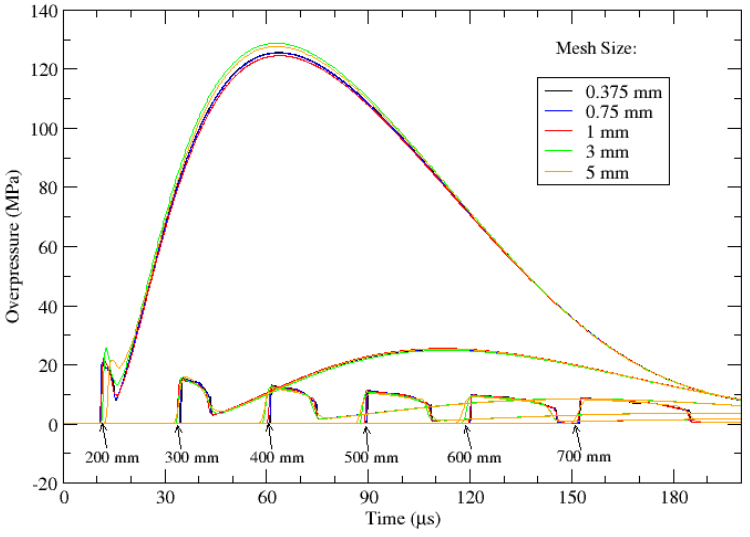

Figure 3.3: Time history of overpressure using perfect gas EOS.

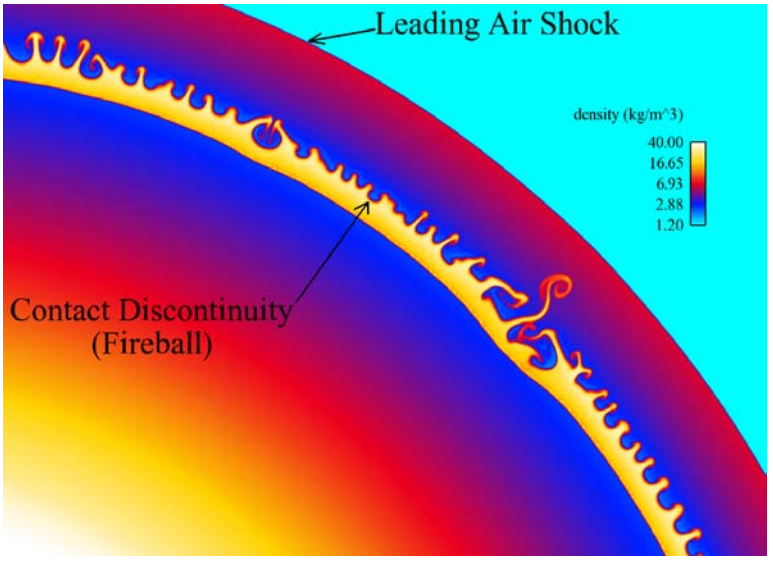

Figure 3.4: Simulated instabilities fireball on the 0.375*mm* mesh.

Blast wave parameters obtained from our simulation results were compared with empirical data from CONWEP and simulation findings from AUTODYN, as shown in Figs 3.5 and 3.6. For the perfect gas EoS and the JWL EoS without detonation model, results from the 1*mm* grid size were utilized. For the JWL EoS with detonation model, results from the 0.5*mm* grid size were used. For the purpose of fair comparisons, results from the 0.5*mm* grid size were chosen for the AUTODYN simulations. Figure 3.5 presents the maximum over-pressures at different distances above the ground. At the closest point above the ground (200*mm*), all the simulation results over-predict by at least 37.5 percent. However, it is noted that CONWEP is unable to provide data for distances below 300*mm* in this case; therefore, the blast parameters from CONWEP at distances below 300*mm* are evaluated by extrapolation. At distances above 300*mm*, the simulations provide reasonable results with the perfect gas EoS and the JWL EoS without detonation underestimating the maximum over-pressure, and the JWL EoS with detonation and the AUTODYN overestimating it. Figure 3.6 shows the specific impulse at different distances above the ground using different models. The specific impulse is defined as the time integration of the overpressure. Again, the simulation results from the models over-predict when compared with the CONWEP extrapolated data at the closest distance. At the farthest distances (larger than 500*mm*), the simulation findings appear to be lower than experimental data.

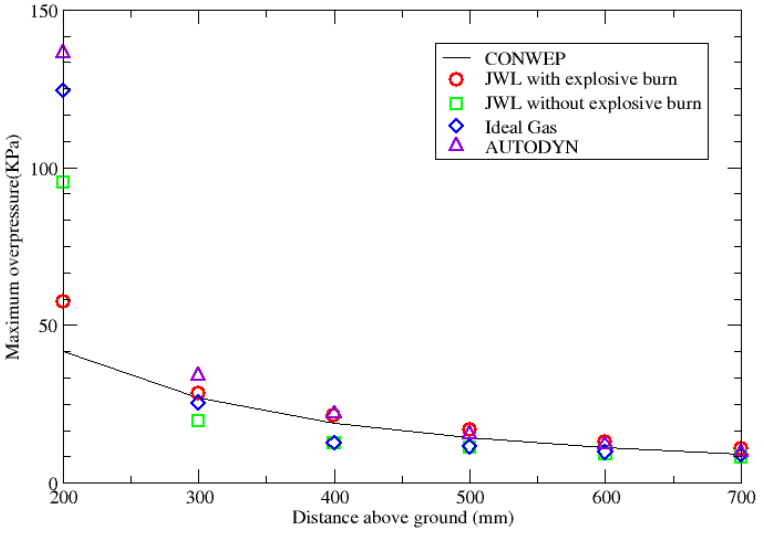

Figure 3.5: Comparison of maximum overpressure using different models.

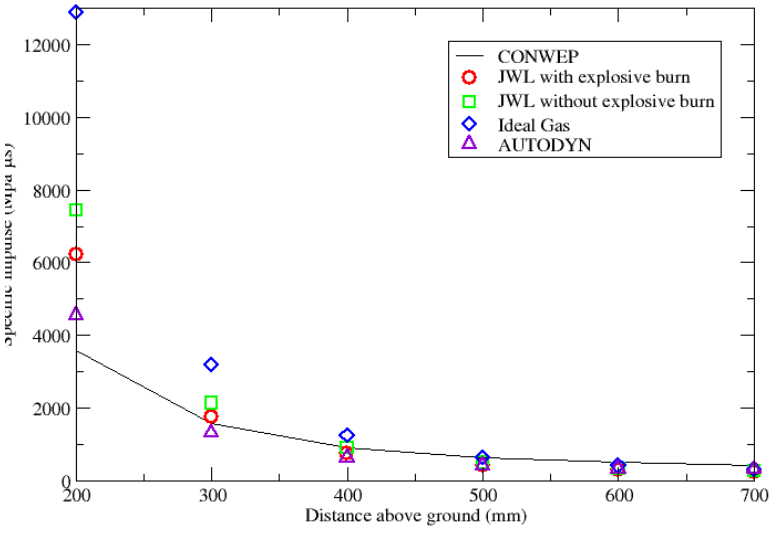

Figure 3.6: Comparison of specific impulse using different models.

Small-scale explosion in dry sand

The second validation study simulated the explosion of C-4 charges buried under dry sand. Three burial depths, were given in terms of the thickness of soil overlaying the mine: 0*mm* for flush burial, and 3*cm* or 8*cm* overburdens for buried landmines. Blast wave parameters were measured in the computations at stations located 30*cm* and 70*cm* above the ground. The explosive charge was defined by 100 grams of C-4 in a disk-shaped charge with a radius of 3.2*cm* and a thickness of 2*cm*. The explosive charge was initiated in the center. The solid, unexploded C-4 was modeled as an elastic solid with a bulk modulus of K=10*GPa* and a density at ambient conditions of ρ_0=1601kg/m^3. The explosive gasses were modeled using the JWL EoS with A=609.77*GPa*, B=12.95*GPa*, ω=0.25, $R1$=4.5, and $R2$=1.4. The explosive burn was modeled with a detonation velocity D=8193m/s and a Chapman-Jouguet pressure P_{CJ}=28*GPa*. Dry sand was modeled as a mixture of solid quartz and air, with solid quartz being modeled as an elastic

solid with a bulk modulus of K=33.77GPa and a density at ambient conditions of ρ_0=2650kg/m^3. The mixture contains .0311% air by mass. The resulting mixture density was the same at ambient conditions as the sand utilized in the experiment. Notably, in this simulation there were four species: air, quartz, jwlgas, and C4. Sand was created by mixing quartz and air in appropriate proportions. As the detonation front expanded, the C4 species converted to jwlgas.

Simulations of the buried charge were carried out on three grids, starting with one that had a mesh spacing of 1mm in the explosive charge, and then successively refining said grid to achieve 0.5mm and 0.25mm mesh spacings. Pressure probes were placed at 30cm and 70cm above the ground. At the time of reporting, only the flush cases had been run on all three meshes for a sufficient amount of time to determine the impulse at the 70mm probe. For the other depths of burial (DOB), the simulations should be run longer to get a complete grid convergence comparison. Results from the flush case and results from the 30cm probes on the other cases indicate that the 1mm mesh is satisfactorily converged. Comparison with experiments and other codes will therefore be given for the results of simulations on the 1mm mesh.

Results from the 1mm mesh for the mine that was buried flush with the ground for times 50μs, 100μs, 500μs, 1000μs, 1500μs, and 2000μs are given in Figures 3.7-3.12, respectively. These figures show an upward directed blast wave with significant compaction of the sand underburden in the early stages of the blast formation. As the explosive blast evolves, the crater forms an upward jet of exploding gases. These gases, which expand behind the leading shock wave, become unstable and mix in a turbulent fashion after t=500μs.

Results from the simulation on the 1mm mesh for the mine that was buried under 3cm of sand for time 50μs, 100μs, 500μs, 1000μs, 1500μs, and 2000μs are given in Figures 3.13-3.18, respectively. These figures show the compaction and deformation of the surface sand in response to the growing bubble of explosive gases. By t=1000μs the sand layer begins to become unstable and mix with the explosive gases, and by t=2000μs the sand interface breaks into disconnected regions, as can be observed in Figure 3.18.

Results from the simulation on the 1mm mesh for the mine that was buried under 8cm of sand for time 50μs, 100μs, 500μs, 1000μs, 1500μs, 2000μs, 3000μs, and 4000μs are given in Figures 3.19-3.26, respectively. At this DOB, the simulations show a significant bubble of explosive gases forming under the sand before eruption through the surface. By t=2000μs, instabilities in the outer sand layer are beginning to cause mixing between the sand and the expanding explosive gases. By t=4000μs, the explosive gases have broken through the sand layer and there is significant mixing evident in the fireball. All of these simulations are qualitatively similar to simulations documented by Fiserova [Fiserova, 2006], Wang [Wang 2001], and Grujicic [Grujicic et al., 2006].

We can show results on the 0.25mm spacing grid that illustrate some of the fine details captured in our simulations. Figure 3.27 shows the density plot from this high resolution simulation at 1400μs after detonation. Here we see that the overburden sand that is thrust in the air by the blast undergoes severe mixing, which suggests the presence of large instabilities. These instabilities appear to come from baroclinic torque caused by pressure disturbances moving through the thin, high-density region that forms from the soil overburden. In turn, these rapidly rotating regions produce some rather violent motion of the sand ejecta that results in regions of high and low pressure and which further enhance the unstable motion. These effects can be seen even more dramatically in the numerical Schlieren shown in Figure 3.28. We suspect that this is not physically real, as the sand should become a dispersed phase with momentum somewhat decoupled from the gas phase pressure; however, the current homogeneous multiphase mixture

does not permit this to occur. It is suggested that removing sand that has become sufficiently dispersed and placing it in a Lagrangian multiphase model would improve the physical realism of the model at this stage of the computations. However, given sufficient mesh resolution, it appears that the sand would naturally break into a dispersed material cloud due to the unstable mechanisms that we observe in these simulations.

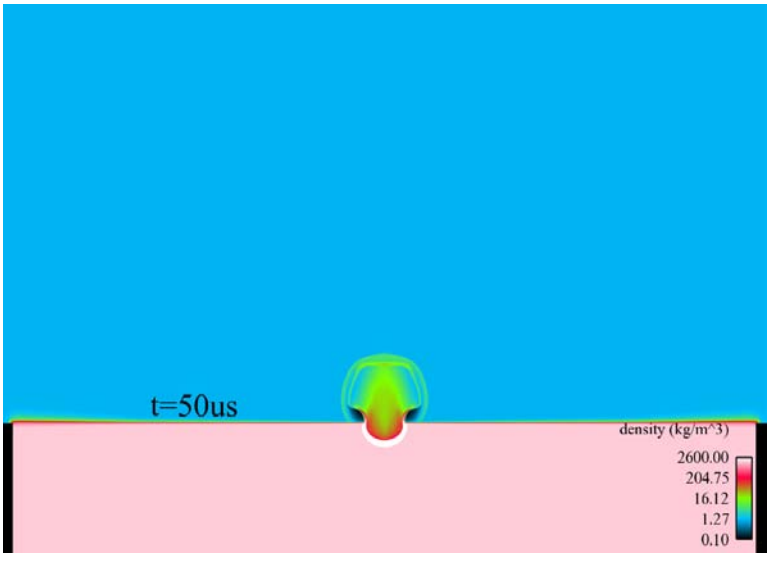

Figure 3.7: Density plot, DOB=0*cm*, t=50*μs*.

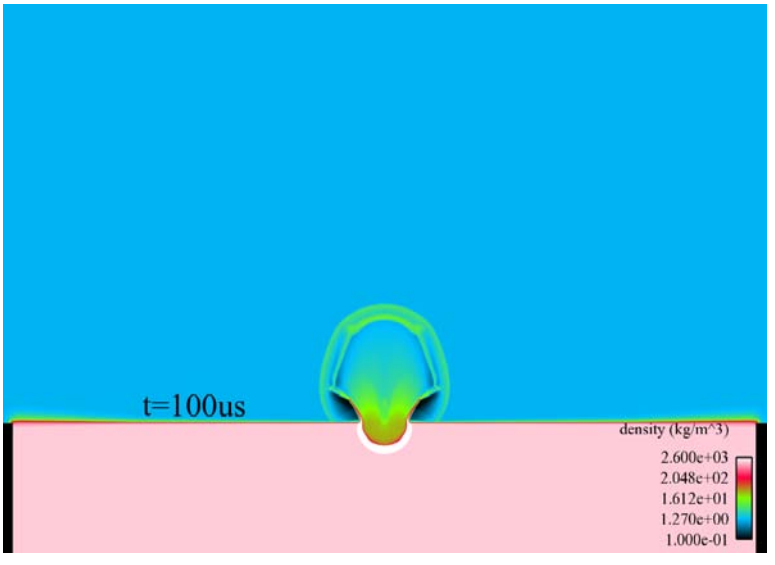

Figure 3.8: Density plot, DOB=0*cm*, t=100*μs*.

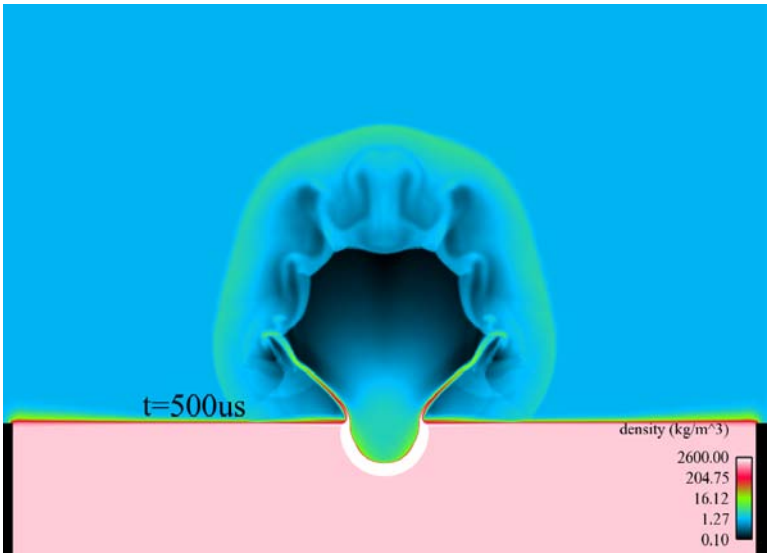

Figure 3.9: Density plot, DOB=0*cm*, t=500μ*s*.

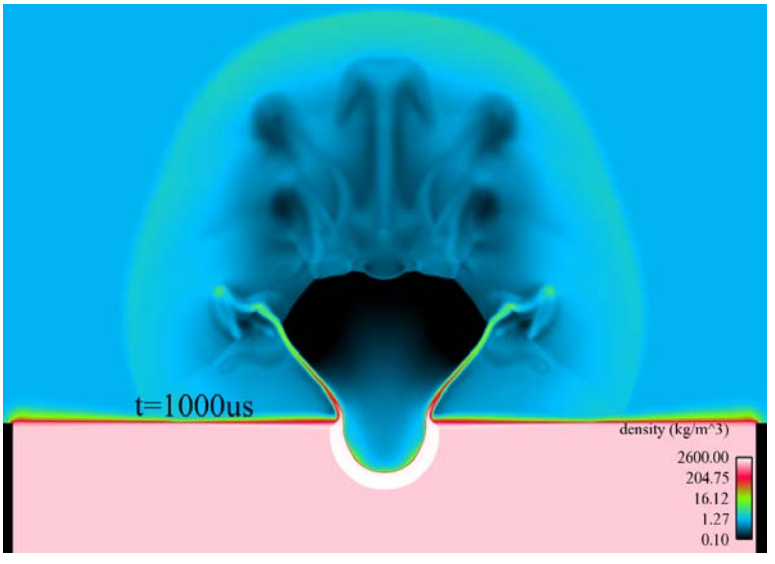

Figure 3.10: Density plot, DOB=0*cm*, t=1000μ*s*.

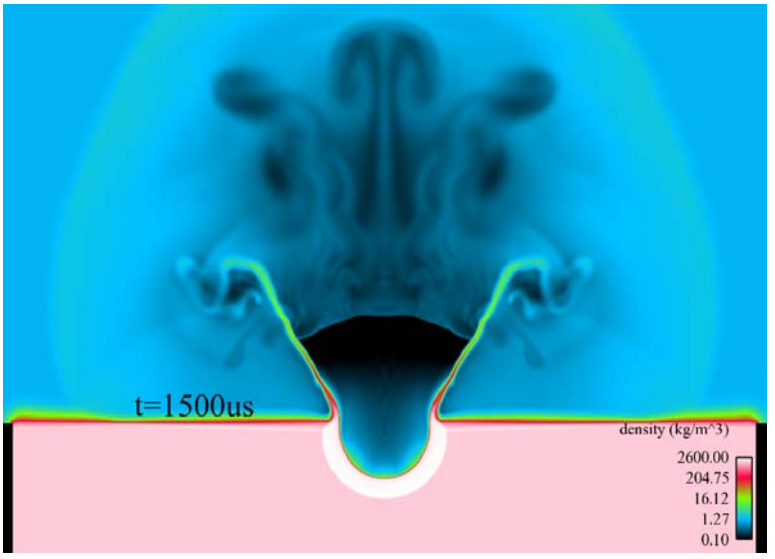

Figure 3.11: Density plot, DOB=0*cm*, t=1500μ*s*.

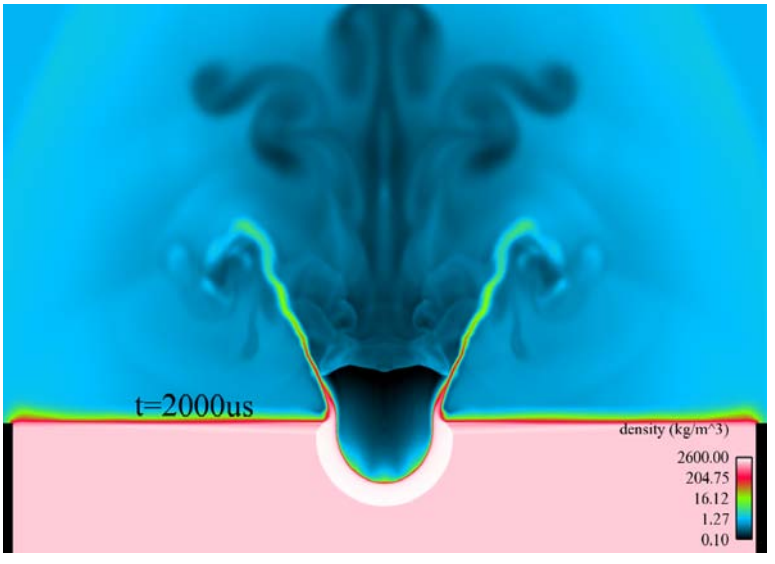

Figure 3.12: Density plot, DOB=0*cm*, t=2000μ*s*.

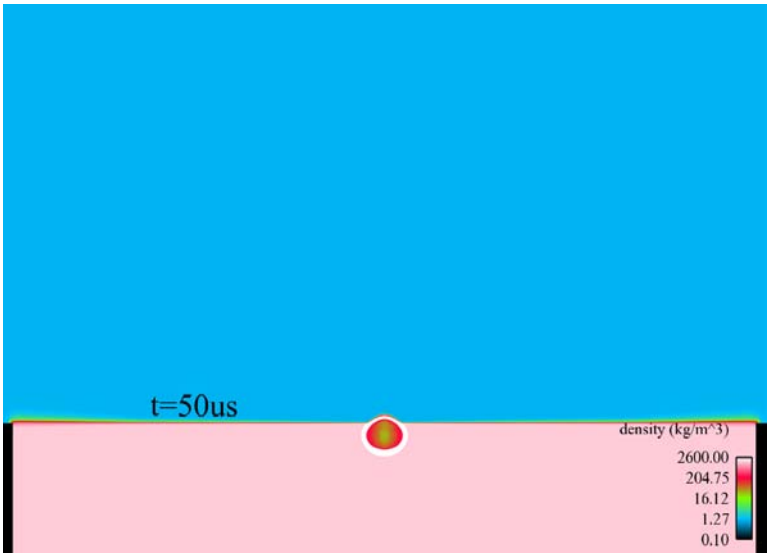

Figure 3.13: Density plot, DOB=3*cm*, t=50μ*s*.

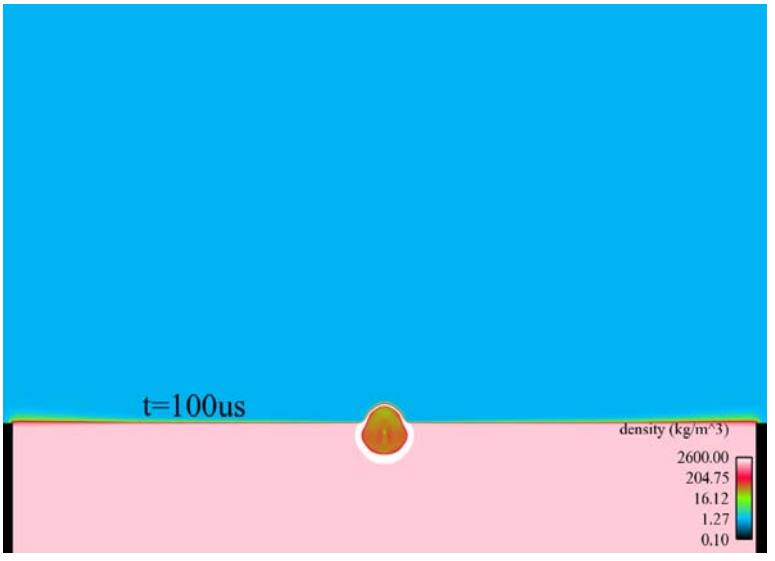

Figure 3.14: Density plot, DOB=3*cm*, t=100μ*s*.

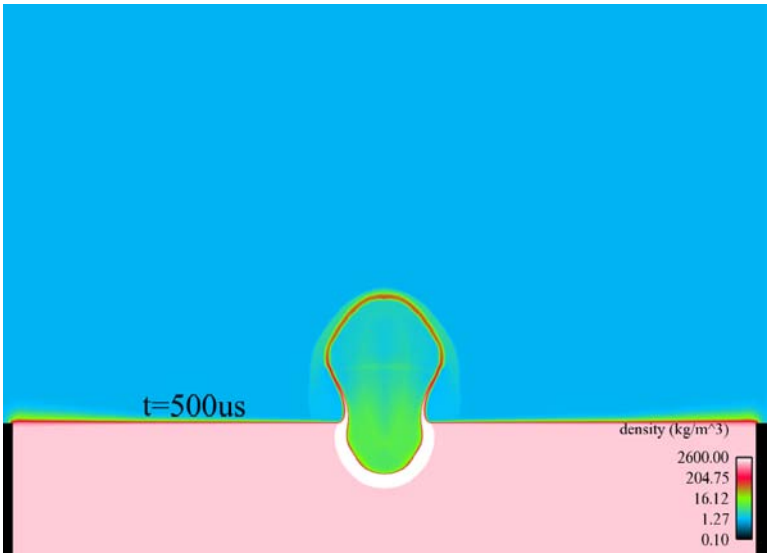

Figure 3.15: Density plot, DOB=3*cm*, t=500μs.

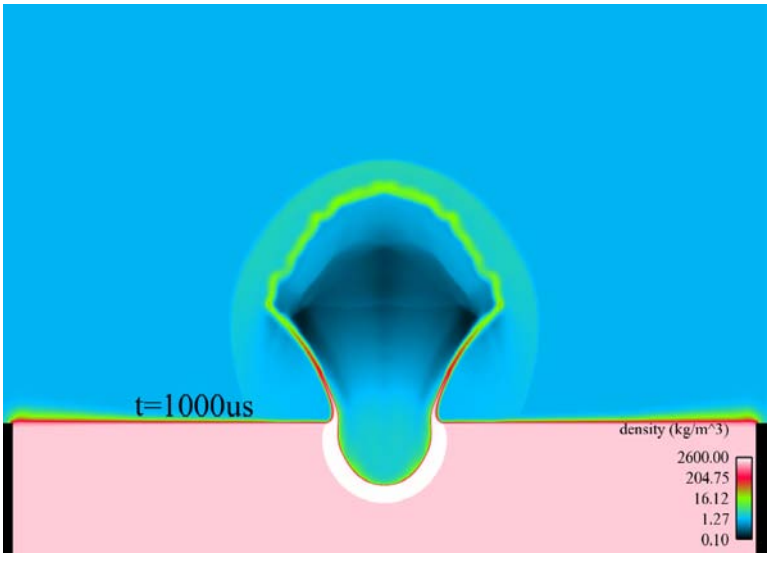

Figure 3.16: Density plot, DOB=3*cm*, t=1000μs.

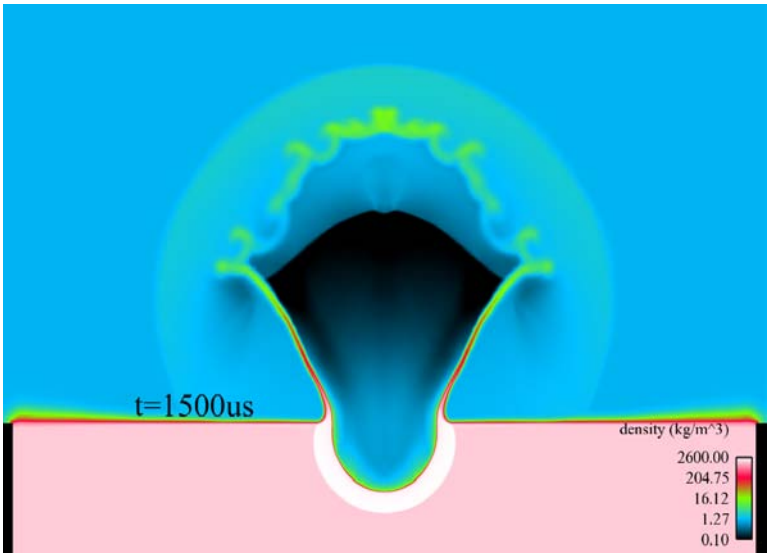

Figure 3.17: Density plot, DOB=3*cm*, t=1500μ*s*.

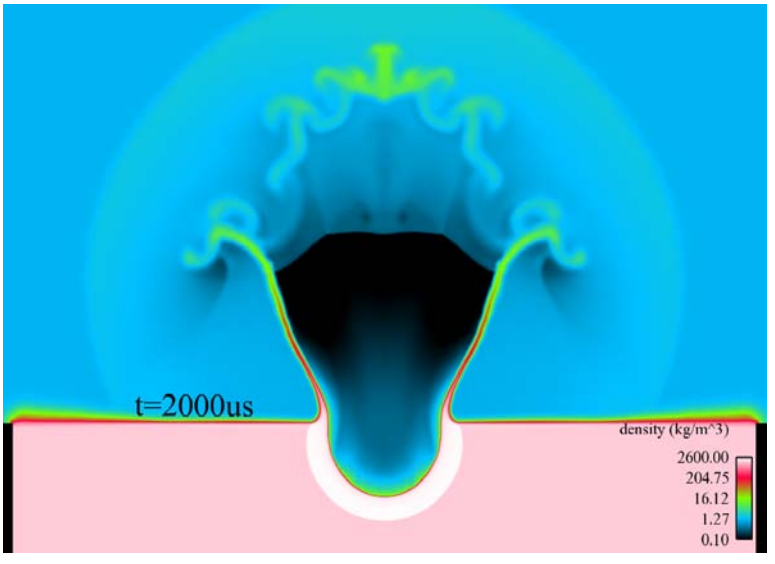

Figure 3.18: Density plot, DOB=3*cm*, t=2000μ*s*.

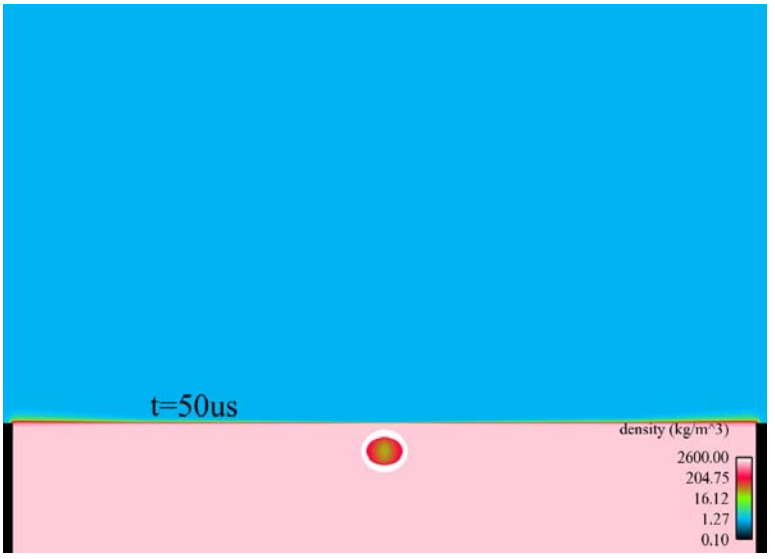

Figure 3.19: Density plot, DOB=8*cm*, t=50μ*s*.

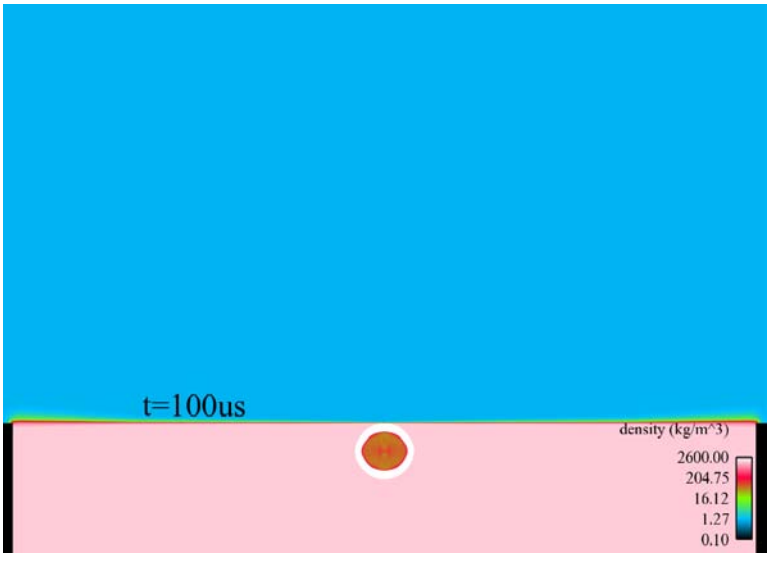

Figure 3.20: Density plot, DOB=8*cm*, t=100μ*s*.

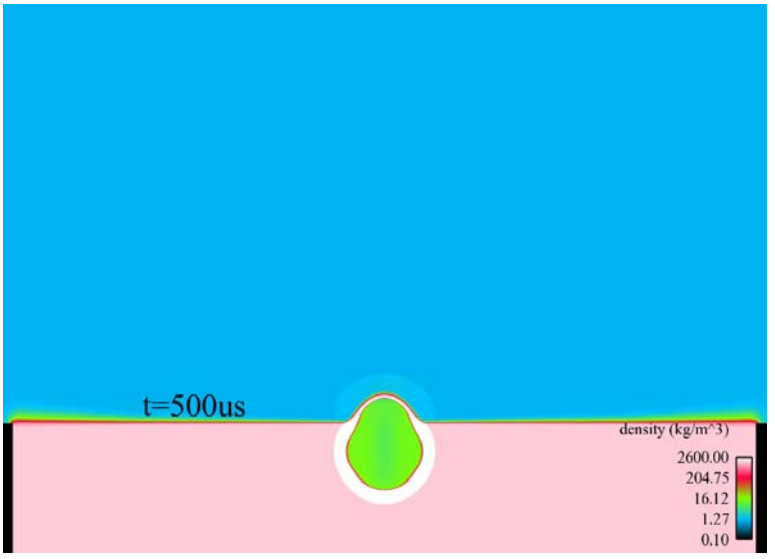

Figure 3.21: Density plot, DOB=8*cm*, t=500μ*s*.

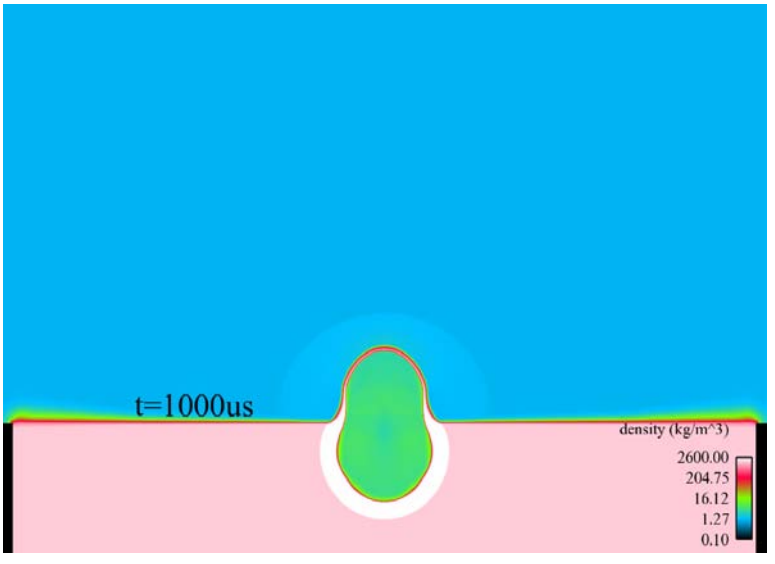

Figure 3.22: Density plot, DOB=8*cm*, t=1000μ*s*.

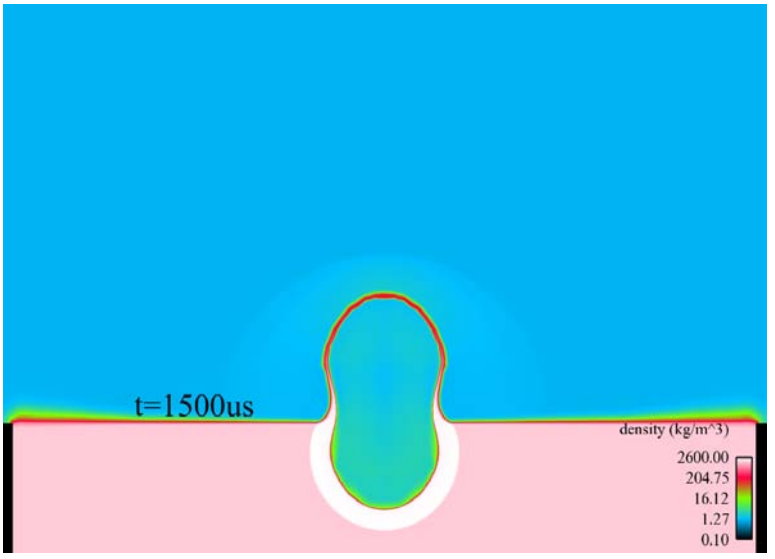

Figure 3.23: Density plot, DOB=8*cm*, t=1500μ*s*.

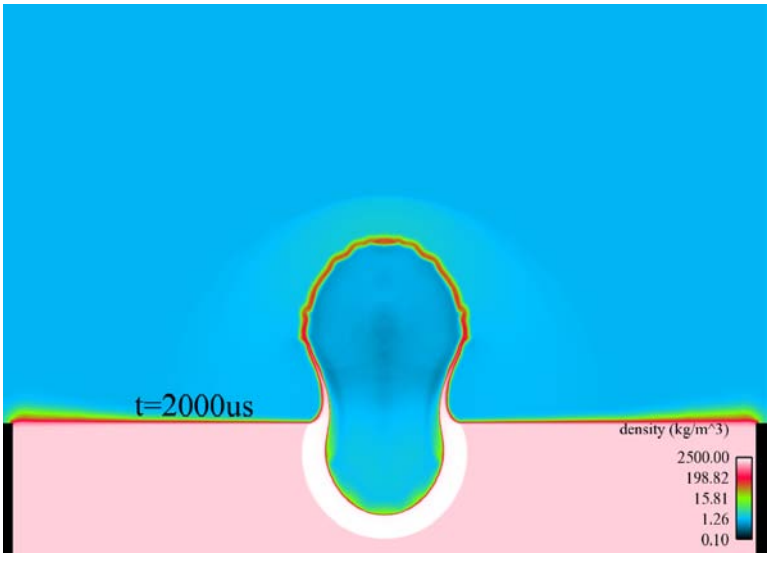

Figure 3.24: Density plot, DOB=8*cm*, t=2000μ*s*.

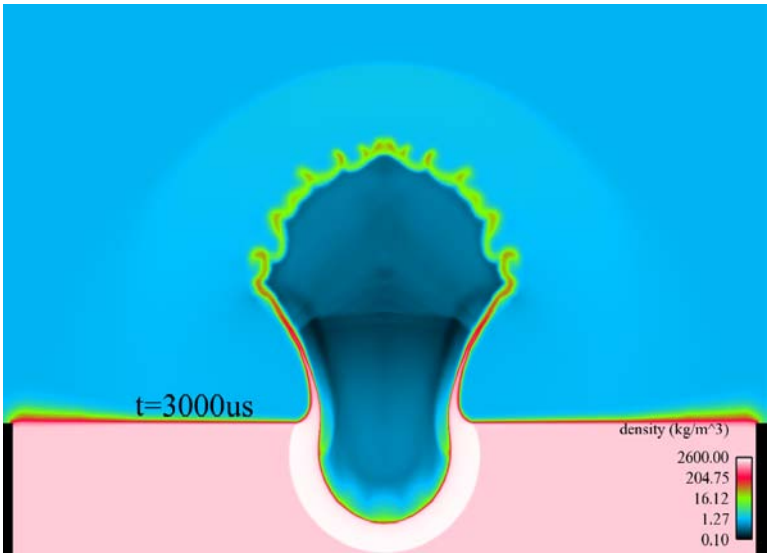

Figure 3.25: Density plot, DOB=8*cm*, t=3000μ*s*.

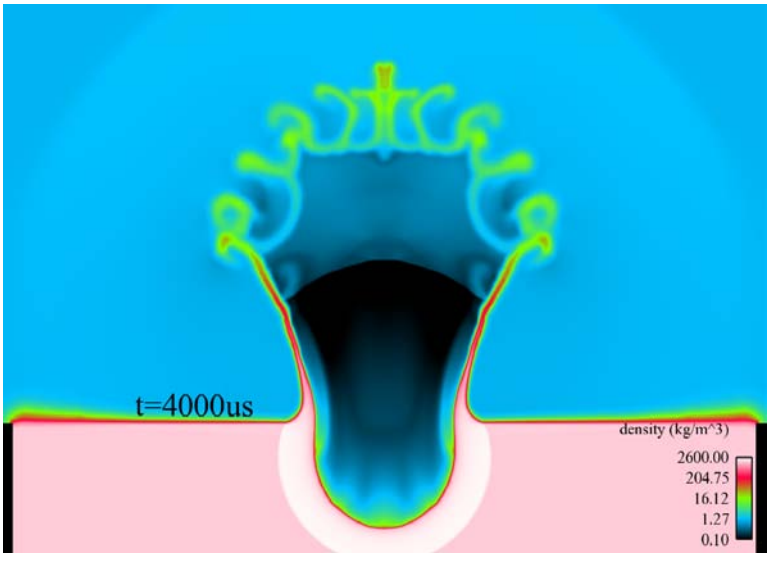

Figure 3.26: Density plot, DOB=8*cm*, t=4000μ*s*.

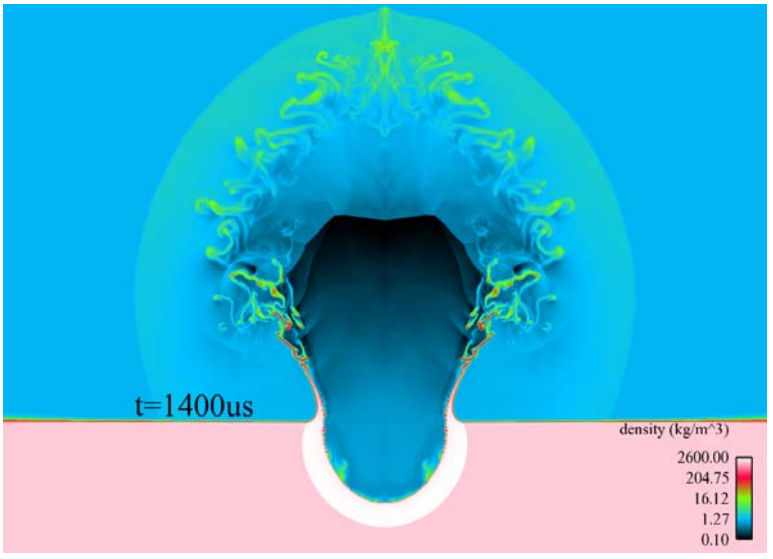

Figure 3.27: Density plot for dry sand, DOB=3*cm*, t=1400μ*s*, grid spacing=0.25*mm*.

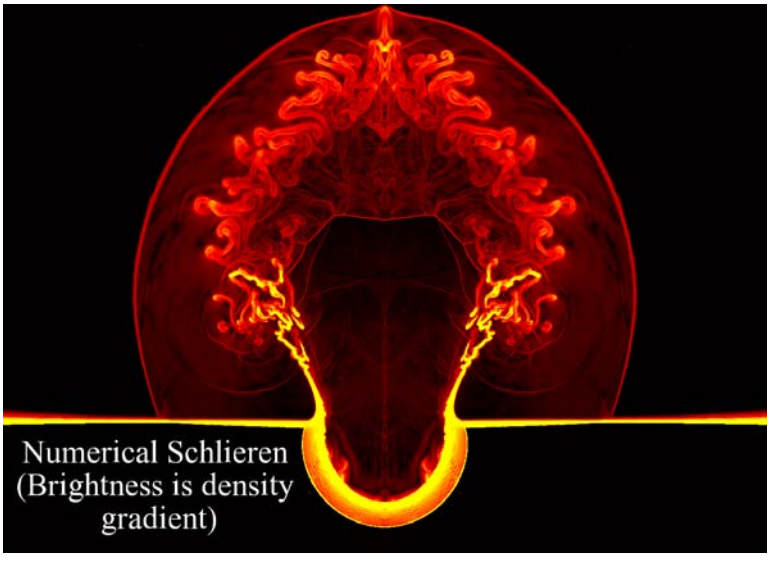

Figure 3.28: Numerical Schlieren, DOB=3*cm*, t=1400μ*s*, grid spacing=0.25*mm*.

In addition to these qualitative assessments, a case with saturated sand was also run. For saturated sand, the air volume was replaced with water, modeled using the Tait EoS; however, we included a very small fraction of air to allow for material expansion because the Tait EoS does not properly include cavitation effects. Thus, the saturated sand model consists of a quartz mass fraction of 0.77, a water mass fraction of 0.229995, and an air mass fraction of 5×10^{-6}. For comparison, the same buried mine simulation for a DOB of 3*cm* was run for both dry sand and saturated sand. The pressure plots for these simulations at t=500μs are given in Figures 3.29 and 30. Note in these figures, the white curve indicates the sand interface in order to make the location of the sand clear. For the dry sand in Figure 3.29, the shock moves slowly due to the low sound speed in dry sand. The detonation products are less focused in an upward direction than the saturated sand case shown in Figure 3.30. In the saturated sand case, a fast moving shock wave is evident in the sand, reflecting the fact that saturated sand has a much higher sound speed. In addition, the expanding detonation products are more focused in an upward direction than the dry sand case. Qualitatively, these results are very similar to the simulations performed by Grujicic [Grujicic et al., 2006].

For quantitative validations, the simulation results from the 1*mm* grid are compared with experimental data obtained by Bergeron et al. [Bergeron et al., 1998]. In addition, the AUTODYN results from Fiserova [Fiserova, 2006] and LS-DYNA results from Wang [Wang 2001] are shown for comparison. While a final grid convergence study was not fully complete at the time this report was generated, preliminary results indicate that the 1*mm* meshes were of sufficient resolution to accurately model the problem at hand. For the quantitative comparison, the following blast wave parameters were considered: time of arrival of the blast wave front, maximum overpressure, and specific impulse. The results from experiments and the simulations for flush 3*cm* DOB are presented in tables 3.1 through 3.6. For flush deployment, the simulations results were similar to the AUTODYN results and also in reasonable agreement with the experimental data in terms of impulse and arrival time. In terms of overpressure predictions, the simulations over-predicted by an amount similar to AUTODYN, particularly for the close probe located 30*cm* above the ground. For the 30*cm* DOB, the simulations again produced results similar to AUTODYN. The simulations matched the experimental results reasonably well in terms of all parameters: maximum overpressure, specific impulse, and arrival time.

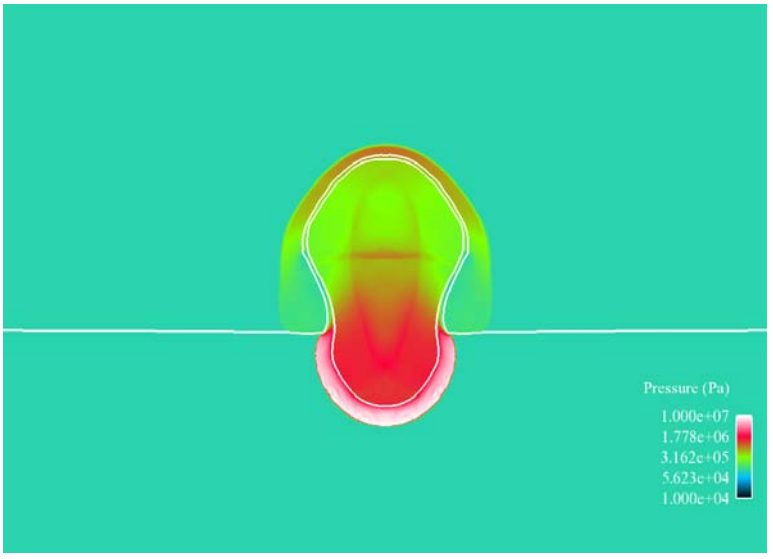

Figure 3.29: Pressure plot for dry sand, DOB=3*cm*, t=500μ*s*.

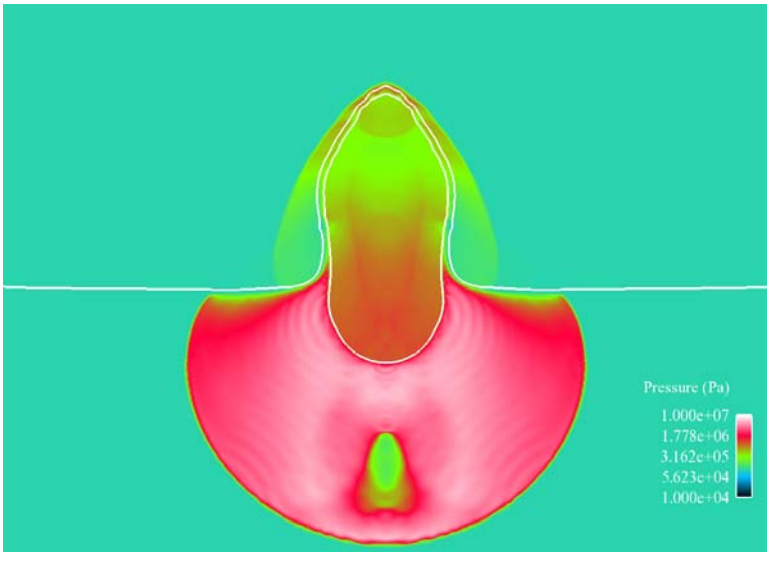

Figure 3.30: Pressure plot for saturated sand, DOB=3*cm*, t=500μ*s*.

Table 3.1: Comparison of maximum overpressure for flush deployment in dry sand for 100g C-4 charge.

Position above ground (mm)	flush, DOB=0 mm			
	Measured	Our results	AUTODYN	LS-DYNA
300	2797	8160	7380	1359
700	1189	1583	1409	580.8

Table 3.2: Comparison of specific impulse for flush deployment in dry sand for 100g C-4 charge.

Position above ground (mm)	Flush, DOB=0 mm			
	Measured	Our results	AUTODYN	LS-DYNA
300	85.8	98.0	98.0	86
700	116.4	177	169.6	137.5

Table 3.3: Comparison of arrival time for flush deployment in dry sand for 100g C-4 charge.

Position above ground (mm)	Flush, DOB=0 mm			
	Measured	Our results	AUTODYN	LS-DYNA
300	94.8	71.3	76	90
700	285.6	271.6	295	300

Table 3.4: Comparison of maximum overpressure for 3*cm* buried deployment in dry sand for 100g C-4 charge.

Position above ground (mm)	Buried, DOB=30 mm			
	Measured	Our results	AUTODYN	LS-DYNA
300	724.8	845	929.7	613.3
700	304.5	462.3	334.1	290.1

Table 3.5: Comparison of specific impulse for 3*cm* buried deployment in dry sand for 100g C-4 charge.

Position above ground (mm)	Buried, DOB=30 mm			
	Measured	Our results	AUTODYN	LS-DYNA
300	106.8	90.7	86.1	174.5
700	57.2	43.1	68.0	77.9

Table 3.6: Comparison of arrival time for 3*cm* buried deployment in dry sand for 100g C-4 charge.

Position above ground (mm)	Buried, DOB=30 mm			
	Measured	Our results	AUTODYN	LS-DYNA
300	266	356	318	270
700	784	804	740	710

Figures 3.31-3.37 show comparisons of displacement parameters between our simulation results and the experimental data obtained by Bergeron et al. [Bergeron et al., 1998]. In addition, the AUTODYN results from Fiserova [Fiserova, 2006] and LS-DYNA results from Wang [Wang 2001] are shown for comparison. The explosive charge is 100*g* C-4 buried under dry sand. The availability of experimental data to compare dictated running two DOB cases, namely *DOB*=30*mm* and *DOB*=0*mm*. From the grid convergence study run with 1*mm*, 0.5*mm* and 0.25*mm* grid sizes, we found that grid convergence is reached with 0.5*mm* grid size. Therefore, the results from the 0.5*mm* grid size were utilized in all comparisons. Vertical displacement of the soil, which is measured as the distance between the ground and the ejecta front, is plotted in Figure 3.31. Predictions from our simulations agree well with the experimental data. Figure 3.32 shows the temporal variation in the crater diameter. Fairly good agreement is achieved between the simulation and the measurement. At later times, our simulations over-predict the crater diameter by approximately 30 percent. It is likely that at later times, the lack of a soil strength model is responsible for this discrepancy; specifically, the strain rates diminish, which increases the relative importance of the material strength in the material kinematics. Figures 3.33 and 3.34 show the height and width of the detonation products cloud, respectively. The agreement between simulation results and experimental data is very good in both cases. We note that at longer times, our model under-predicts values relative to the experimental data. We suspect that this may be due to a lack of a failure mechanism for the soil. In our simulations, the soil encloses the growing cloud of detonation products, whereas in the AUTODYN simulations the soil ruptures thereby releasing the explosive products. In our method, the soil remains in velocity equilibrium with the explosive gases. Rather than failure, we propose that the soil should transition into a multiphase cloud and allow the solid soil material to take on independent velocity groups from the gas phase. We are now extending our model to include a multiphase modeling capability where, instead of failure removing material, failure would inject multiphase particles into the simulation. Such a model would allow for decoupling between the soil particles and gas velocities, thereby presumably creating a more rapid growth of the detonation cloud.

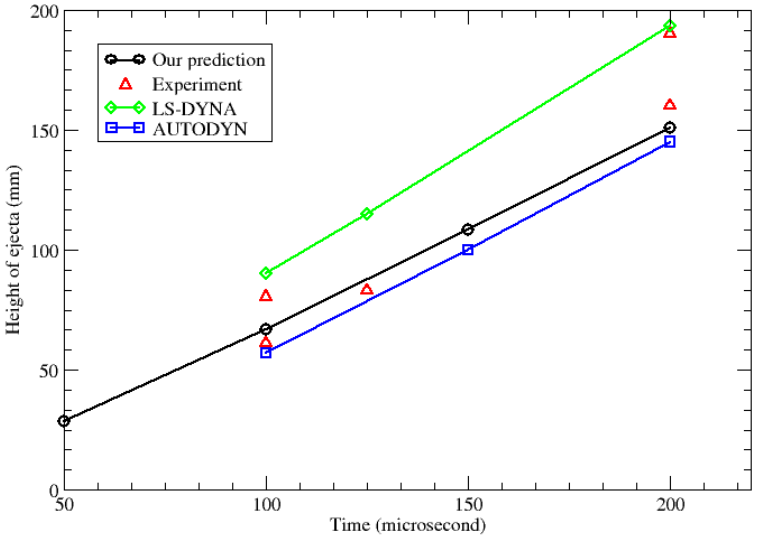

Figure 3.31: Time history of the height of ejecta at DOB=30mm.

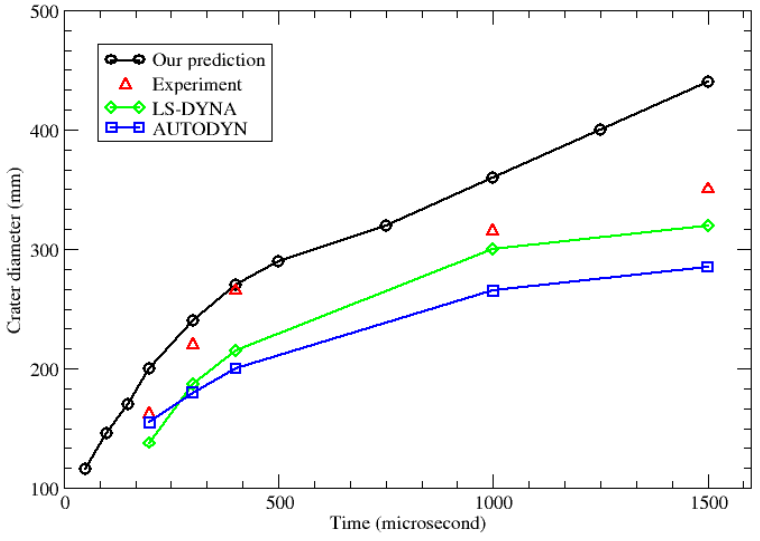

Figure 3.32: Time history of the width of crater at DOB=30mm.

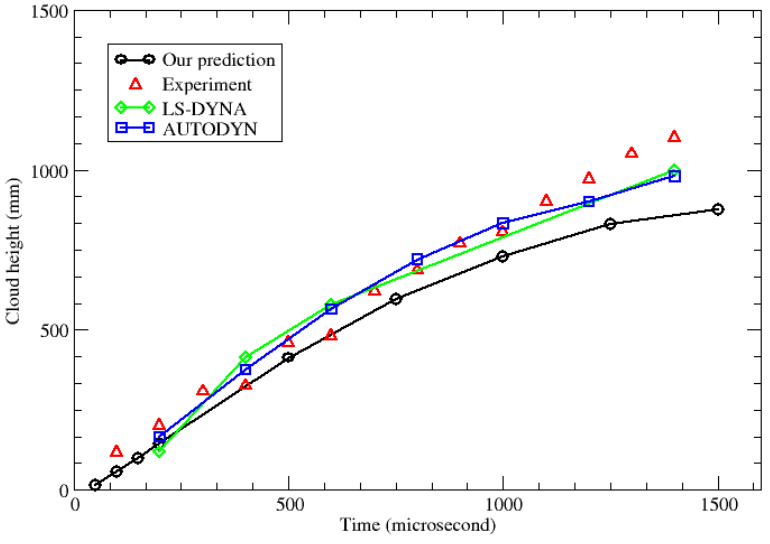

Figure 3.33: Time history of the height of the detonation product at DOB=30mm.

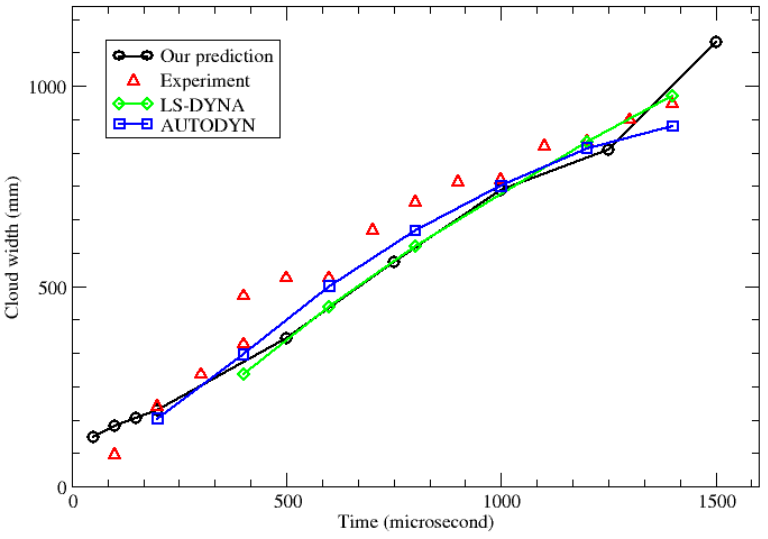

Figure 3.34: Time history of the width of the detonation product at DOB=30mm.

Figures 3.35-3.37 show the results for the case of zero DOB (the top of the mine is at ground level). Figure 3.35 shows the crater diameter, which agrees with experimental results very well. Figure 3.36 and 3.37 show the height and width of the detonation products cloud, respectively. The trends of our simulation agree with those from the experiment. We note that in the case of a flush buried mine, there would be little sensitivity to failure because there is no soil covering the mine to rupture. In addition, the crater formation will be mostly dominated by soil compression rather than shear, so we would expect little sensitivity in these results to material strength. In addition, since our algorithms employ numerical methods that conserve total energy (including material kinetic energy), we will capture the gas dynamics very well, even on a reasonably coarse mesh. Thus, in many ways the flush case is optimal for a simulation using numerical methods that are optimized for gas dynamics such as those employed in our models.

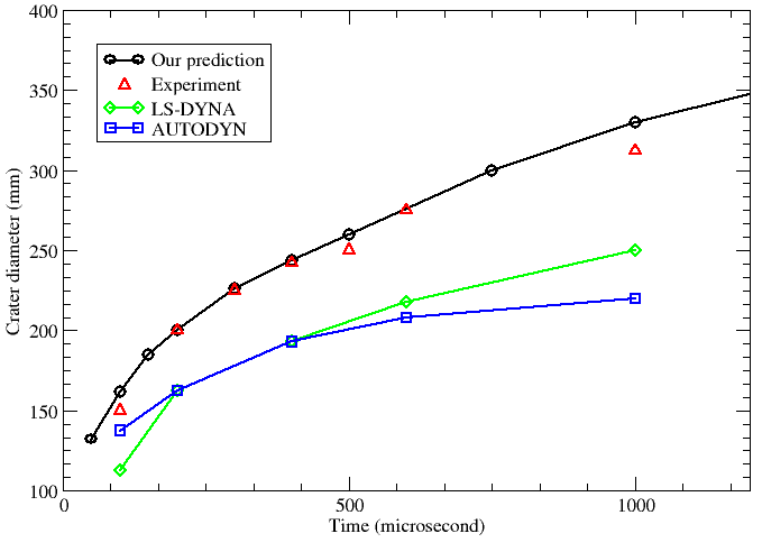

Figure 3.35: Time history of the width of crater at DOB=0mm.

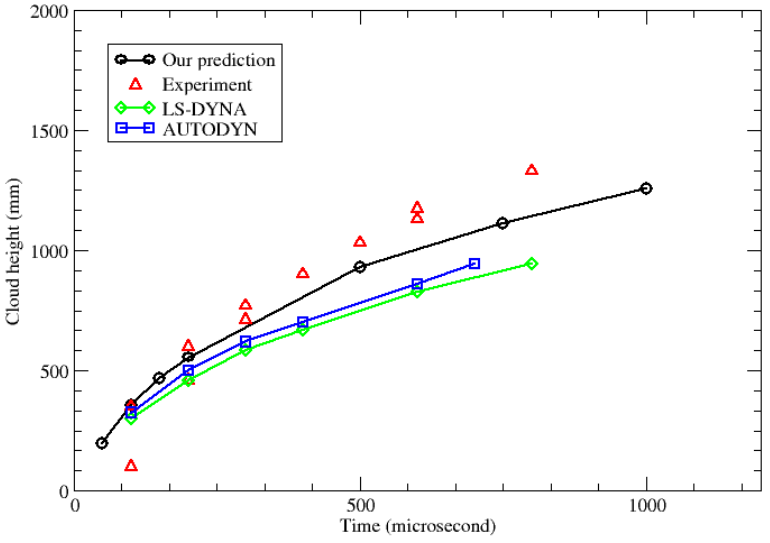

Figure 3.36: Time history of the height of the detonation product at DOB=0mm.

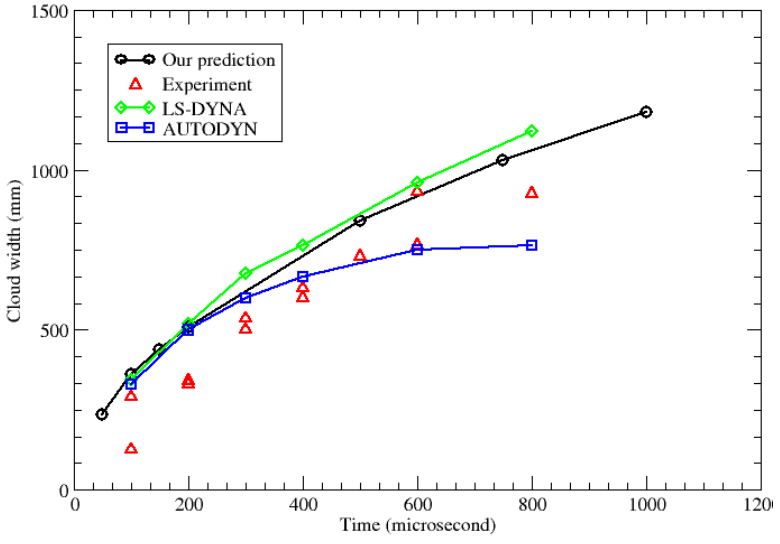

Figure 3.37: Time history of the width of the detonation product at DOB=0mm.

Mine impulse pendulum (MIP) explosion in prairie soil

The mine impulse pendulum is a horizontal ballistic pendulum that measures the effective impulse from a landmine explosion. The experiment was performed using DRDC Suffield's small pendulum apparatus [Coffey et al., 1998]. The pendulum consists of a target plate attached to two rotating steel beams affixed to a stationary base. The pendulum target plate is suspended at a specific standoff distance over a buried landmine. The landmine is detonated; maximum angle of inclination obtained by the pendulum arm is measured; and effective mechanical impulse applied to the target by the landmine can be derived as a function of the maximum inclination angle of the pendulum. Details describing the MIP experiment can be found in the PhD dissertation of Fiserova [Fiserova, 2006].

In our simulation, an axisymmetric plate is used to represent the square witness plate in the experimental setup. The axisymmetric disk has the surface area and moment of inertia equivalent to those of the square target plate in the experiment. The dimension of the disk is 1376*mm* in diameter and 68.76*mm* in height, with standoff distance of 400*mm* above the ground. An explosive charge of 1*Kg* C-4 is buried with one of two overburdens (*DOB*=100*mm*, 50*mm*). The diameter and thickness of the explosive charge are 134*mm* and 45*mm*, respectively. The soil properties of the trials used for validations in this section are shown in Table 3.7. The density values for air, water and solid in the soil are 1.2kg/m^3, 1000kg/m^3 and 2650kg/m^3, respectively. The value of dry density of the soil is set to 1322 kg/m^3 for all the trials in our simulations. Using the wet and dry density values, the mass fractions of the three phases (air, water, solid) composing the soil can be determined, which are shown in Table 3.8, where mf_s, mf_w, and mf_a represent the mass fraction of solid, water and air in the soil, respectively. The water content percentage was determined experimentally by measuring the mass of the soil and then drying the soil and measuring the mass of the dry soil. The moisture content is then defined as

$$w = \frac{\left(m_{wet} - m_{dry}\right)}{m_{dry}}. \tag{3.21}$$

The mass fractions computed in Table 3.8 were derived by assuming that the void volume is conserved and that the dry density and wet density can be written as

$$\rho_{dry} = \frac{\rho_{solid} V_{solid} + \rho_{air} V_{air}}{V_{solid} + V_{air}}, \rho_{wet} = \frac{\rho_{solid} V_{solid} + \rho_{water} V_{water} + \rho_{air} V_{air}}{V_{solid} + V_{water} + V_{air}}. \tag{3.22}$$

The mass fractions were then derived by considering (while neglecting the air contributions) that $\rho_{wet} = \rho_{dry}(1+w)$. Combining these equations and selecting an arbitrary reference for V_{solid}, the remaining volume fractions were computed by assuming that the pore volume is conserved: $\left[V_{air}\right]_{dry} = \left[V_{water} + V_{air}\right]_{wet}$. From these volumes, component mass fractions were computed.

For the present simulation, the solids were given the material properties of quartz. Since this type of soil contains sand and clay particles, this assumption is questionable. However, based on presently available data, the material properties of isolated clay (without the voids and water) are unknown. The explosive gas was described by the JWL equation of state, and the air was assumed to be an ideal gas. Impulse exerted on the target plate was computed and compared with the experimental data.

Table 3.7: Soil properties for simulated trials.

Moisture Content (%)	Wet density (kg/m^3)
6	1401
7.7	1423
12.2	1483
15.0	1520
18.2	1562
20.9	1598
23.7	1635
28.7	1704

Table 3.8: Calculated mass fraction for simulated trials.

Moisture content (%)	mf_s	mf_w	mf_a
6	0.9432598	0.05669	0.0003789
7.7	0.928165	0.0715867	0.0003304
12.2	0.891089082	0.108892255	0.000268851349
15.0	0.8694	0.130628	0.00023305
18.2	0.845755041	0.154181466	0.000194178589
20.9	0.826996	0.173127	0.0001630328
23.7	0.80804956	0.191823766	0.0001321024
28.7	0.7768	0.2233	8.0307298e-05

Figure 3.38 shows a comparison of impulse on the target plate versus soil moisture content for a 50*mm* overburden landmine explosion. Simulation results from AUTODYN and Martec's Chinook code [Martin and Link, 2003] are also included for comparison purposes. We note that the formulation of the Chinook code, which is similar to our methodology, employs algorithms typically used to solve inviscid gas dynamics equations. The figure demonstrates that the trends of increasing impulse as a function of moisture content are reproduced and qualitatively consistent with the experimental data. However, our simulations over-predict the impulse by 5 to 50 percent in comparison with the experimental data. Results from AUTODYN are smaller in magnitude than our predictions and, in general, show good agreement with the experimental data. Similar observations can be made for the 100*mm* overburden case, as depicted in Figure 3.39.

The over-prediction of the impulse for our present model is not unexpected, as we will explain shortly. To understand the details of this prediction, we studied the evolution of the plate loading for the 18.2% moisture content and 50*mm* overburden case. Figure 3.40 shows the integrated momentum flux on the plate as a function of time. We note that there are three spikes in momentum transfer: the first at t=0.5*ms*, the second at t=0.9*ms*, and the third at t=1.7*ms*. Between t=0.5*ms* and t=0.9*ms*, soil impacts over an increasingly large area, combined with a reduced momentum transfer in the center of the plate due to a soil rebound effect. By t=0.9*ms*, as illustrated in Figure 3.41, the explosive gases are enclosed by the soil. The soil velocity at this time is primarily in the direction normal to the plate. The dip in the momentum transfer observed at t=1.2*ms* is due to the rebound of the soil that struck the plate at t=0.9*ms*, while the final peak at t=1.7*ms* is caused by an increasingly glancing blow of the soil and gas material with the target plate, as can be seen in Figure 3.42. Also noteworthy is the presence of a thin region of dense, high-pressure soil material in the region immediately adjacent to the witness plate throughout the duration of peak momentum transfer to the plate. Although in the present model we cannot distinguish between the contributions to the loading due to the soil and the gases, the simulations support that a significant proportion of the loading is, in fact, due to the large density (and consequently large momentum) of the soil material. That our model is a homogeneous mixture of quartz, air, and water implies that the soil must have the same velocity as the gas phase. As a result, the model transfers too much momentum to the soil. A better model for this case would allow the soil to become a multiphase cloud of particles at an appropriate time. Once the soil particles are free to have their own velocity, the momentum coupling will become less efficient. Therefore, there will be less momentum in the soil that strikes the plate, reducing the overall impulse.

We also note that Martec's Chinook code, which makes the same homogeneous mixture assumption, also over-predicts the plate loading, Meanwhile, the AUTODYN model addresses the problem of the soil becoming a multiphase cloud in a different way: the soil material fails and is removed from the simulation allowing the gas to escape. The result is that the soil material will have a reduced momentum due to the failure mechanism. We note that failure may occur due to a dropping pressure, but also cells may be removed simply due to mesh tangling. In this case, there is no physical justification for the failure mechanism and the results are likely to be highly dependent on the initial mesh configuration. We also note that AUTODYN has an option to allow the mass of the free nodes to be included in the momentum transfer to the plate. In this case, a disembodied node created through material failure travels on a linear trajectory until it strikes a surface and is not treated as a multiphase particle with associated drag functions. We could not verify whether this mode was employed in the AUTODYN simulations that are included in our comparisons.

Furthermore, there is some uncertainty in how to define the material properties of the solids that are in the sandy clay soil. The prairie soil composition used in the MIP experiment consisted of a composition of 40-60% sand and 10%-20% clay. The exact elastic modulus of the clay particles are not known to the investigators at this time, and may have some influence on the impulse loading on the plate. In the Martec report [Martin and Link, 2003], the Chinook code was used to study this sensitivity where they reduced the solid material elastic modulus by a factor of 1000. The code obtained good agreement with this value. However, in our view, it is unlikely that the clay would cause such a significant change in the elastic modulus of the solids, and so the result would seem to suggest that the impulse loading would be rather insensitive to a small change (e.g. less than an order of magnitude) in the material stiffness.

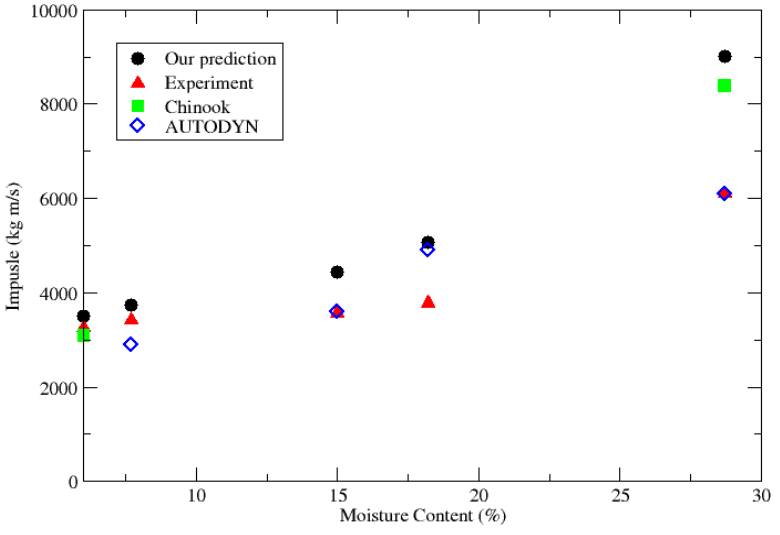

Figure 3.38: Comparison of impulse on the target plate for *DOB*=50*mm*.

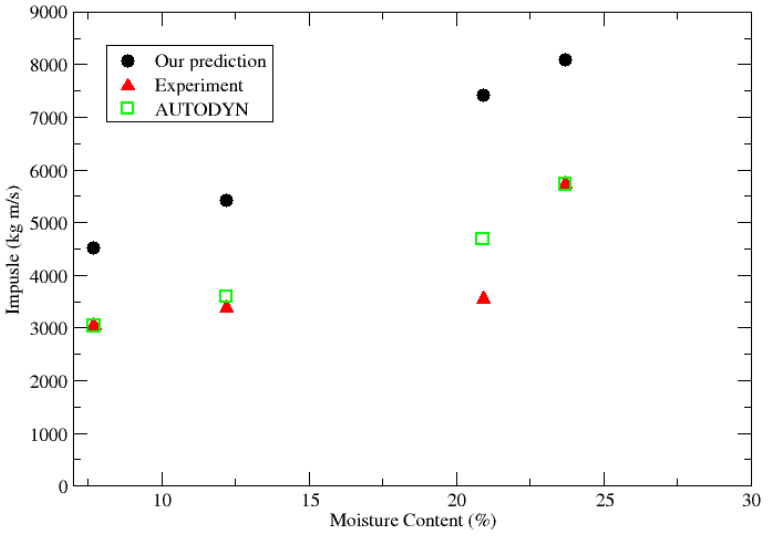

Figure 3.39: Comparison of impulse on the target plate for *DOB*=100*mm*.

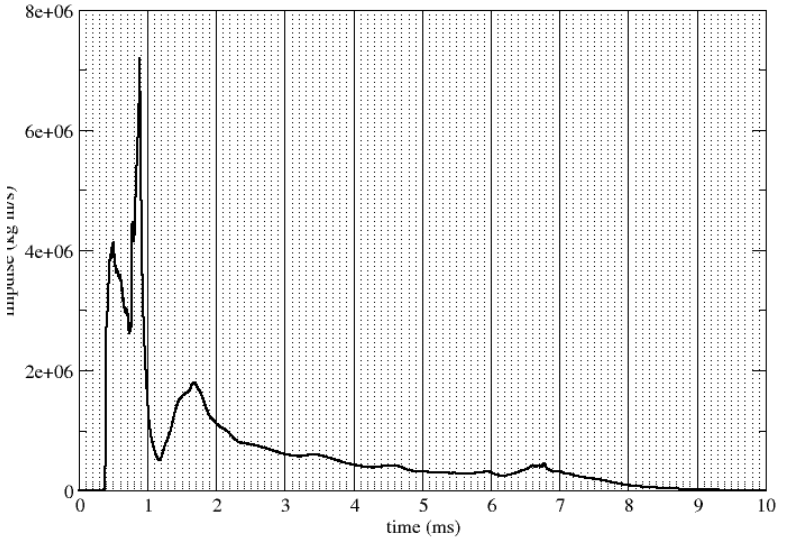

Figure 3.40: Time development of impulse of landmine explosion impacted onto a plate for *DOB*=50*mm* and 18.2% moisture content.

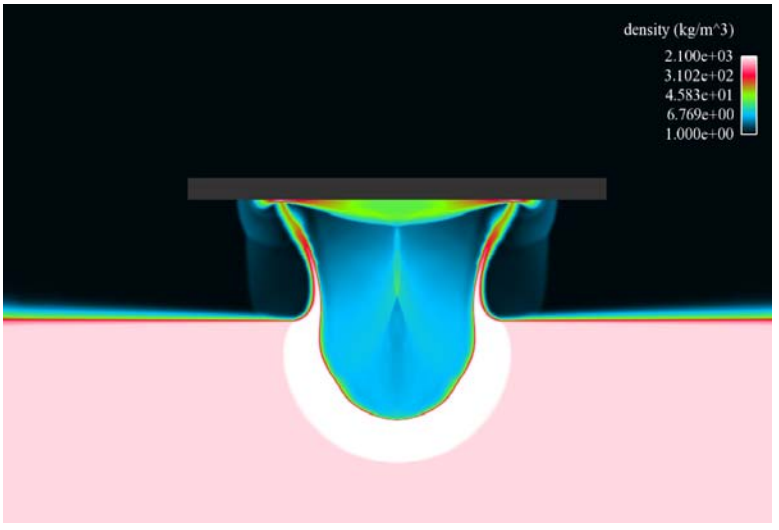

Figure 3.41: Density contour of landmine explosion impacted onto a plate for *DOB*=50*mm* and 18.2% moisture content at *t*=900μ*s.*

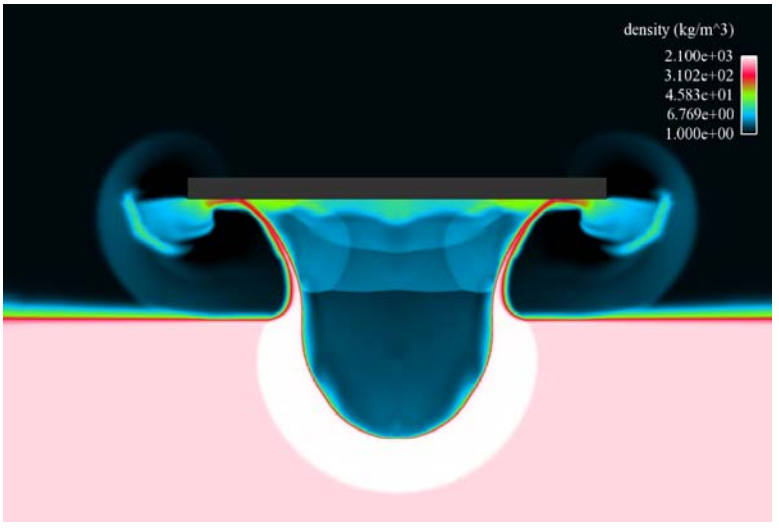

Figure 3.42: Density contour of landmine explosion impacted onto a plate for *DOB*=50*mm* and 18.2% moisture content at *t*=1700μ*s.*

3.7 Observations for further investigation

From the small-scale dry sand validation of the crater and ejecta cloud evolution, we have some evidence that material strength may play an important role in the later times of the soil-blast progression. The algorithms that we currently employ have been developed primarily for accurate gas-dynamics simulation; therefore including strength presents additional challenges. Specifically, in the current model, we track material velocity rather than material deformation, while strain is not directly available. However, development of strength models in the context of a Godunov type solver similar to the algorithm employed here have been developed [Miller and Colella, 2001] and could be adapted to our model with modest effort.

Probably the most critical feature that is lacking in our simulation is a more correct modeling of the transition to multiphase flow of soil during the explosive interaction. In the next quarter we plan to implement and evaluate the effects of coupling our present model with a Lagrangian particle tracking model. Transition to multiphase would occur based on criterions similar to failure, e.g. if soil material pressure (or density) dropped below a given threshold, we can assume that the soil decohesion results in a dense multiphase cloud. We expect that inclusion of these effects will improve our model performance on the MIP validation case.

Section 4: Simulation of blast interactions with debris

In this section, we investigate the effects of blast interactions with debris. One of the primary objectives of this effort was to characterize the effects of these interactions in order to develop appropriate phenomenological models to couple a multiphase model of soil particulates with the blast event. For this investigation, we limited our study to the blast effects on spherical quartz particles in different configurations in order to determine the effects of particle configuration on the loads that are communicated to the particles. We performed these simulations using an the implicit time integrator in Loci/CHEM which supports over-set meshes and independent movement of bodies subject to a six degree of freedom (6DOF) rigid body motion. We first performed a validation study for an isolated sphere subject to an impinging shock for which experimental data is available. We used this data to validate the over-set methodology and also to identify the mesh spacing that will be required to obtain a reasonable resolution of particle loads. We employed simulations of an isolated sphere subjected to a strong shock at various Reynolds numbers to determine the basic requirements of the simulation. We then considered 6DOF models for various particle configurations including tandem particle arrangements with different particle spacings as well as staggered configurations. Finally, we performed a 6DOF simulation on a collection of particles that interact with a spherical blast wave in place of the planar shock.

4.1 Shock-sphere validation case

Our time dependent, over-set mesh test case is the comparison of experimental drag forces computed on a sphere that is subjected to a passing shock wave. The experimental setup, performed at the Institute of Fluid Science, Tohoku University, Japan, is described in a paper by Tanno et. al. [Tanno et al., 2004]. In this experiment, a sphere was subjected to a M=1.22 shock wave impingement. The geometry for this case consisted of a 300mm×300mm square cross section shock tube where an 80mm diameter sphere was suspended on an elastic wire. The driver side of the shock tube consisted of nitrogen gas at a pressure of P=240kPa at room temperature, while the driven gas was air at atmospheric conditions. The post shock conditions for this case were a pressure of P=159.08kPa, a static temperature T=334K, and a velocity of 114.6m/s. The force exerted on the sphere as the shock passed was measured through accelerometers embedded in the sphere. For the duration of the experiment, the sphere movement was slight and one can reasonably approximate the sphere as a rigid body for computing the drag force for comparison with the experimental data.

We wish to validate the over-set mesh methodology that we will employ for our many-body problem to facilitate including debris motion. In this case, we are validating the utility of using this over-set methodology for accurately capturing shock-body interactions. In addition, we are attempting to get an estimate of the mesh resolution required to obtain a reasonably accurate solution. The more coarse the mesh we can use, potentially the more independent bodies we can consider in our debris simulation.

In this case we constructed the over-set mesh using a Cartesian mesh matching the square cross section of the shock tube and used an unstructured mesh to capture the geometry of the sphere. For the sphere mesh, we generated an unstructured mesh that extended to an interface sphere with a radius of 120mm. A Cartesian background mesh was generated for the 1000mm×300mm×300mm shock tube section. Mesh sizes were generated with a mesh spacing of 10mm, 5mm, and 2.5mm with the combined mesh sizes being 0.264M, 1.64M, and 11.5M cells respectively. For the all of these cases, a time-step of 1μs and 5 Newton iterations with second

order time differencing were employed. The Reynolds number for this case was 7.6×10^6. Menter's Shear Stress Transport (SST) turbulence model was utilized with solid viscous walls modeled using a wall law boundary condition with a viscous wall boundaries meshed with a normal spacing giving y^+ in the range of 50-100.

In Figure 4.1, the details of the mesh topology are shown for the 5*mm* case along with the density contours at a time 200μs after the shock hits the sphere. The cutting plane shows a cross section of the mesh illustrating the Cartesian mesh of the shock tube and the unstructured mesh that surrounds the sphere. Note that the unstructured sphere mesh is automatically cut by the over-set mesh facility due to proximity with the walls of the shock tube. Interpolation is used to couple the solution at the interface of the Cartesian and unstructured meshes.

The comparisons of the simulation results with the experimental data are shown in Figure 4.2. All grids produced reasonable comparisons to the experimental results, with the 5*mm* and 2.5*mm* grids producing nearly identical results. With the exception of a small peak in the experimental data at around 50μs, the simulations on all mesh resolutions produced excellent agreement with the experimental data. In addition, both experiment and simulations reproduced the curious effect of negative drag (occurring around 400μs) that is caused by a coalescence of shocks on the back side of the sphere. This test case shows that the code can accurately capture shocks passing though these interpolated regions. We also note that the 10*mm* mesh spacing, although very coarse, provided remarkably good agreement with experimental data. This suggests that we may be able to sacrifice mesh resolution without sacrificing the accuracy of our prediction in order to simulate a large number of bodies.

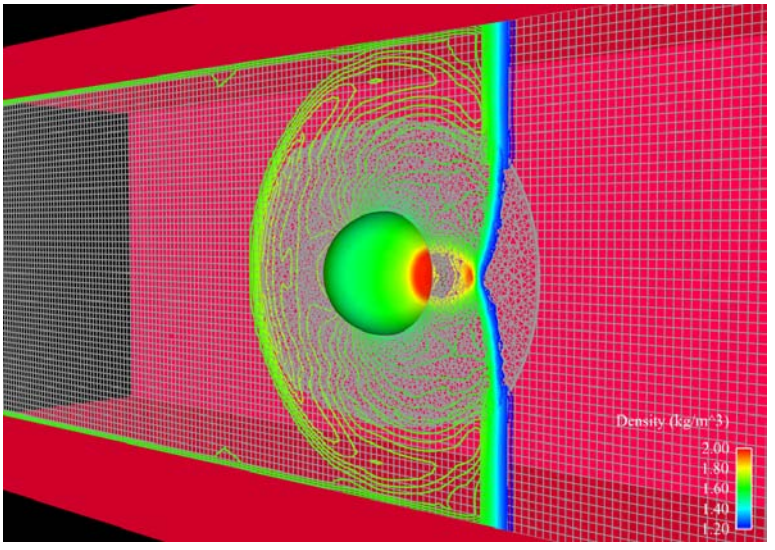

Figure 4.1: Density contours on cutting plane showing over-set mesh.

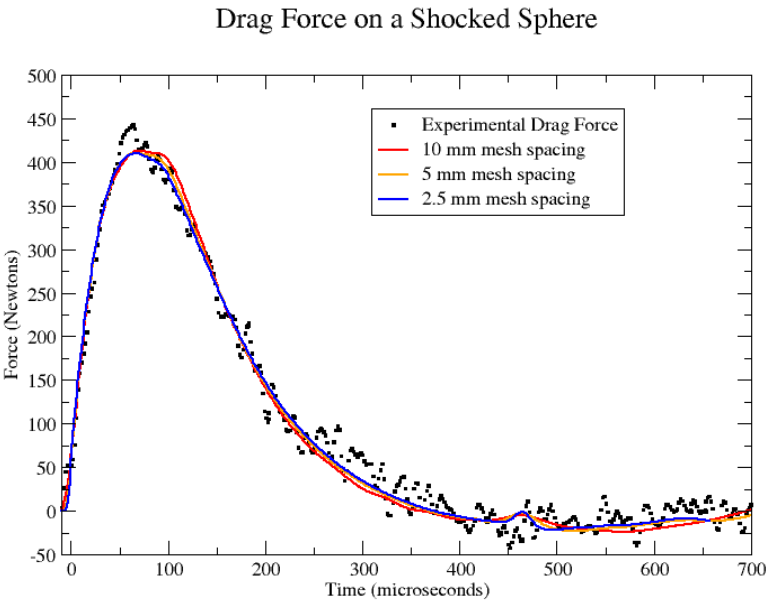

Figure 4.2: Drag force comparison.

4.2 Study of shock wave impinging on a single sphere

Before we performed the 6DOF simulations of blast-particle interactions, we first performed simulations of an isolated particle of various sizes with a range of impingement shock strengths in order to understand the time scales of various phenomena. Irregularity of the particle shape is beyond the scope of the current study; thus, only solid particles with spherical shape were considered. The particle was placed in a shock tube and the time history of the momentum flux exerted on the particle was computed.

Many studies have been conducted on shock wave interactions with particles at different length, time, and velocity scales [Sun et al., 2004, Liou and Takayama, 2004, Tanno et al., 2003, Saito et al., 2003]. The dynamic drag coefficient of a sphere due to shock wave loading was investigated numerically and experimentally by Sun *et.al* [Sun et al., 2004]. In their study, the unsteady drag of a sphere due to a shock wave of Mach number 1.22 was examined over a range of Reynolds numbers varying from 10^2 to 10^5, which is equivalent to the diameter of the sphere varying from $8\mu m$ to $80mm$. It was found that unsteady pressure loading due to shock interaction with the sphere is a dominant effect early in the interaction, especially for high Reynolds number cases. The effects of viscosity on the drag are negligible at this stage, although they become more important after the shock passes. The duration of the strong, unsteady shock-particle interaction is approximately the time for the shock wave to travel one sphere diameter. In our study, we intended to determine reasonable parameters for particles (e.g. particle diameter) and fluid conditions (e.g. Mach number) so that we have a basic understanding of how particles will respond during the time when the shock passes. Analysis based on the momentum equation for the particle showed that the speed the particle attains due to the initial shock impingement does not depend on the size of the particle, but rather on the density of the particle, the Mach number of the flow, and the density of the gas behind the approaching shock. According to our analysis, for quartz, with a density of $2650kg/m^3$ in our application, particles will have little response during the short duration of time that corresponds to the shock wave passing over the particle. Thus, the response of the particle to the initial blast wave will be dependent on the strength of the

wave and the relative densities of the blast wave and the material density of the particle. Therefore, unless the particle is very close to the expanding explosive cloud, the particle response will be much slower than the approaching shock. It is important to note that this observation appears to be true regardless of the particle size provided that the Reynolds number of the particle is on the order of 10^3 or greater. Over much longer durations of time, the effects of particle sizes will become more important.

Movement of the spherical particles due to the shock wave was computed using 6DOF, where no model was used for the coupling between flow and the particles. The above speculations on particle response to the flow will be tested. As preparation for the 6DOF simulation, the drag on stationary particles with different diameters under different shock speeds were simulated and compared with analysis.

Two Mach numbers, 2.5 and 5.0, were chosen for the impinging shock strengths and three different particle sizes were considered for each Mach number. Three representative particle diameters in soil are selected to be 0.05*mm*, 0.5*mm* and 5*mm*, which cover the range of sizes from a typical sand grain to small gravel. The Reynolds number ranges from 3×10^3 to 3×10^5 for Mach 2.5, and 8×10^3 to 8×10^5 for Mach 5. The definition of Reynolds number is

$$Re=\frac{\rho_0 U_0 d}{\mu_0}, \tag{4.1}$$

where d is the diameter of the sphere. This definition of the Reynolds number has been generally adopted to document the drag coefficients for a sphere. ρ_0, U_0, μ_0 are characteristic density, velocity and viscosity of the flow, and are taken as those behind the shock wave.

The results from our simulations are illustrated in Figures 4.3 and 4.4. These two plots are the dimensionless time history of the non-dimensional drag force (C_d) for two different Mach numbers. The physical time is non-dimensionalized using r/U_0, where r is the radius of the sphere and U_0 is the post-shock fluid velocity. The non-dimensional drag force is the drag coefficient, which is defined as

$$C_d=\frac{2f}{\rho_0 U_0^2 \pi r^2}, \tag{4.2}$$

where f is the drag force on the sphere. These simulations show that the particle size has minimal effect on the particle response to the shock wave in these size categories. Note that these curves overlay one another because of the non-dimensionalization applied. Thus, a particle is exposed to the strong shock loads for a shorter period of time for smaller size particles, while the forces are also reduced by the relative difference in the projected surface area of the particles. As a result, although a larger particle will receive an increased force, this force will be compensated by its increased mass such that the resulting acceleration the particle experiences will be similar regardless of particle size. This result suggests that for particles that have mass similar to soil, there will be very little motion of the particles during the immediate interaction with the blast wave, regardless of the particle size.

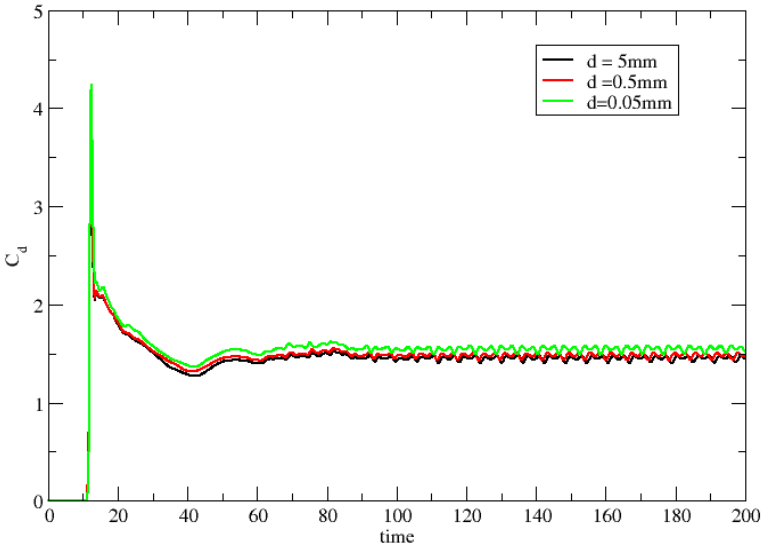

Figure 4.3: Time development of the drag coefficient on spheres with impinging shock speed of M=2.5.

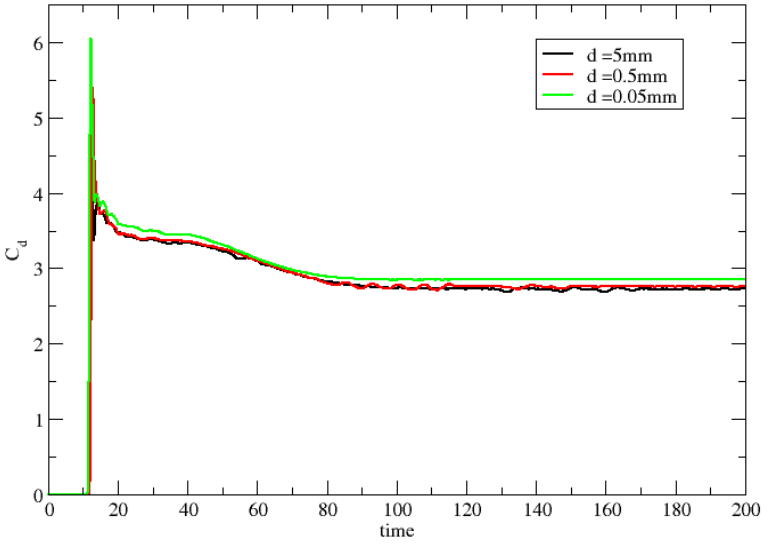

Figure 4.4: Time development of the drag coefficient on spheres with impinging shock speed of M=5.

4.3 Study of a normal shock wave impinging on multiple spheres

In this section, we will discuss the interaction of the flow field with multiple spheres. First, we study the flow of four spheres in a tandem configuration, separated by an equal distance, as illustrated in Figure 4.5. Three sphere diameters are taken to be 5*mm*, 0.5*mm* and 0.05*mm*. For each sphere diameter, simulations are performed for three equal inter-sphere spacings of s=1r, s=2r and s=6r, as illustrated in Figure 4.5. A shock wave moving at Mach 5.0 relative to the ambient air impinges on the spheres. Based on the previous validation exercise, a mesh size of 0.0625 times the sphere diameter is adopted in the simulations for each sphere size.

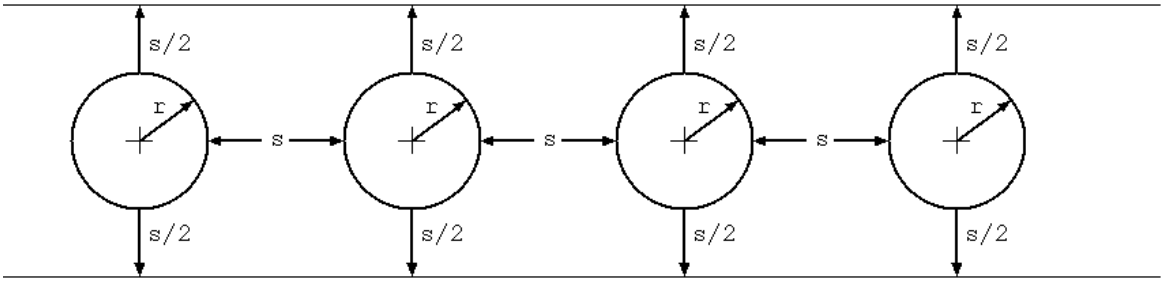

Figure 4.5: Schematic diagram of tandem particle configuration.

One of the important parameters for the study is the particle drag coefficient as defined in equation (4.2). In these cases, ρ_0 and U_0 are the characteristic density and velocity, respectively, and are taken to be the ambient density before the shock arrives and the velocity of the shock relative to the ambient velocity. According to equation (4.1), the Reynolds numbers are 6.4×10^5, 6.4×10^4 and 6.4×10^3 for 5*mm*, 0.5*mm* and .0.5*mm* diameter spheres, respectively. An example of the simulated pressure contours for a particle size of 5*mm* and a shock speed of M=5 with s=2r is shown in Figure 4.6.

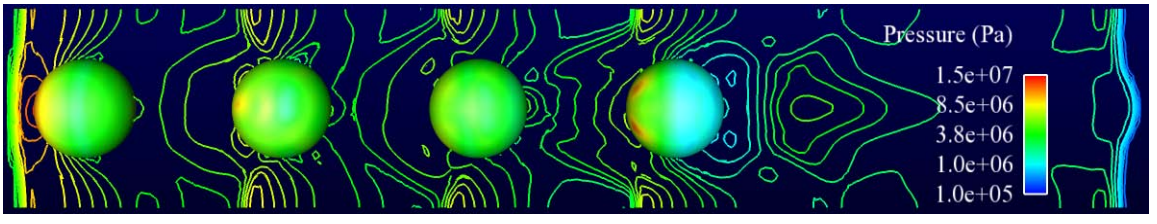

Figure 4.6: Simulated pressure contours for M=5, r=2.5*mm*, and s=2r.

The results of time evolution of the drag coefficient on the particles are shown in Figures 4.7-4.15 for three different sphere diameters at different spacings. Since there is a wide range of length scales for the spheres, the physical time is normalized by $\frac{r}{U_0}$, and non-dimensional time is used for the images. The figures show that for the same spacing between spheres, the drag coefficients are almost the same for the three different particle sizes. This indicates that pressure drag (inviscid force) is the main contributor to the total drag, and the viscous drag is not

significant for the particle Reynolds numbers studied in the present cases. It is also evident that the spheres experience a steep drag increase due to shock impingement and that the drag drops precipitously as the shock wave moves to the rear side of the sphere. The maximum drag on spheres 2, 3 and 4 is larger than that on the first sphere because the flow accelerates after passing the leading sphere and is then focused on the following sphere. The shock weakens as it travels downstream with the presence of the spheres because of the effects of shock reflections, which may be considered blockage effects. The blockage effect is more obvious when the spheres are closer together; thus, the maximum drag exerted on spheres 3 and 4 decreases for 1*r* and 2*r* spacing, as shown in the figures. However, when the distance between spheres is larger, the blockage effect becomes less significant, as does the focusing effect. Therefore, the spheres behave more like isolated individual particles without much interaction, as depicted in Figures 4.9, 4.12, and 4.15. Another important observation made from those figures is that the drag values at steady state for the first and last spheres are higher than those for the middle spheres. There are two phenomena that are responsible for this effect: 1) the leading sphere experiences an increased pressure on its trailing side due to a supporting effect of the following sphere, while the trailing sphere experiences a much lower pressure on the trailing side and 2) the leading sphere sees an increased stagnation pressure, while the trailing spheres experience a shielding effect from the spheres ahead of it. So the middle spheres experience both a shielding effect from the particle ahead of it and a supporting effect from the particle that trails it. The leading particle does not benefit from a shielding effect, while the trailing particle does not benefit from a supporting effect. Therefore, we expect more loading will be experienced at the leading and trailing edges of the particulate cloud. As seen in the figures, the difference between steady state drag on spheres at different locations appears to be smaller as the spacing between the spheres becomes larger since the shielding and supporting effects related to the particle-particle interactions tend to decrease with increasing particle spacing.

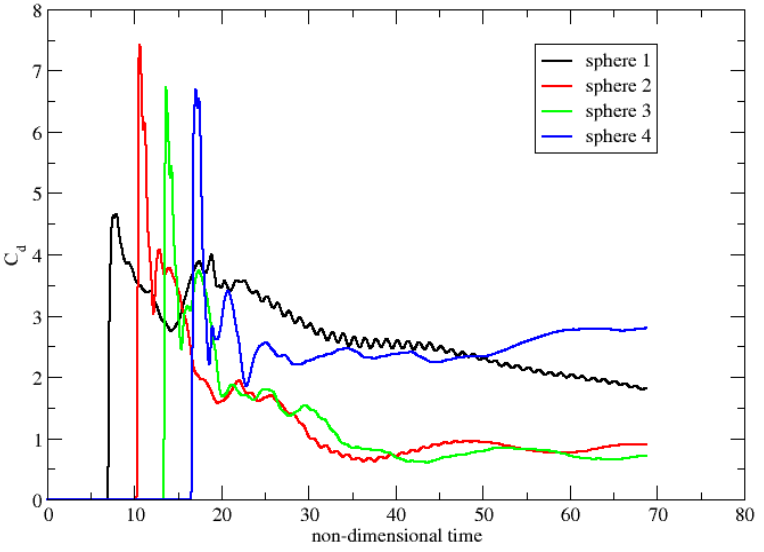

Figure 4.7: Drag coefficient of shock wave loading on spheres with 5*mm* diameter and *s*=1*r*.

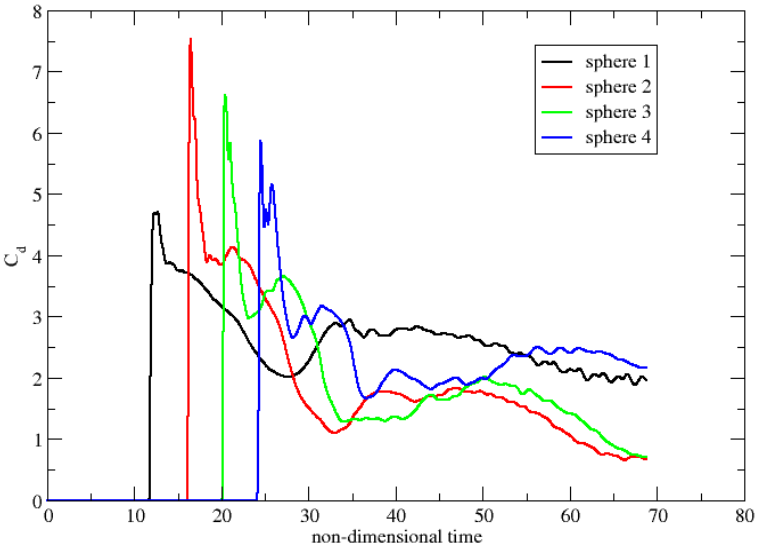

Figure 4.8: Drag coefficient of shock wave loading on spheres with 5*mm* diameter and *s*=2*r*.

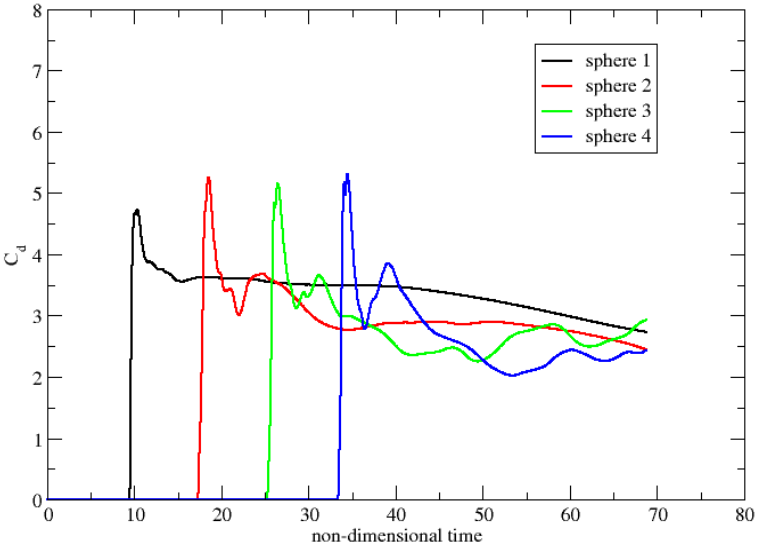

Figure 4.9: Drag coefficient of shock wave loading on spheres with 5*mm* diameter and *s*=6*r*.

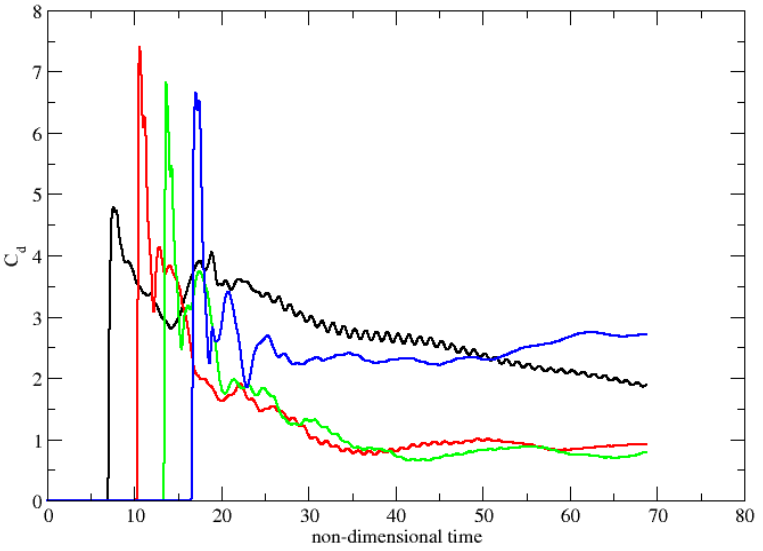

Figure 4.10: Drag coefficient of shock wave loading on spheres with 0.5*mm* diameter and *s*=1*r*.

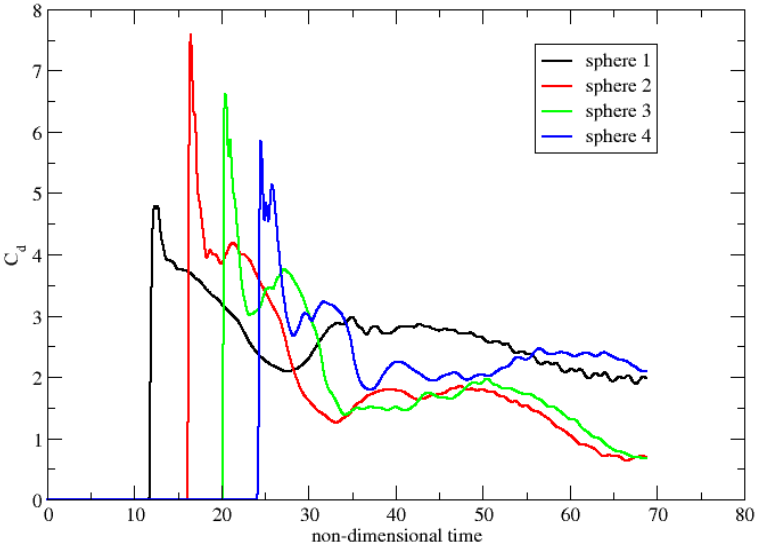

Figure 4.11: Drag coefficient of shock wave loading on spheres with 0.5*mm* diameter and *s*=2*r*.

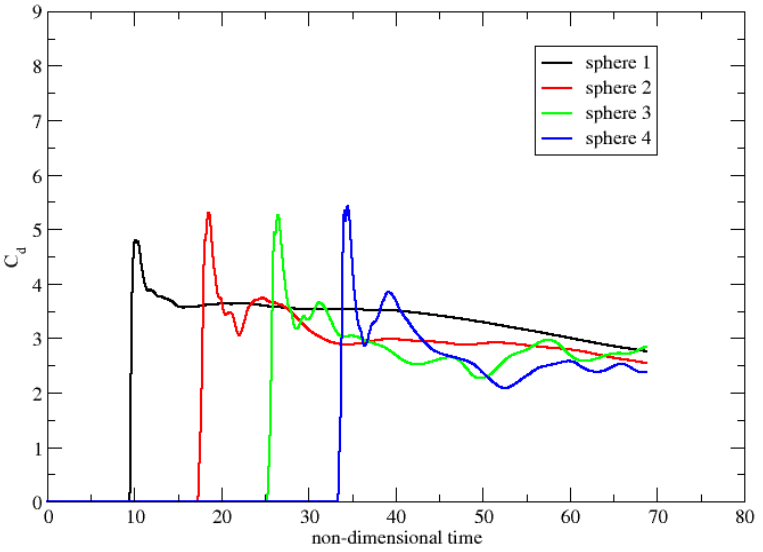

Figure 4.12: Drag coefficient of shock wave loading on spheres with 0.5*mm* diameter and *s*=6*r*.

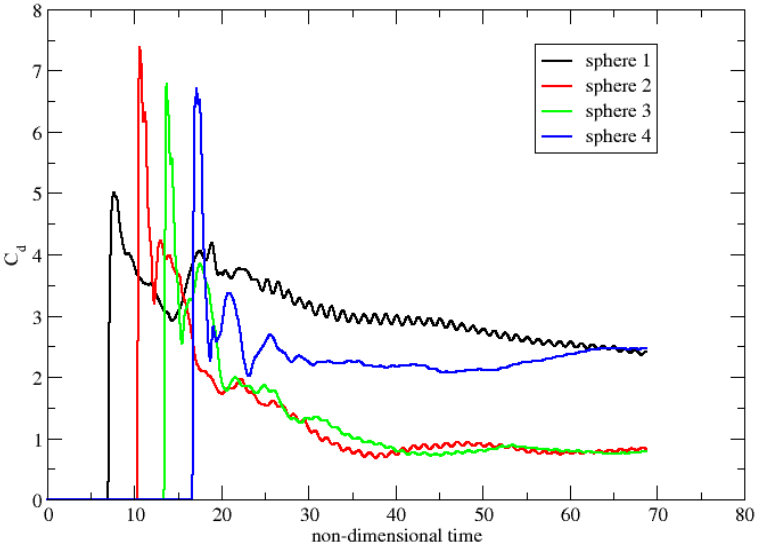

Figure 4.13: Drag coefficient of shock wave loading on spheres with 0.05*mm* diameter and *s*=1*r*.

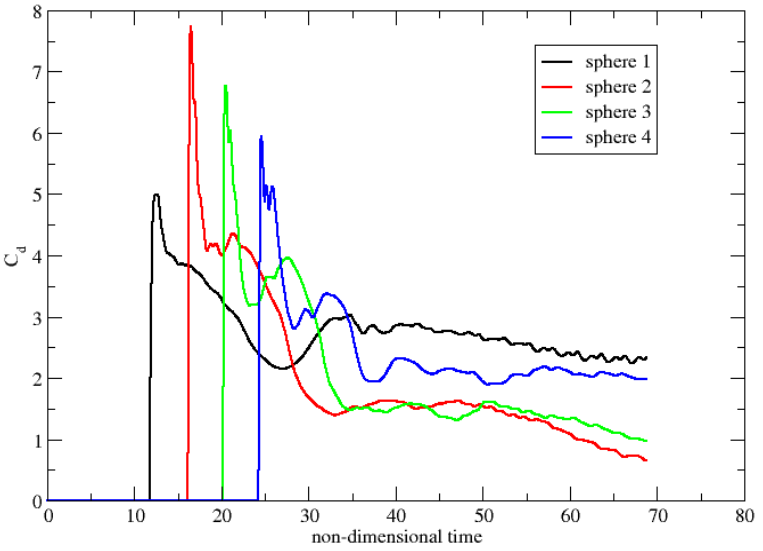

Figure 4.14: Drag coefficient of shock wave loading on spheres with 0.05*mm* diameter and *s*=2*r*.

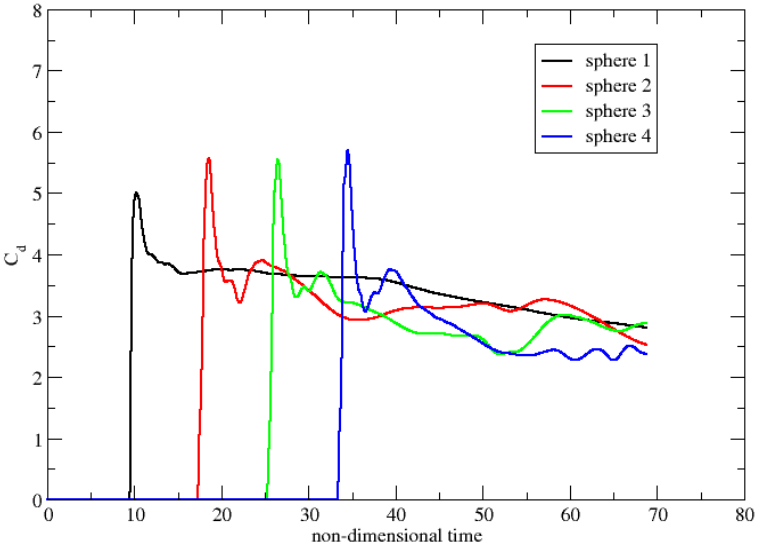

Figure 4.15: Drag coefficient of shock wave loading on spheres with 0.05*mm* diameter and *s*=6*r*.

Figures 4.16-4.19 compare the drag coefficient for the three different diameters of the spheres at the largest particle spacing (*s*=6*r*). As mentioned above, the particle drag coefficients for each different size of sphere are almost the same for the particle Reynolds number in our present studies, which is again demonstrated in this plot. Although the viscous drag in not significant, it is still observed that the viscous effect increases with the decrease of particle Reynolds number (smaller particle size).

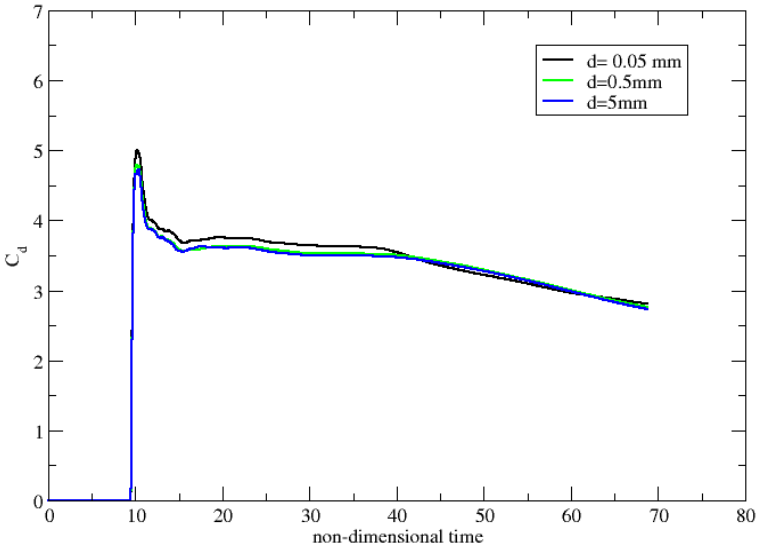

Figure 4.16: Comparison of drag coefficients on leading sphere with different diameters for *s*=6*r*.

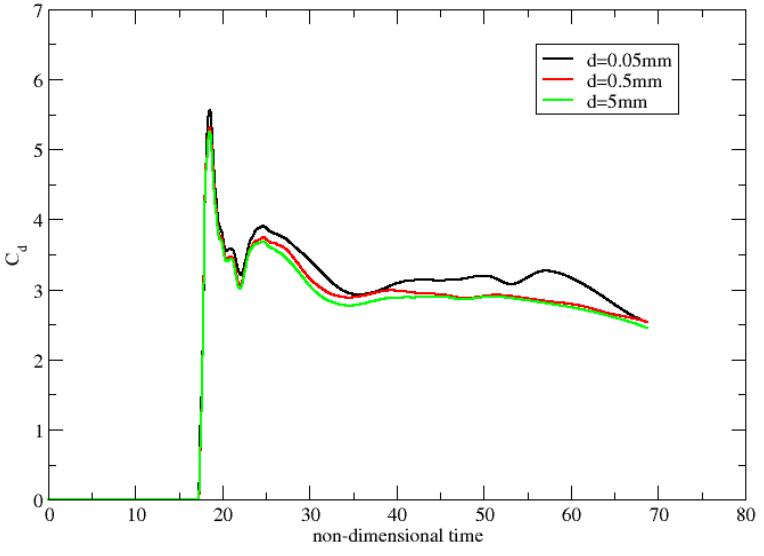

Figure 4.17: Comparison of drag coefficients on second sphere with different diameters for *s*=6*r*.

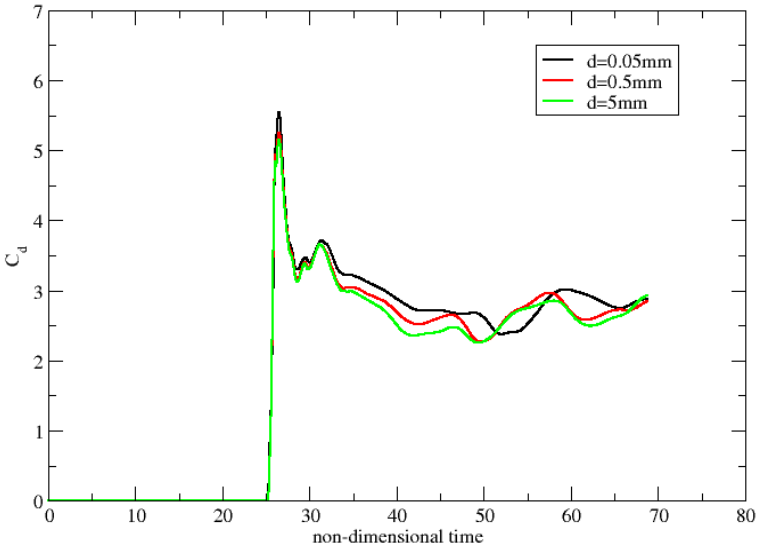

Figure 4.18: Comparison of drag coefficients on third sphere with different diameters for *s*=6*r*.

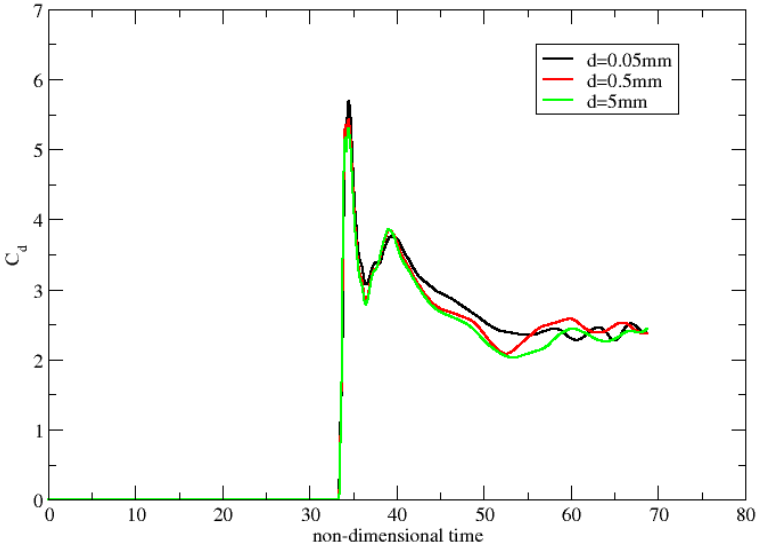

Figure 4.19: Comparison of drag coefficients on trailing sphere with different diameters for *s*=6*r*.

Figures 4.20-4.22 show the computed particle velocities for the 5mm diameter tandem spheres. The velocities in these plots were shifted so that they all start with a zero time at the time of arrival. If the inter-particle interactions are negligible, we would expect these curves to be identical. We note for a sphere spacing of 1 sphere radius, we have significant differences between the particles with the first and last sphere gaining the most momentum from the flow. The middle particles acquired significantly less momentum from the shock impingement. The middle particles have both a shielding effect from the wake of the sphere ahead of it, while they also have a supporting effect from their own wake interacting with the sphere that trails them.

Both of these effects have the result of reducing the drag on the particle. Since the leading particle does not have a shielding effect, and the trailing particle does not have a supporting effect, these two particles experience a larger drag than the middle particles. We see that as we increase the sphere spacing to 1 sphere diameter, the degree of difference between the leading, middle, and trailing particles is much less, as is observed in Figure 4.21. For the case where the sphere spacing is 3 diameters, as shown in Figure 4.22, we see that the spheres experience a decreasing momentum transfer as we proceed down the line of particles. However, the leading and trailing particles do not show a particular departure from the trend. We observe that this effect could simply be explained by the loss of fluid momentum due to the drag of the particle ahead of it, and the shielding and supporting effects appear to no longer be playing a role in the fluid-particle coupling.

The variation of sphere velocities with the spacing between them is plotted in Figures 4.23-4.26. It is expected that the velocity increases with increasing sphere spacing since the damping (including the shielding and supporting effect) from other spheres weakens with increasing distance between the spheres. The velocity of leading and middle spheres (Figures 4.23, 4.24, and 4.25) supports this hypothesis, while the reverse trend is observed for the trailing sphere. The anomaly may come from the complex behavior in the wake region. It is seen that the velocities of the two middle spheres are more sensitive to the spacing since they feel both the shielding and supporting effects from the spheres in front and behind, while the first and last spheres do not experience as much interaction from other spheres. We also note that the interactions appear to be complex and nonlinear. For example, in Figure 4.23, the lowest particle velocity is obtained for the intermediate spacing. From the graph it appears that this is due to a transient interaction between particles that occurs at about 10 microseconds. Nonetheless, the general slope after this transient event still supports our hypothesis regarding the supporting effect on the leading sphere.

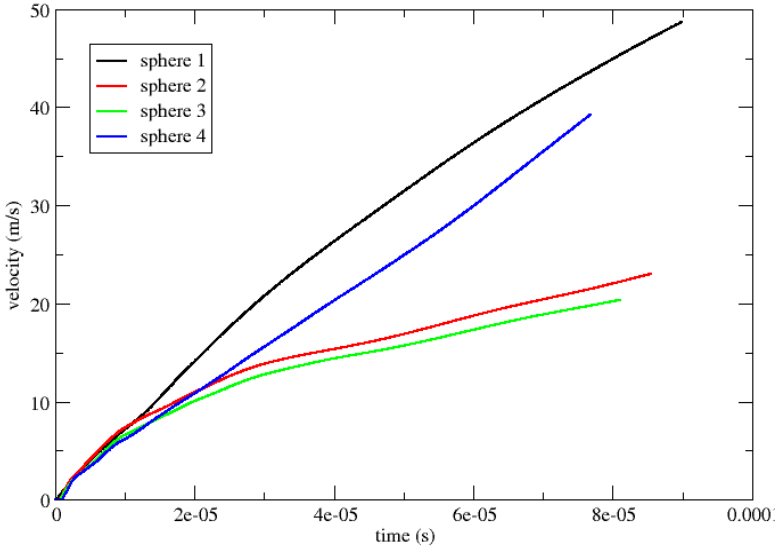

Figure 4.20: Comparison of velocity for different spheres (*d*=5*mm*, *s*=1*r*).

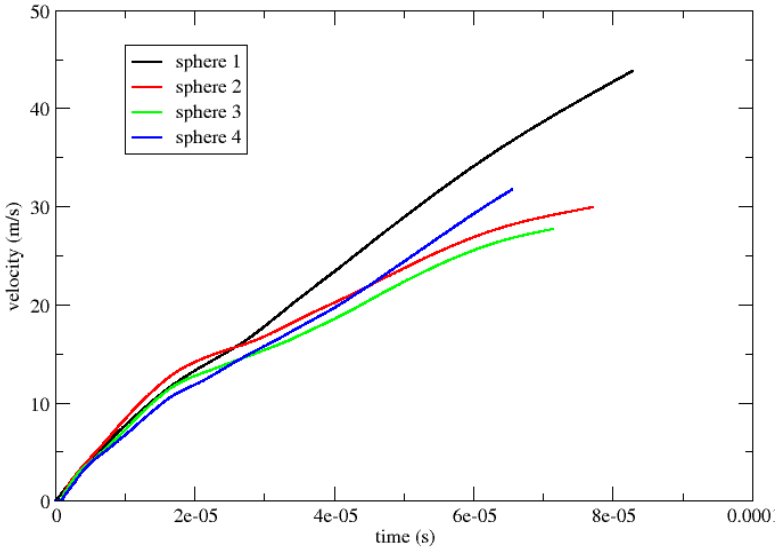

Figure 4.21: Comparison of velocity for different spheres (*d*=5*mm*, *s*=2*r*).

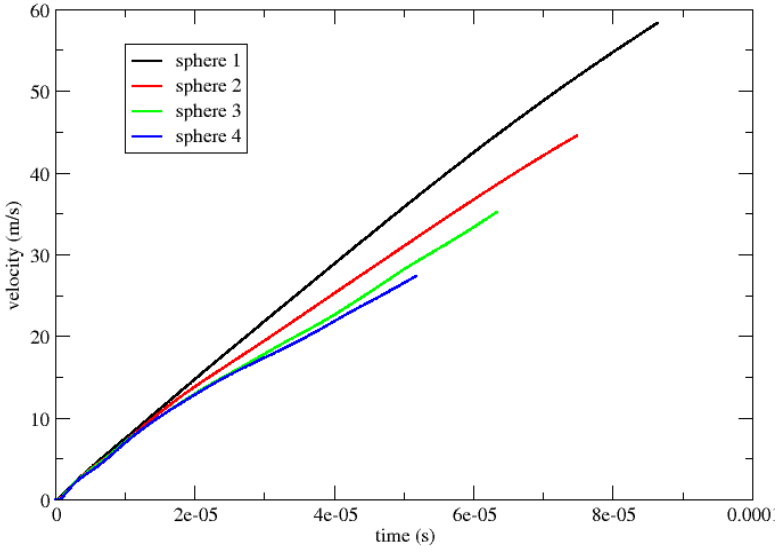

Figure 4.22: Comparison of velocity for different spheres (*d*=5*mm*, *s*=6*r*).

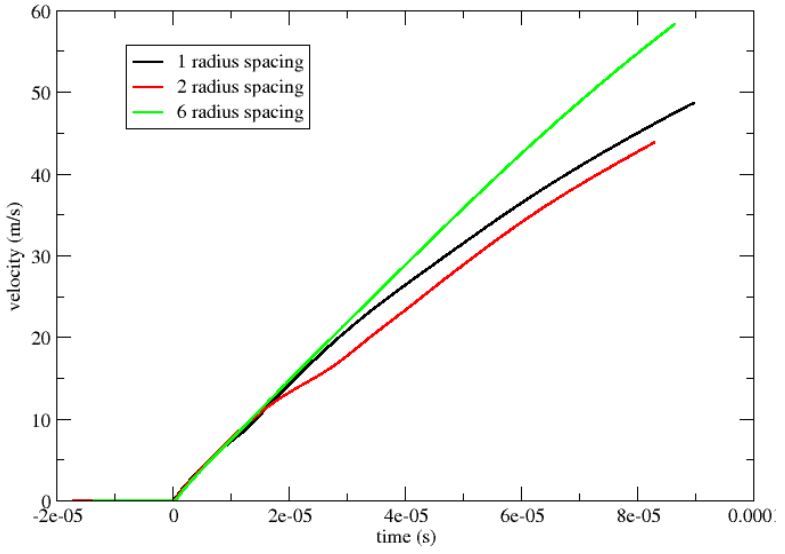

Figure 4.23: Comparison of velocity of leading sphere (*d*=5*mm*) for different particle spacings.

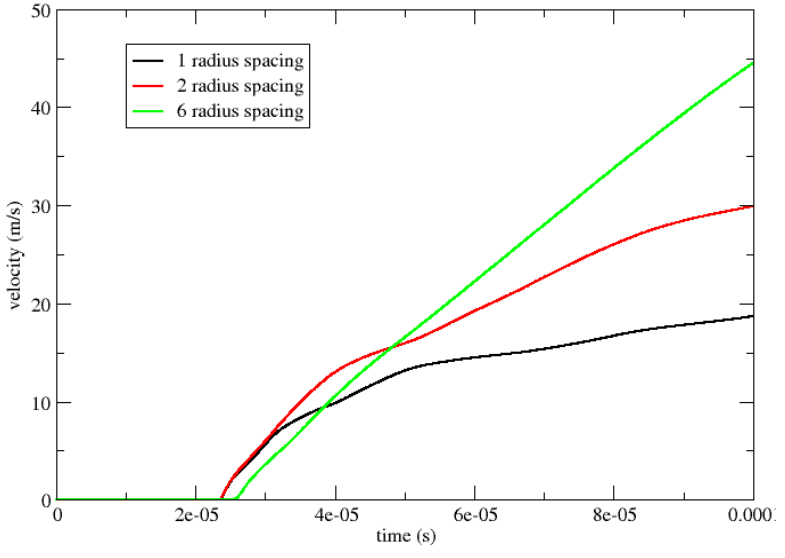

Figure 4.24: Comparison of velocity of second sphere (*d*=5*mm*) for different particle spacings.

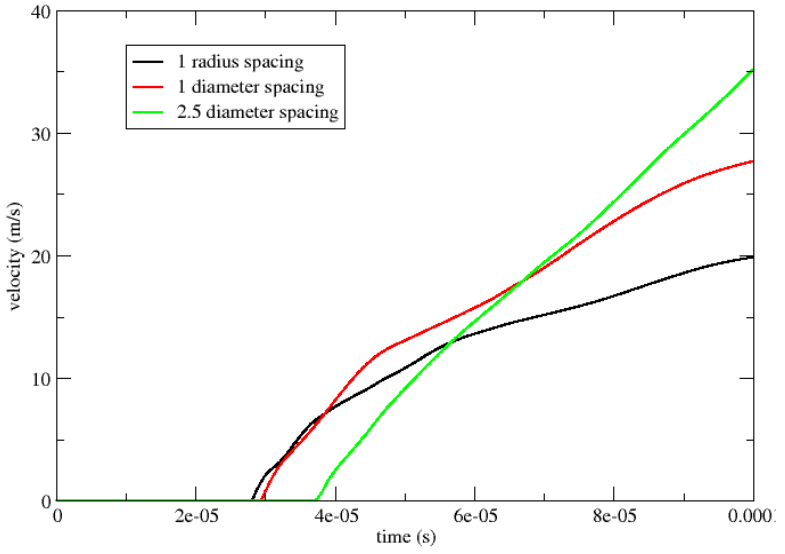

Figure 4.25: Comparison of velocity of third sphere (*d*=5*mm*) for different particle spacings.

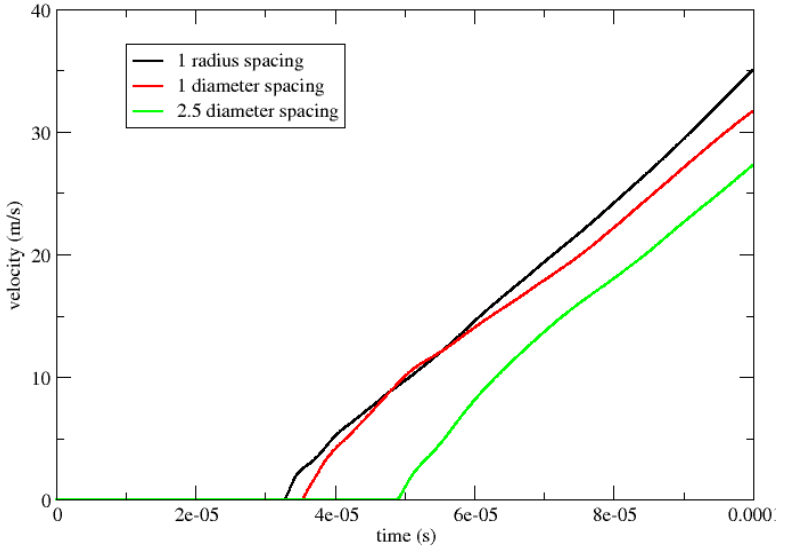

Figure 4.26: Comparison of velocity of trailing sphere (*d*=5*mm*) for different particle spacings.

The predicted movement of the spheres is illustrated in Figures 4.27-4.29. The four spheres travel a small distance and do not have the chance to collide during the time frame simulated in the present study. Figures 4.30-4.33 compare the movement of spheres at different sphere spacings. The distance the spheres move is in agreement with the velocity profile depicted in Figures 4.23-4.26, but the spheres with larger spacing start moving at a later time, as expected.

To reduce the computational expense, all the above results were obtained in the one-way coupled frame in which the spheres are stationary and the time-integrated drag force is employed to compute the velocities and positions as a post-processing procedure. However, one simulation

was performed in the two-way coupled frame where the spheres move in the flow and exert an influence on the flow field. The sphere moves with six degrees of freedom (6DOF) under the integrated force from the flow on the sphere surface and sphere body force. Figure 4.34 compares the results between the one-way and two-way coupled simulations. The two types of simulations provide identical results for the current problem.

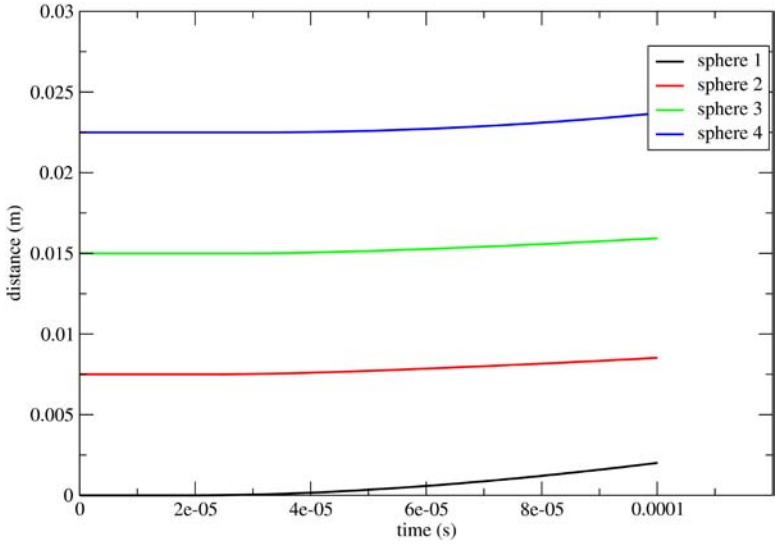

Figure 4.27: Position of spheres (*d*=5*mm*) along shock tube axis with *s*=1*r*.

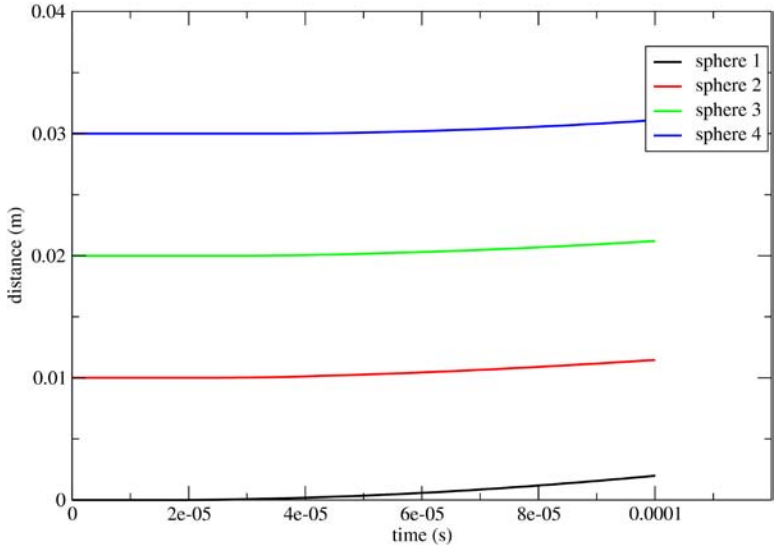

Figure 4.28: Position of spheres (*d*=5*mm*) along shock tube axis with *s*=2*r*.

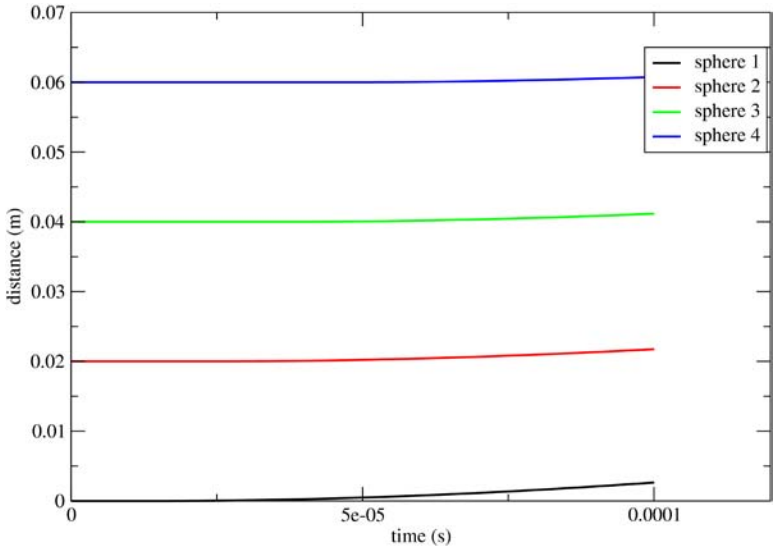

Figure 4.29: Position of spheres (*d*=5*mm*) along shock tube axis with *s*=6*r*.

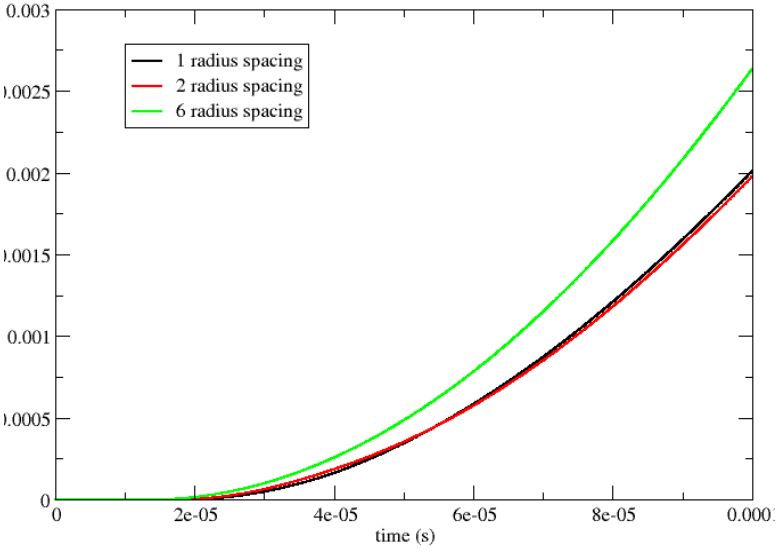

Figure 4.30: Position of leading sphere (*d*=5*mm*) along shock tube axis for different spacings.

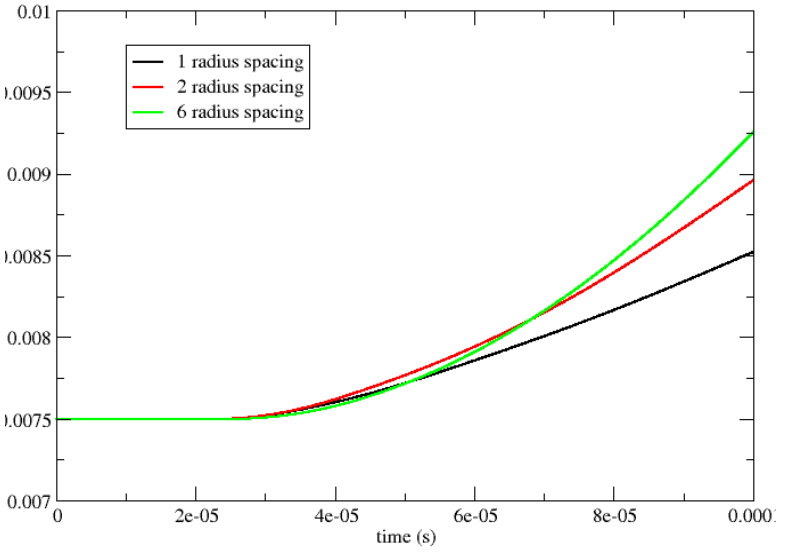

Figure 4.31: Position of second sphere (*d*=5*mm*) along shock tube axis for different spacings.

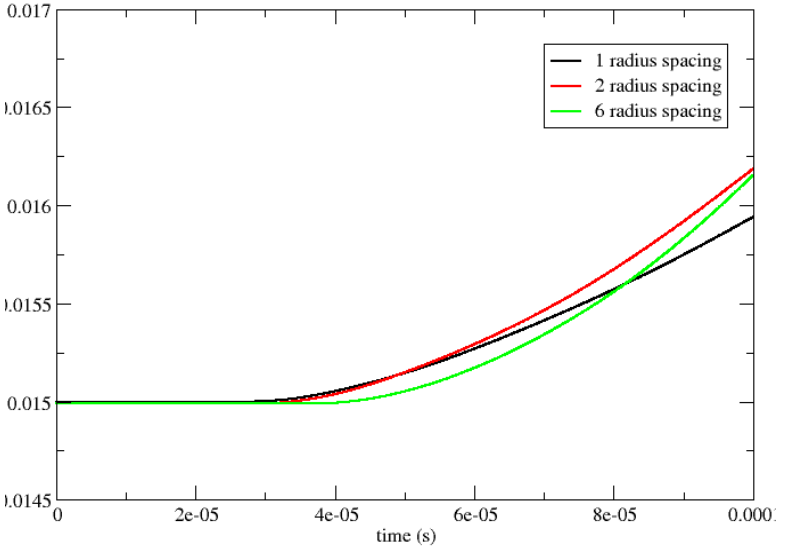

Figure 4.32: Position of third sphere (*d*=5*mm*) along shock tube axis for different spacings.

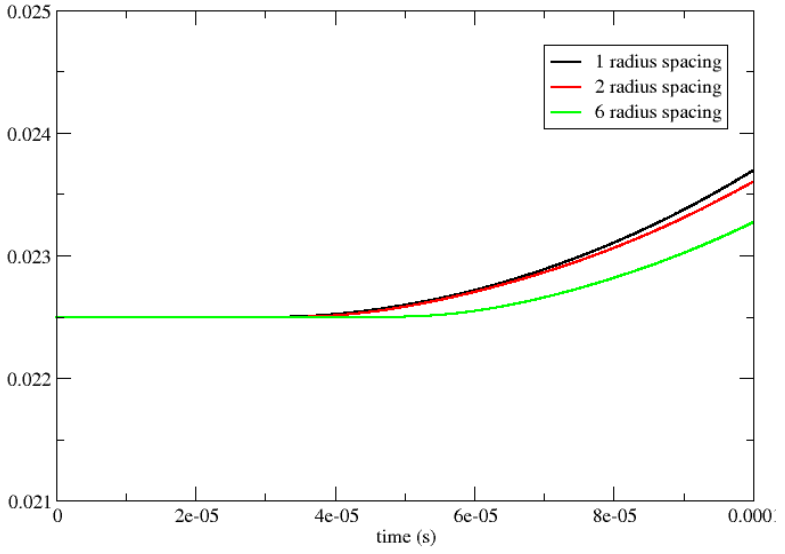

Figure 4.33: Position of trailing sphere (*d*=5*mm*) along shock tube axis for different spacings.

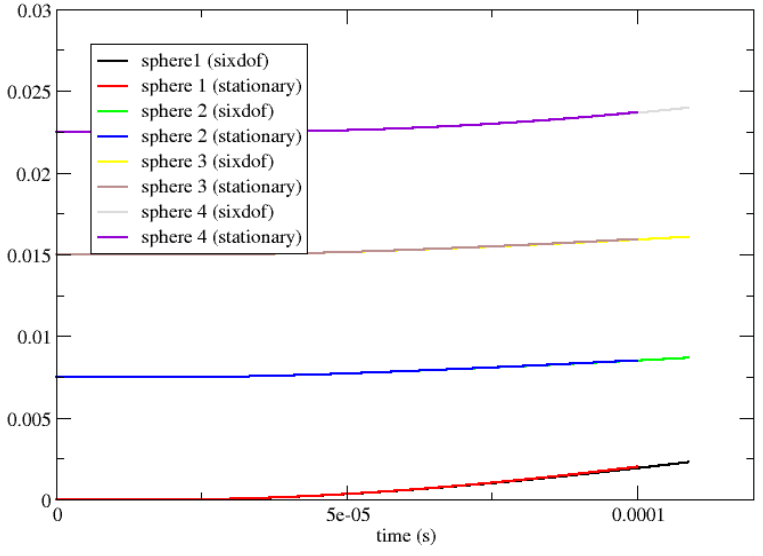

Figure 4.34: Comparison of positions for stationary and moving spheres.

4.4 Study of a normal shock wave impinging on multiple staggered spheres

Next, a staggered sphere configuration was considered. This configuration is an arrangement of six spheres, with one leading sphere, four middle spheres, and one trailing sphere. A diagram of the layout of the four spheres that are aligned with the z=0 plane is shown in Figure 4.35. Sphere #3 and sphere #5 are not shown and will appear at positive and negative z coordinates, respectively. The lines at the top and bottom of this schematic are the location of periodic boundaries.

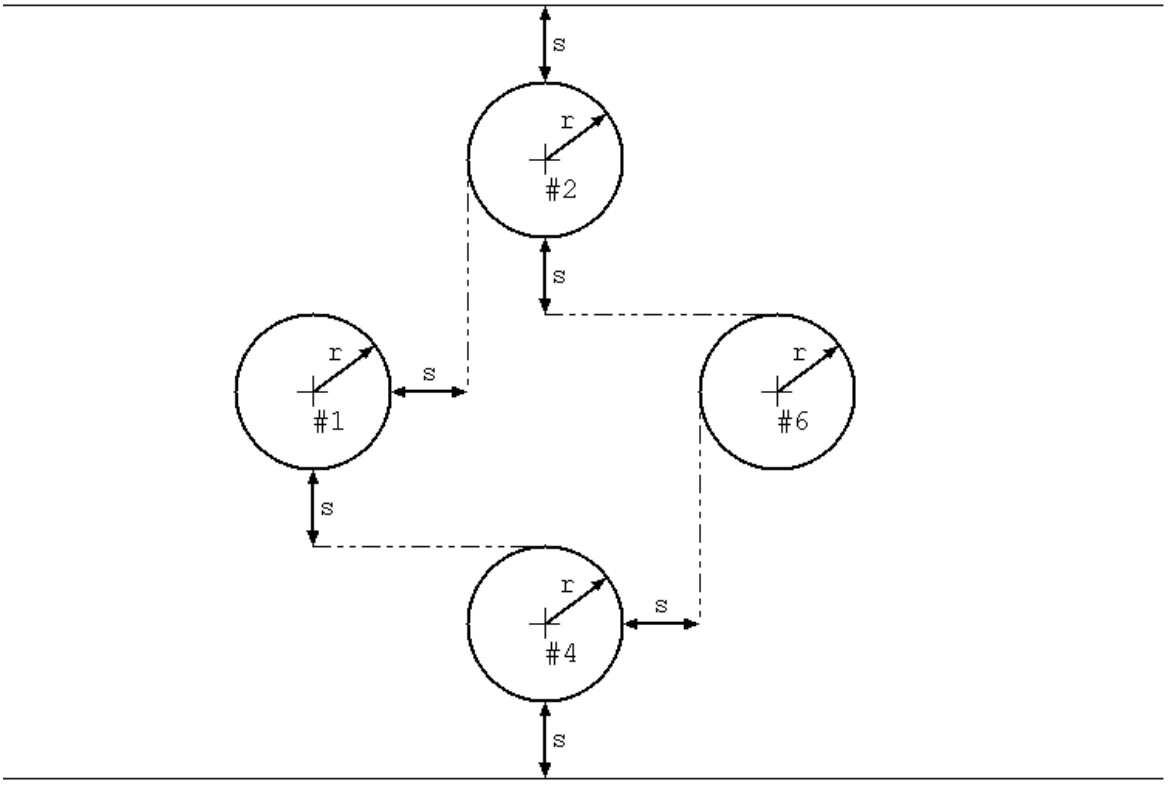

Figure 4.35: Schematic diagram of sphere layout for staggered case showing spheres located on z=0.

Figure 4.36 shows an instantaneous snapshot of pressure contours just as the Mach 5.0 shock wave is passing over the trailing sphere in the staggered configuration. Figure 4.37 shows the time history of the drag coefficient on the six spheres. The results on the four spheres in the middle plane are almost identical due to the symmetry of the particle layout. The maximum drag on the four middle spheres is almost equivalent to the drag on the first one because there are no spheres in front directly blocking the flow, which provides a shielding effect. In addition, we don't observe a significant focusing effect due to the presence of the leading sphere. A sharp increase of maximum drag on the last sphere (sphere 6) is caused by the fact that the flow accelerates when passing the middle four spheres, which focuses the flow down the central core directly onto the trailing sphere. Contrary to the tandem case, the steady state drag on the middle four spheres is higher since there are no shielding and supporting effects presented to those

spheres. The lower steady state drag force on the last sphere results from the shielding effect from the first sphere.

The velocities and positions of the six spheres in the staggered configuration are examined in Figures 4.38 and 4.39. As expected, the middle four spheres move faster when compared to the first and last spheres since there is no direct impact from other spheres. Like the tandem case, the spheres still do not travel fast enough to collide with each other.

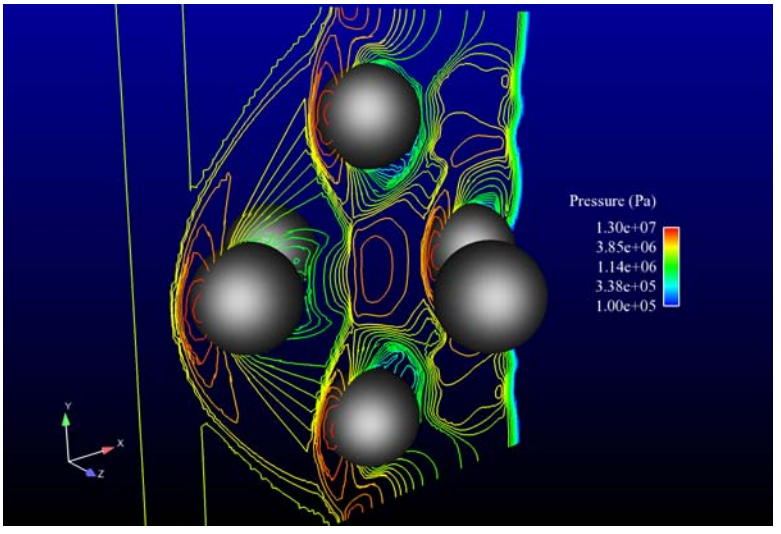

Figure 4.36: Instantaneous pressure contours for staggered configuration (*d*=5*mm*, *s*=1*r*).

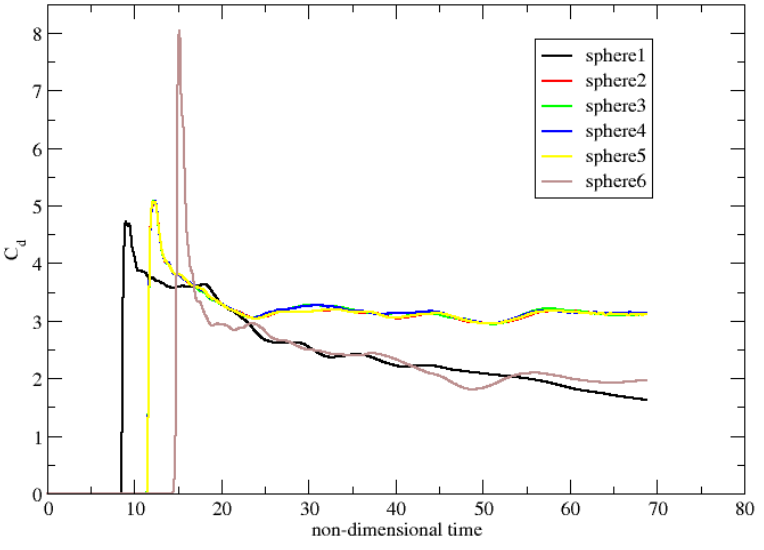

Figure 4.37: Drag coefficient on spheres for staggered configuration (*d*=5*mm*, *s*=1*r*).

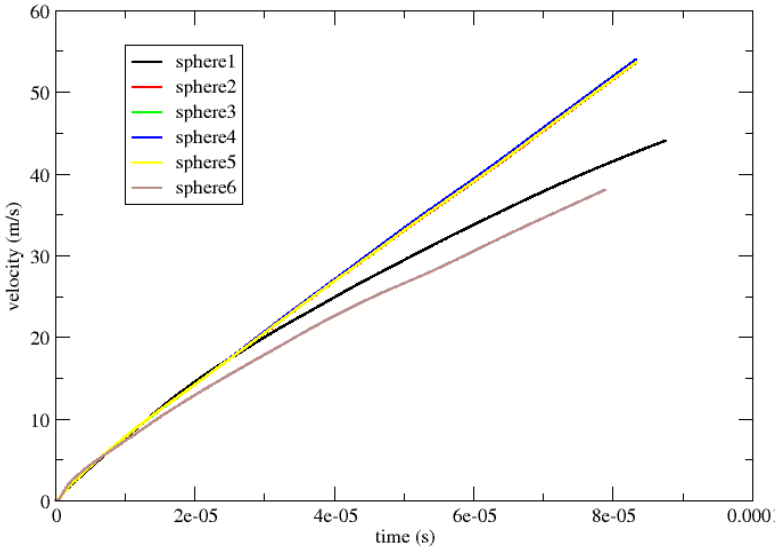

Figure 4.38: Velocity of spheres (*d*=5*mm*, *s*=1*r*) for staggered configuration.

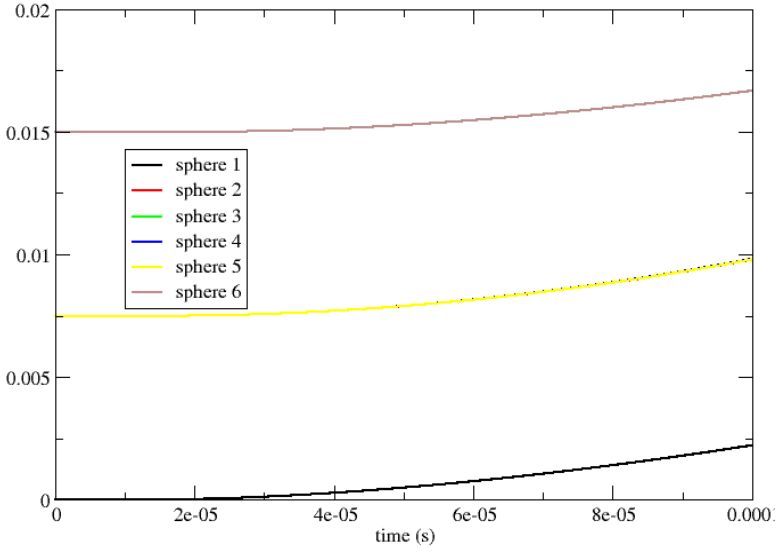

Figure 4.39: Distance of travel for spheres (*d*=5*mm*, *s*=1*r*) for staggered configuration.

In order to demonstrate how the layout of particles can affect the particle dynamics, a comparison of velocity and position between the staggered and tandem configurations is provided in Figure 4.41. Only the middle spheres, having the same distance (in the axial shock tube direction) relative to the first sphere, are selected for this comparison. It is obvious that the particle configuration plays a significant role in the dynamics of spheres. The shielding and supporting effects on the middle sphere in the tandem layout reduces the movement of the sphere significantly.

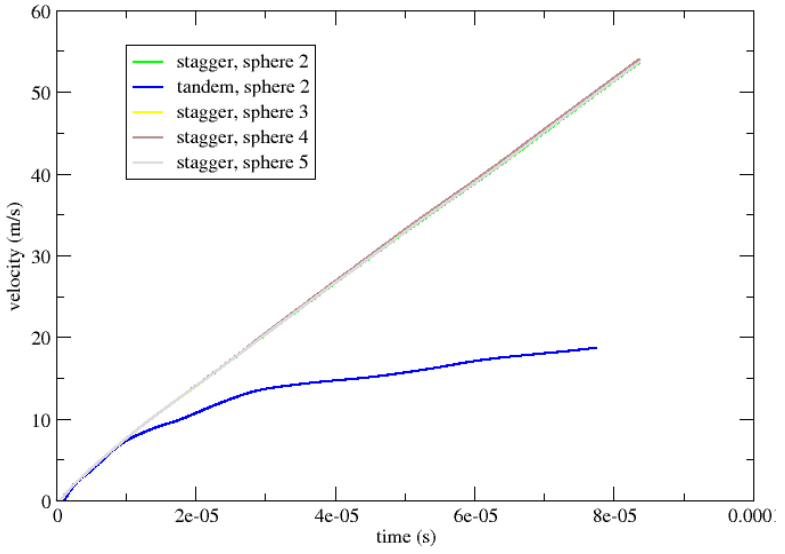

Figure 4.40: Comparison of velocity of spheres (*d*=5*mm*, *s*=1*r*) between staggered and tandem configurations.

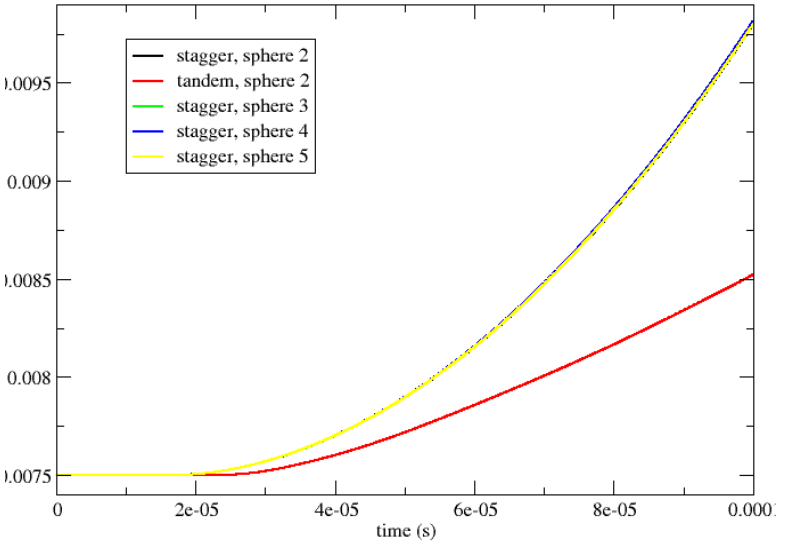

Figure 4.41: Comparison of distance traveled for spheres (*d*=5*mm*, *s*=1*r*) between staggered and tandem configurations.

From the numerical studies of the shock interaction with micro-spheres for a particle Reynolds number ranging from 6×10^3 to 6×10^5, we may draw the following conclusions. First, the size of the particles in the regime of the current application does not affect the dynamics of the particles. Second, the spacing between multiple particles and the layout of the particles play an important role in the movement of the particles. The shielding effect from upstream and the supporting effect from downstream particles can slow down the particle, and these effects are most pronounced in the tandem configuration. However, the focusing effect from the acceleration of the flow past the sphere could impose a boosting force on the sphere downstream. Finally, the unsteady force from the shock impingement does not have a significant influence on particle dynamics. Instead, the steady state force plays a much more significant role.

4.5 Study of a blast wave impinging on multiple particles

After investigating the behavior of particles in a shock tube, we conducted a study on a notional blast wave interaction with particles. To generate the blast wave, we performed an axisymmetric simulation of a surface-laid hemispherical charge of TNT with a radius of 144mm and a mass of 10.19kg. We used an ideal gas model with high-pressure conditions within a sphere to model the detonated TNT. The two-dimensional simulation was run until the blast wave had expanded to about r=1.8m from the center of the TNT charge. At this point, we interpolated the axisymmetric solution onto a three-dimensional grid that consisted of a solid angle slice of a spherical domain. We used reflecting conditions on the boundaries of this solid angle. The three dimensional grid in which we embedded the particles is shown in Figure 4.42. Before embedding the particles, we utilized adaptive mesh refinement in the regions where we would be resolving the blast-particle interaction. Specifically, we refined two levels over the general region where the blast wave would be present for the simulation and another two levels in the immediate region where the particles were placed, as illustrated in Figure 4.43. Ten particles were arranged in a staggered formation configured in two planes. Each plane contains a configuration similar to a “five” die face with the subsequent plane rotated by 45 degrees. These ten particles were given a diameter of 1cm and density of 2650kg/m^3 and were located just before the front of the interpolated blast wave. These ten particles are equally divided into two planes located at r=1.82m and r=1.84m perpendicular to the approaching blast wave, as illustrated in Figure 4.44.

Figures 4.45-4.49 show the evolution of the blast wave impinging on the particle configuration. In this figure, symmetry illustrates how the simulation represents a larger particle cloud. From this simulation, a complex set of shock structures emerges that is similar to the normal shock simulations described earlier. In Figure 4.49, there is considerable variation in particle velocities, as illustrated by the particle colors. The source of these differences in particle velocity can be seen in the time history of the particle drag forces, as shown in Figures 4.50 and 4.51. Compared with particles in the shock wave presented in the last section, the drag force on spheres in blast waves exhibit similar general behavior of peaking and falling. However, the drag force at steady state after the blast wave passes decreases rapidly, which is a result of the blast wave’s expanding surface area, causing a rapidly decreasing pressure profile.

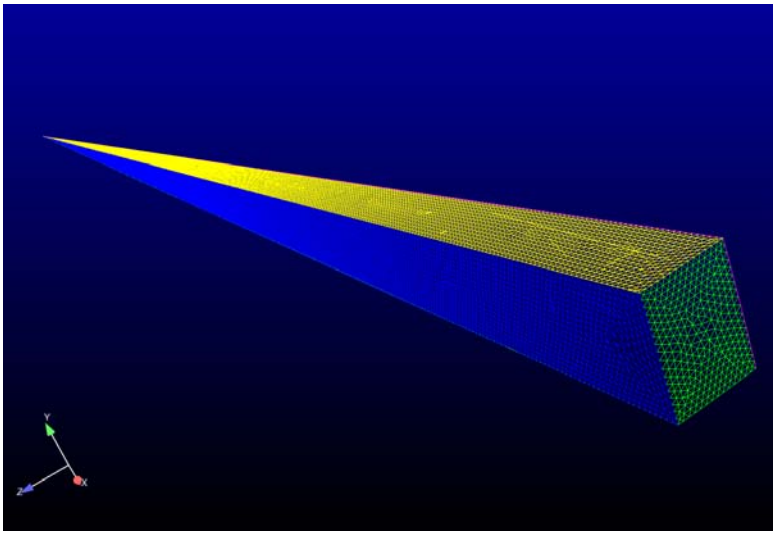

Figure 4.42: Solid angle partition of sphere used for blast-particle simulation.

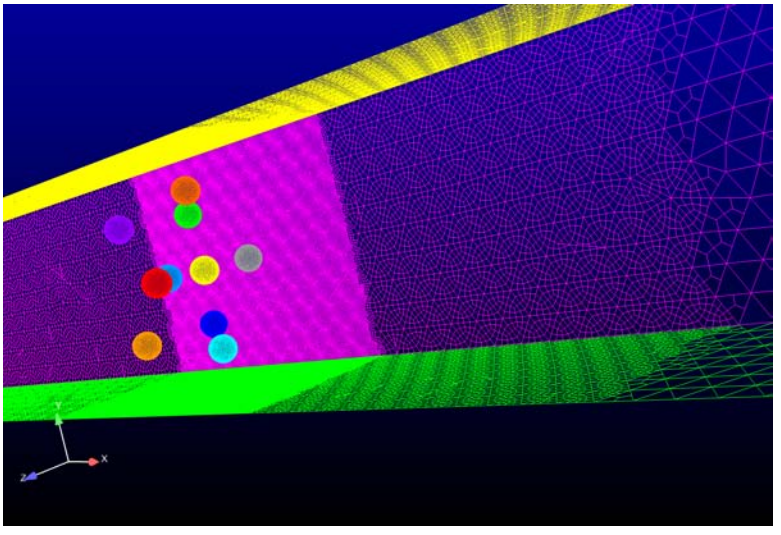

Figure 4.43: Refined solid angle mesh in particle region.

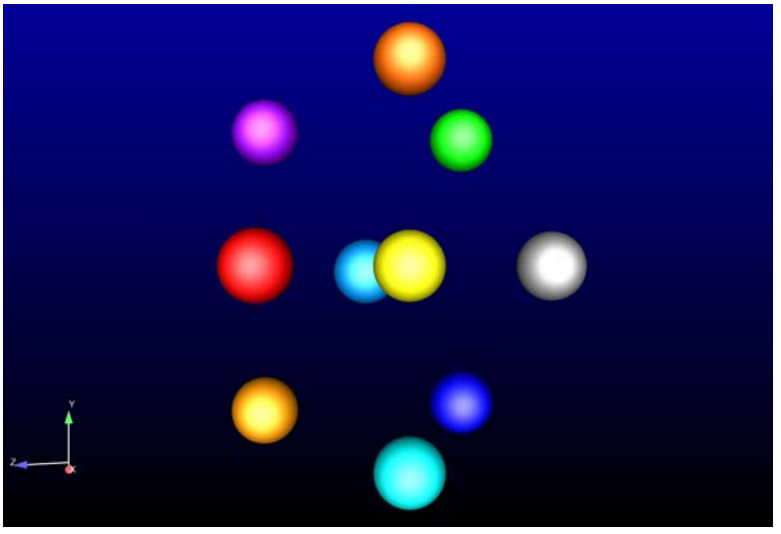

Figure 4.44: Configuration of ten particles used in blast-particle simulation.

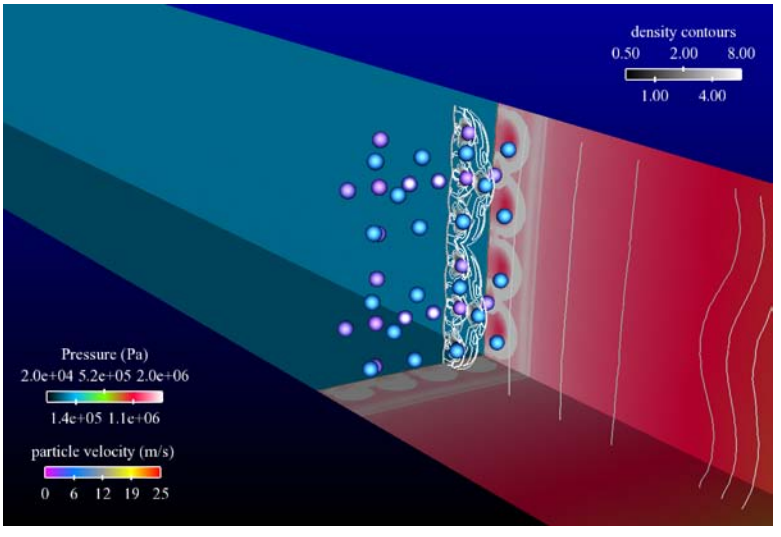

Figure 4.45: Time evolution of blast-particle interaction at 50*μs*.

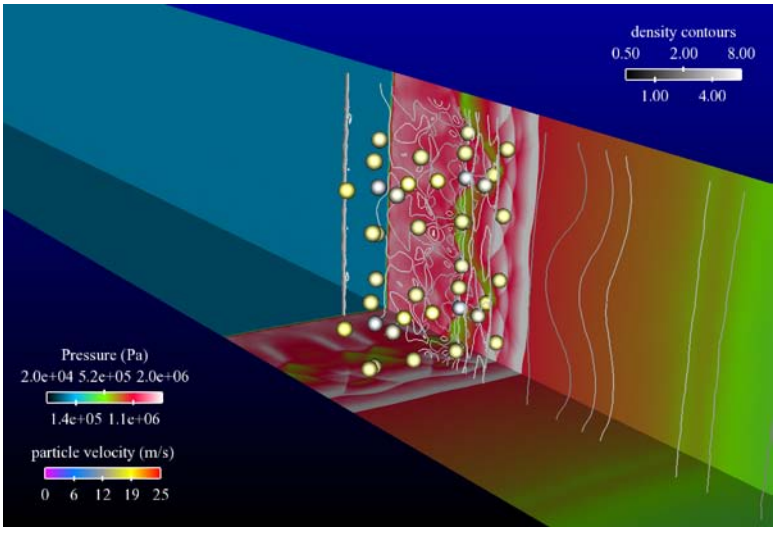

Figure 4.46: Time evolution of blast-particle interaction at 150μs.

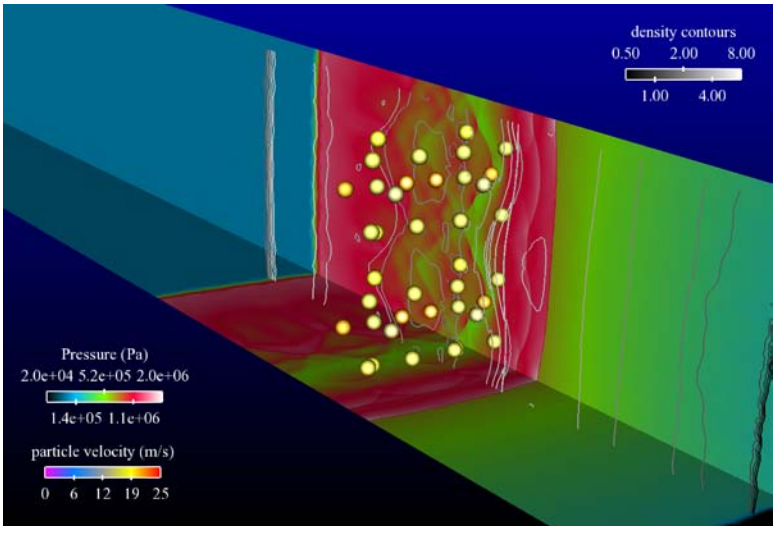

Figure 4.47: Time evolution of blast-particle interaction at 250μs.

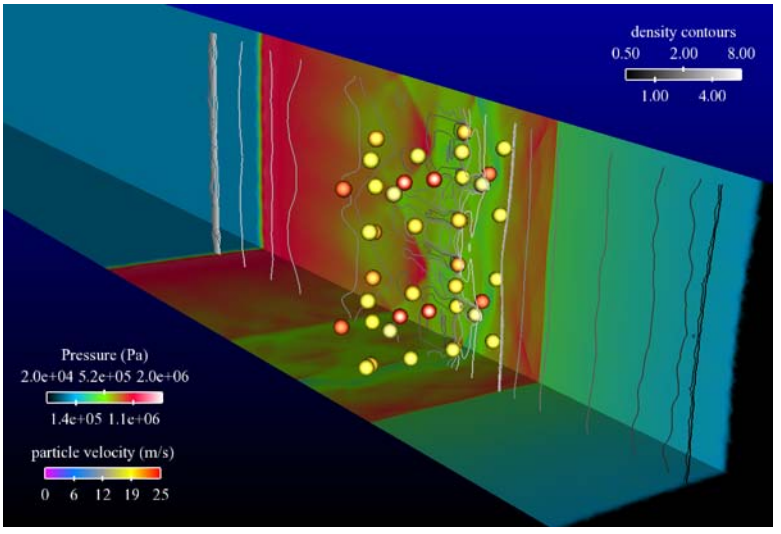

Figure 4.48: Time evolution of blast-particle interaction at 350μs.

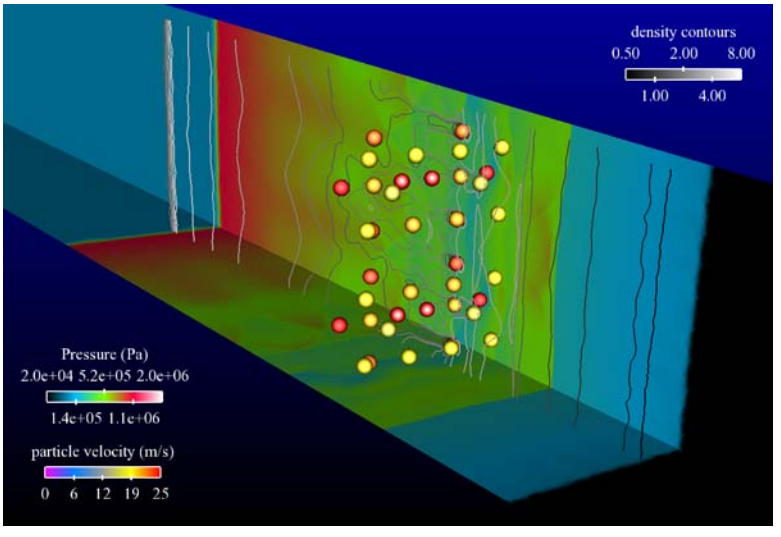

Figure 4.49: Time evolution of blast-particle interaction at 450μs.

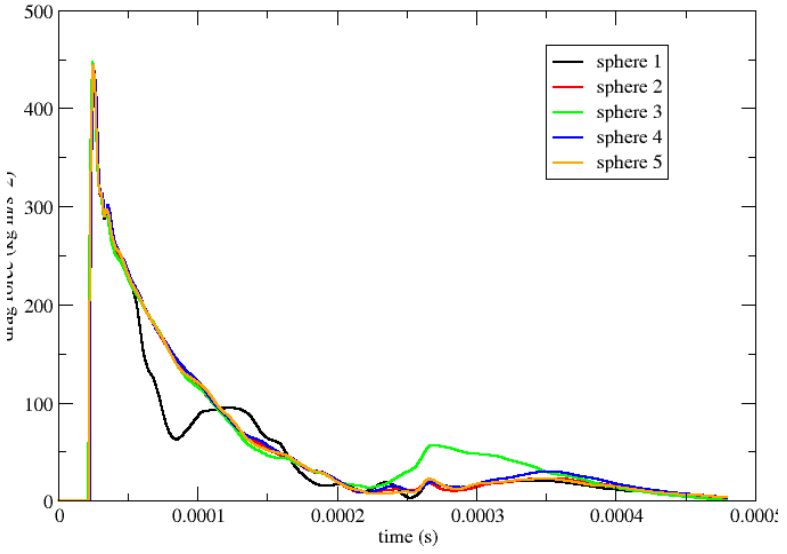

Figure 4.50: Time development of drag on leading plane spheres in blast wave.

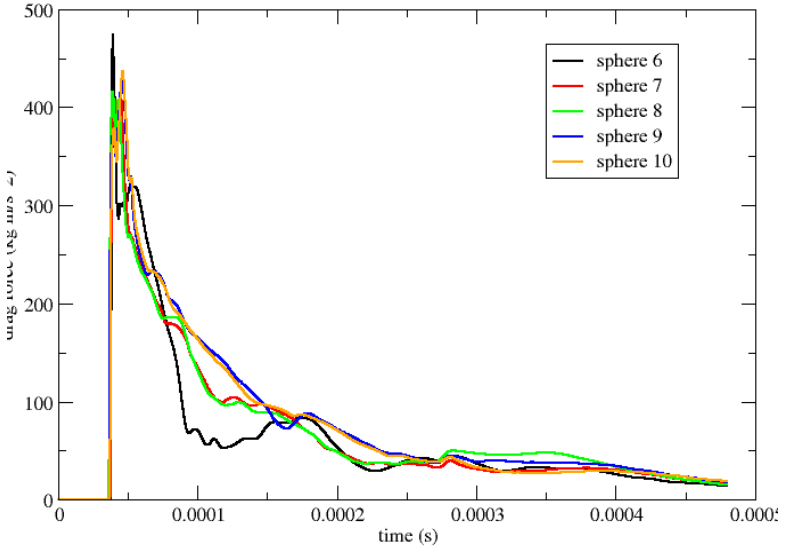

Figure 4.51: Time development of drag on trailing plane spheres in blast wave.

Section 5: Simulation of coupled fluid-structure interactions

A coupled air-blast-wave (shock)-structure interaction analysis capability utilizing Loci/CHEM and LS-DYNA has been developed and demonstrated via the fluid-structure interaction of steel plates for various TNT charge weights. Additionally, loosely-coupled and one-way coupled strategies were examined using a two-dimension blast wave interacting with an elastic circular-arc "bump" geometry.

5.1 Two-dimensional FSI simulations

The software coupling strategies under examination included a loosely coupled ("two-way") methodology and a decoupled (aka "one way") methodology. The loosely coupled approach solved each disciplinary set of equations within its own domain and interfaced the solutions at common boundaries. For this coupling strategy, even when one system had a linear equation set (e.g., linear elastic structural analysis), the problem remained nonlinear. For example, in fluid-structure interaction (FSI) with nonlinear CFD and linear computational structural dynamics (CSD), the external force vector is an implicit function of the displacements. Thus, during each time step, dynamic equilibrium between the systems must be achieved via sub-iterations. However, situations arise when a two-way coupling of the disciplinary physics is deemed unnecessary and neglecting the interaction is considered to be a valid approximation. This situation arises when the deformation of the structure has little impact on the developing blast (that is, when the load duration is much smaller than the response time of the structure) and, hence, a one-way coupling is considered sufficient.

Regardless of coupling strategy, the FSI interdisciplinary transfer algorithm must be utilized for communication between the disciplinary domains, which typically do not have the same discretizations at the common interface. Accuracy of these transfer algorithms may be evaluated by comparing the transferred disciplinary data to those of the matched-mesh solution (that is, same discretization along the interface for both disciplines). To this end, a 2D "testbed" tool has been developed, henceforth referred to as 2DFSI. An effort is underway to assess the accuracy of the in-house non-overlapping point-to-point interdisciplinary data transfer scheme and to investigate the disciplinary coupling strategies (e.g., loose "two-way" coupling, and decoupled or "one-way" coupling). A brief description of the testbed software and preliminary results will be presented and discussed within this report.

Currently, the computer code used to obtain the flow solution in 2DFSI is called NS2D. As the name implies, NS2D is an unsteady implicit 2-D Navier-Stokes flow solver. The code can operate in either a viscous or inviscid mode. The convective flux vectors are discretized using a high-resolution flux-difference-split TVD scheme, and the diffusive flux vectors are discretized using central difference operators. The same software was previously coupled to a heat energy conduction code in an aero-thermal design endeavor [Janus and Newman, 2000]. The motivation and justification for utilizing this software at this stage (rather than Loci/CHEM) are that the code is two-dimensional with fast-turn around times, an adaptation algorithm for the structured grids used for the flow simulation is readily available and easily implemented, and that the dynamic mesh terms and enforcement of the Geometric Conservation Law [Janus, 1989] are already an integral part of the NS2D software. Although different flux formulations and time integration schemes are used within NS2D and Loci/CHEM, for the cases examined here they evaluate the same equation set and produce comparable results.

The initiation of the blast event is characterized by interactions between a planar shock wave, a contact discontinuity, and a fan of rarefaction waves, as shown schematically in Figure 5.1. Although similar to a traditional open-ended shock tube, the origin in Figure 5.1 represents the center line of the high pressure region which acts as a reflection plane for the shock tube scenerio, thus resulting in a blast profile. The distance X_0 is the half-width of the high pressure region (as shown in Figure 5.3). In order to assess the flow solvers ability to simulate the rapid release of energy and the propagation of the blast-wave, ascertain the adequacy of the grid resolution, and compare the NS2D to Loci/CHEM, a rigid "flat" wall, simulation of the aforementioned blast was undertaken. To this end, shown in Figure 5.2 is a comparison of the pressure time history at a point on the plate from the NS2D and Loci/CHEM simulations. As seen, excellent agreement is observed in the positive phase, negative phase, and secondary shock resolution. The slight algorithmic differences between NS2D and CHEM can explain the difference in resolution seen. Further analysis is ongoing regarding establishing an analytical standard by which both solutions can be verified.

The initial case studied was the interaction of a blast wave with a circular-arc "bump" geometry. This case is akin to that utilized by Jaiman et al. [Jaiman et al., 2006] to assess the accuracy of several point-to-element approaches for interdisciplinary data transfer. For a rigid cylinder, this particular case has been numerically studied by Ofengeim and Drikakis [Ofengeim and Drikakis 1997] and exhibits significant unsteady flow and complicated diffraction of shock waves over the cylinder during the blast. Furthermore, as noted in the literature review, for experimental studies with a single or a small number of particles, it has been difficult to arrive at the dependency between the drag coefficient and Reynolds number. Due to refraction, reflection, and diffraction, the geometry and amplitude of the wave fronts are altered due to the interaction of the shock wave(s) with the particle. These interaction effects become significant when large debris/fragments are present.

The geometrical description and initial blast conditions are shown in Figure 5.3; only a half-plane is simulated due to symmetry. Approximate blast profiles of a calculated strength and duration can be created by adjusting the initial high-pressure and temperature within the blast zone and the width of the zone. The magnitude of the blast at impact on the cylinder surface can be adjusted via the blast strength and standoff distance of the blast initiation zone. The conditions shown in this report are for a half-width (x_0) of $0.033L$ centrally located upstream a distance (x_e) of $1.1L$, where L is the distance from the leading-edge point (B) to the trailing-edge point (C). The ambient conditions are set at $p_0=1atm$ and $\rho_0=1.293kg/m^3$. The blast zone initial pressure (stagnation pressure) is set such that $p_3/p_0=33.81$ and the fluid temperatures are uniform. It should be noted that for inviscid flow simulations, the conditions for imposing symmetry and that representing a solid body are equivalent for a planar surface. Thus, the symmetry line could also be viewed as a ground plane. The structured (quadrilateral) grid used for the flow simulation in the upper domain is depicted in Figure 5.4.

Modeling of the solid domain is accomplished with the in-house CSD program originally developed by Newman [Newman 1997], which is an implicit finite-element code that performs nonlinear (geometric and material nonlinearity) static or dynamic analyses and includes numerous element types. For the current simulations, however, only the linear elastic plane stress option for CSD elements is utilized. Furthermore, within this software the Newmark-Beta algorithm is reformulated for the time integration of the nonlinear dynamic response such that it remains consistent with the flow solver during FSI simulations. The matched-mesh structural discretization of the elastic solid in the lower domain is shown in Figure 5.4 along with the CFD mesh. The coupled simulations assume the symmetry line of the fluid domain as a ground plane

and model the lower half as an elastic body under plane stress conditions. The chosen material properties are similar to those used for solid propellants (E=10MPa, v=0.499, ρ=1300kg/m^3). This particular case, albeit having limited physical relevance, represents an excellent scenario by which the FSI interdisciplinary data transfer algorithms may be evaluated. Additionally, it may be used to qualitatively investigate loosely coupled (two-way) and decoupled (one-way) response histories.

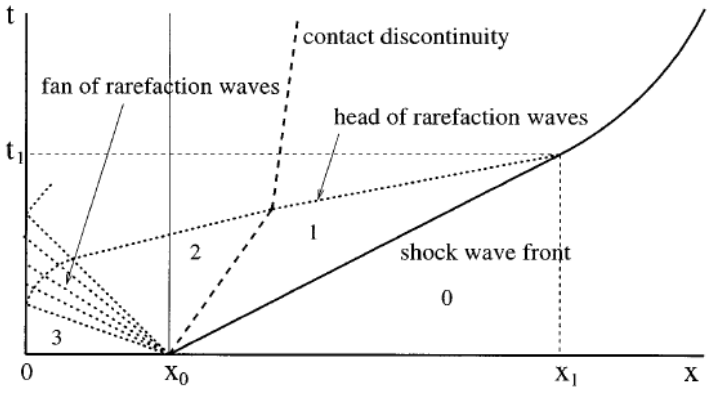

Figure 5.1: Characterization of blast event (x-t diagram) (Ofengeim and Drikakis, 1997).

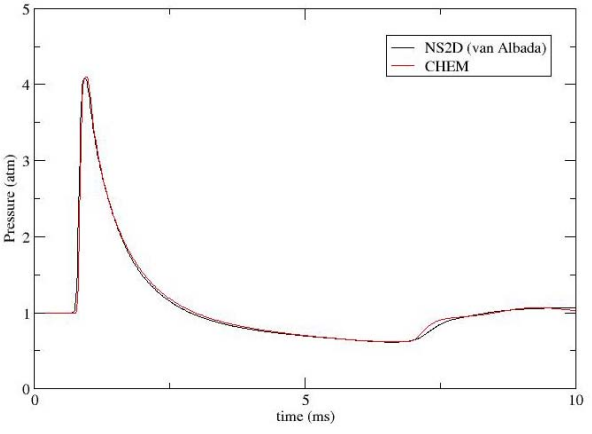

Figure 5.2: Wall pressuure comparison for NS2D vs Loci/CHEM (rigid flat-plate).

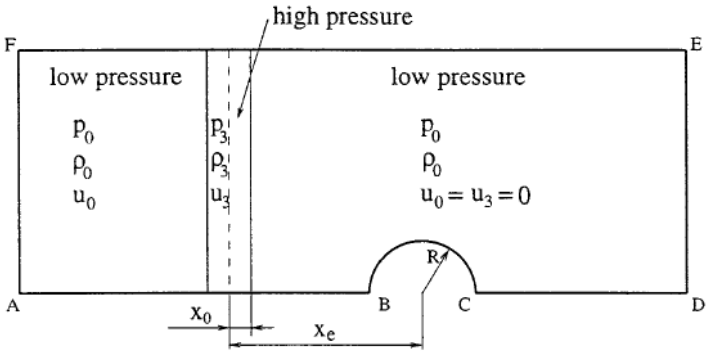

Figure 5.3: Geometry used for blast wave interacting with a cylinder (Ofengeim and Drikakis 1997).

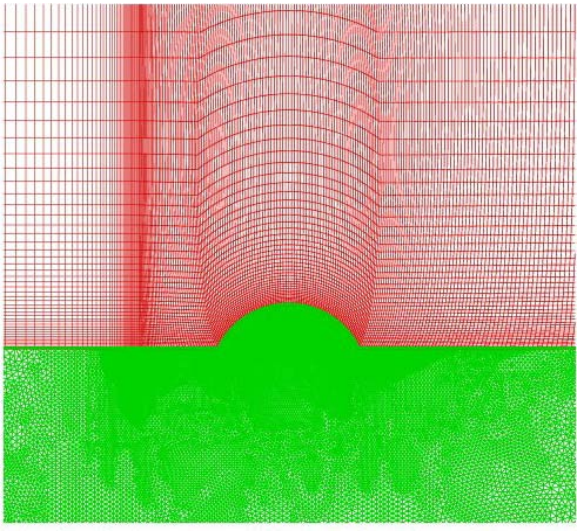

(a) Near-field view of the disciplinary discretizations.

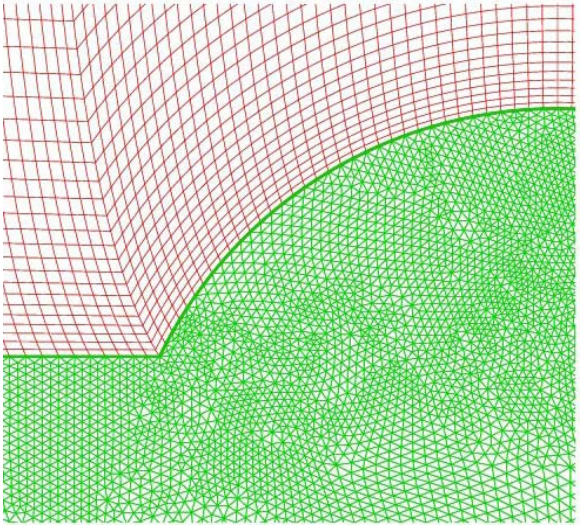

(b) Close-up of the leading edge of the circular arc geometry.

Figure 5.4: CFD (red) and CSD (green) discretizations used for blast-wave/bump FSI.

Initially, the high pressure in the "blast zone" impulsively loads the solid media. This is followed by the evolution and propagation of a blast wave "pressure profile" which impacts the circular arc protrusion. Figure 5.5 depicts the surface pressure distribution at selected times for the (rigid) CFD simulations which are used for the one-way FSI coupling. The *x*-axis represents the horizontal position (measured in meters) along line ABCD in Figure 5.3. The cylindrical surface begins at 0.0 *m* (point B) and ends at 1.0*m* (point C). Here, the pressures from the CFD simulation are transferred directly to the deforming CSD surface but do not alter the blast-wave evolution. Figure 5.6 depicts color-shaded pressure fields for times corresponding to when the blast-wave first reaches the particular points, leading edge (LE), top (TOP), and trailing edge (TE), respectively. Shown in Figure 5.7 are the decoupled pressure and structural response for the (LE), (TOP), and (TE) locations of the circular arc, respectively. For this one-way coupling, significant structural response only occurs once the blast wave reaches each location. This slow response time is illustrated clearly in Figure 5.8 as the blast-wave reaches the leading edge of the circular arc. A comparison of surface pressures for one-way and two-way coupling, as shown in Figure 5.9, also indicates that the surface deformations have little influence on the blast-wave for the conditions chosen for this demonstration.

The two-dimensional test case presented was selected because it sufficiently represents the physical phenomena found in a blast event. Furthermore, an elastic body was chosen such that the structural response would have the ability to interact with the resulting blast waves propagating over and impacting an obstacle. The decoupled (one-way) and loosely coupled (two-way) methodologies where both simulated and compared numerically. Based on these simulations, , the structural response for the selected elastic body selected was slow compared to the blast event and only local deformations were present that did not significantly alter the wave evolution. These preliminary findings are consistent with observations concerning blast-wave (shock)-structure interaction found in the literature. This would not be the case for thin structures such as shells which would have faster response times and thus have large non-local deflections and changes in surface curvature. The development of the 2DFSI will enable a better understanding of limitations of the one-way coupling approach.

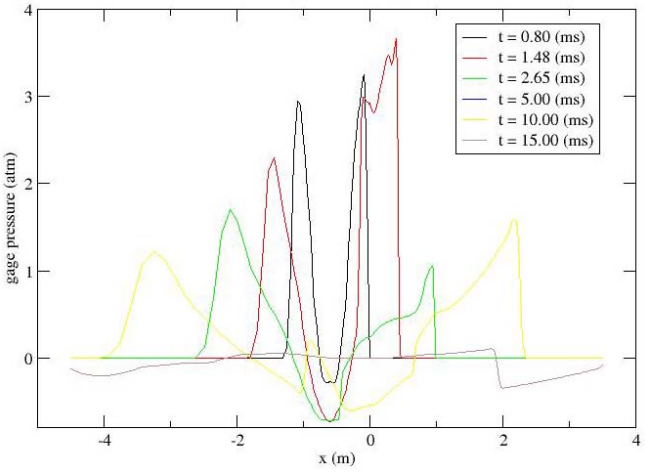

Figure 5.5: Surface pressure distribution at selected times for decoupled (one-way) simulation of a blast-wave/bump FSI interaction.

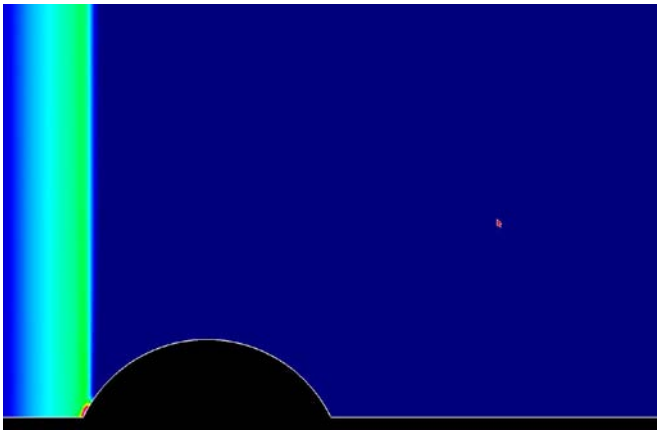

(a) LE impact, t ~ 0.8*ms*.

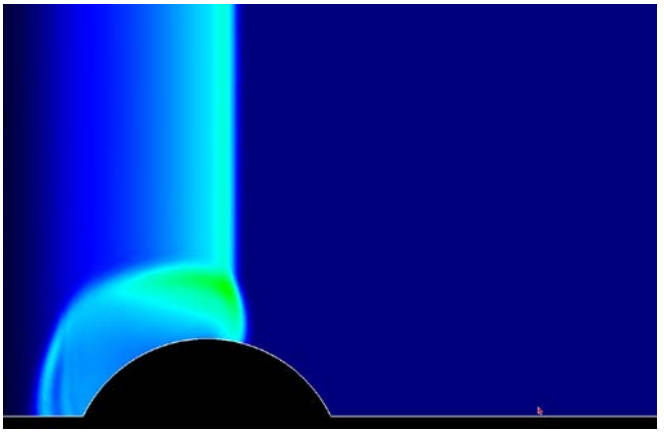

(b) TOP impact, t ~ 1.48*ms*.

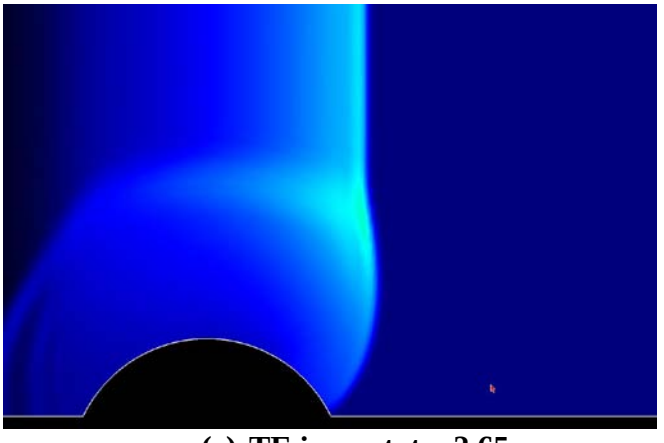

(c) TE impact, t ~ 2.65*ms*.

Figure 5.6: Shaded-surface pressure plots of blast-wave/bump interaction.

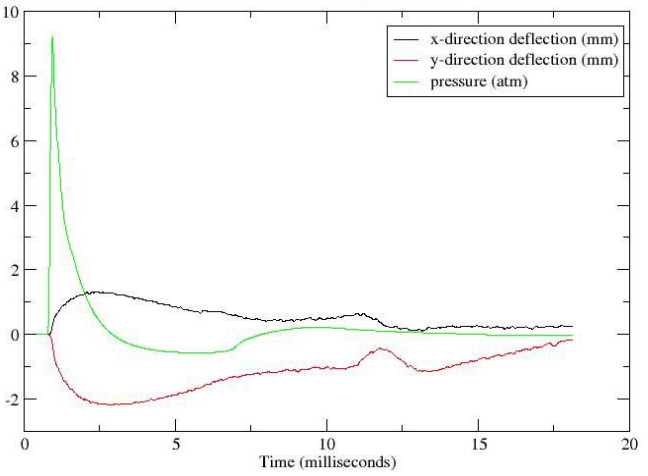

(a) Surface pressure and deflections at the LE.

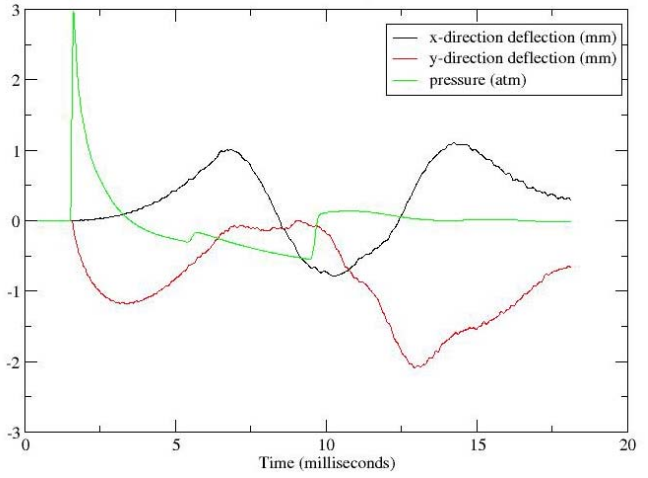

(b) Surface pressure and deflections at the TOP.

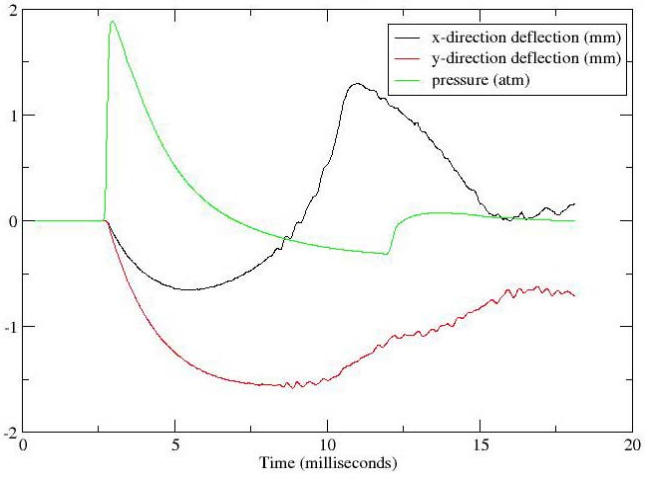

(c) Surface pressure and deflections at the TE.

Figure 5.7: Surface pressure and deflections for decoupled (one-way) simulation of a blast-wave/bump interaction.

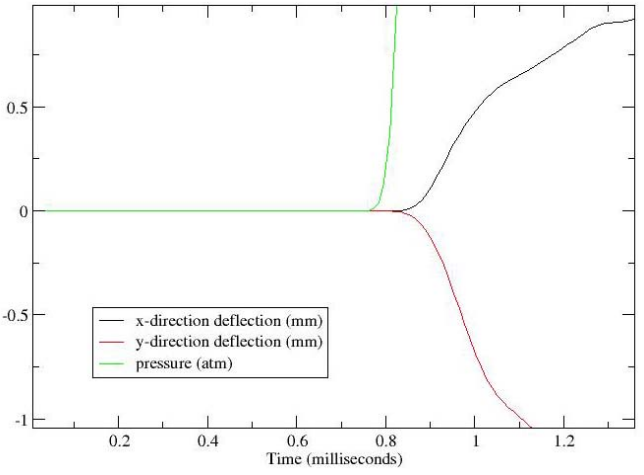

Figure 5.8: Close-up view of LE surface response for decoupled (one-way) simulation.

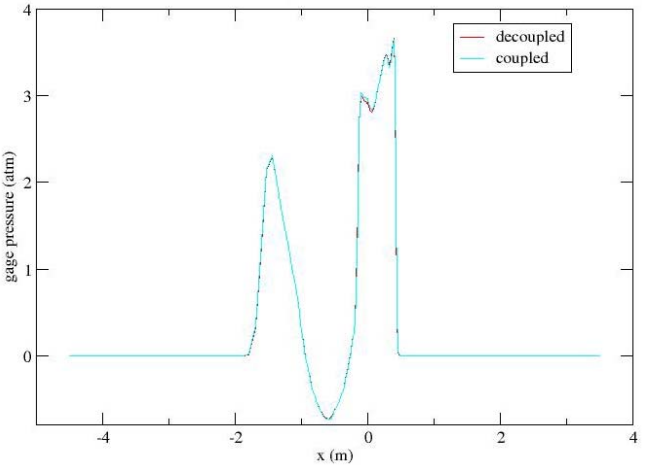

Figure 5.9: Surface pressures: one-way vs two-way coupling, t ~ 1.48ms.

5.2 Three-dimensional blast-plate FSI simulation

An exemplary experimental setup, by which preliminary evaluation and validation of the developed technology may be made, has been presented by Trzcinski and Cudzilo [Trzcinski and Cudzilo, 2004]. Their study presented experimental results of air blast waves generated by cylindrical TNT charges of various weights as they impacted steel and laminated fabric plates. The rectangular plate, having a side length of 0.5 *m*, was clamped along the edges as shown in Figure 5.10. The loaded portion of the plate has a side length of 0.46*m*, and all plates have a thickness of 1*mm*. Experimental plate profile final shapes were recorded for three TNT charges (50g, 75g, and 100g).

For the three dimensional fluid-structure interaction simulations, Loci/CHEM was used with the HLLE inviscid flux, the Barth flux limiter, and Runge-Kutta second-order time integration. A maximum CFL of 0.9 was implemented throughout the runs. Although the charge shape was indicated to be cylindrical (as in a "circular" cylinder), no specific dimensions were given in the report. In the simulation, the charge was chosen as a circular cylinder of overall square dimensions, i.e. cylinder height is equal to the cylinder diameter. For computational brevity, the axisymmetry (about the vertical axis) of the cylindrical charge was exploited in addition to the quarter plane symmetry of the entire experimental configuration. In figure 5.11, the computational geometry and mesh cut-planes for this configuration are shown with half–plane symmetry.

The solution process involved performing an axisymmetric simulation of the charge detonation on a uniform mesh. The axisymmetric mesh, the yellow mesh nearest the charge in Figure 5.11, has an order of magnitude in higher resolution (~0.5*mm* mesh spacing) than the fully 3D mesh in the same region. The charge detonation was initiated at the center of the base of the charge, and the axisymmetric simulation was executed for ~0.05*ms*. Limiting the simulation to such a short time was done to ensure that the ambient outer-boundary condition was not disturbed. The solution was then interpolated to the computational domain of the fully 3D simulation. The solution was continued for an additional 2*ms*.

The 50g solutions shown in Figure 5.12 are of the $\log_{10}$ of the pressure at various times during the blast simulation. Figure 5.12(a) illustratessoon after the solution was interpolated from the axisymmetric detonation simulation. Figure 5.12(b) shows the initial impact of the blast wave with the plate surface. Although the view is from above, the surface pressures on the bottom of the plate are depicted in the figure. Figure 5.12(c) is a view from below the plate illustrating the reflected blast wave (shown in the colored-mesh symmetry plane). Depicted in Figure 5.12(e) is the pressure at the time (~0.5*ms*) where the total vertical force acting on the plate is balanced. The total vertical force acting on the plate over the entire time history of the simulations for each charge weight is shown in Figure 5.13. As seen, at approximately 0.5*ms*, the total pressure force begins to act downwards before returning to atmospheric. Since the blast evolution is similar for the 75g and 100g TNT, pressure plots are not shown for brevity.

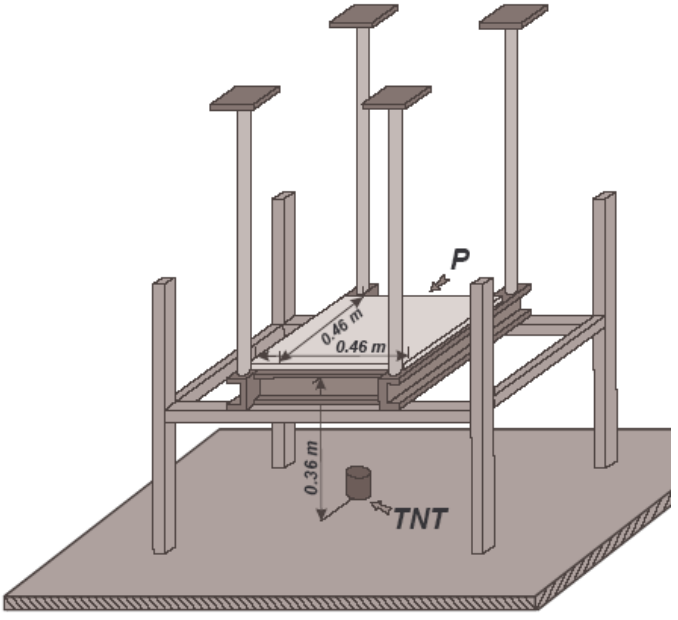

Figure 5.10: Experimental apparatus for blast loading on plates from [Trzcinski and Cudzilo 2004].

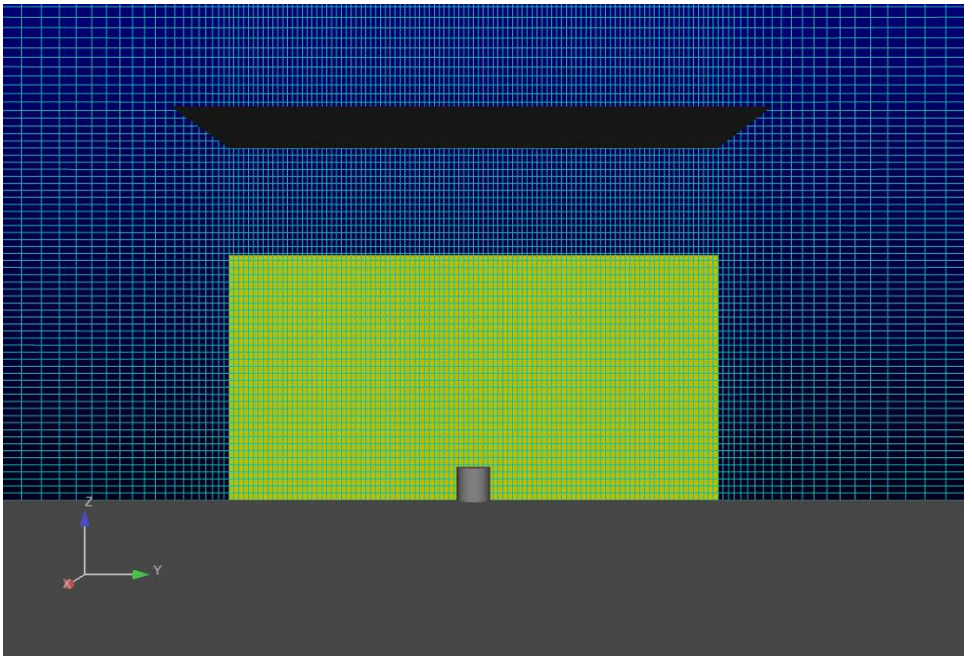

Figure 5.11: Blast/plate computational geometry (50g TNT cylindrical charge).

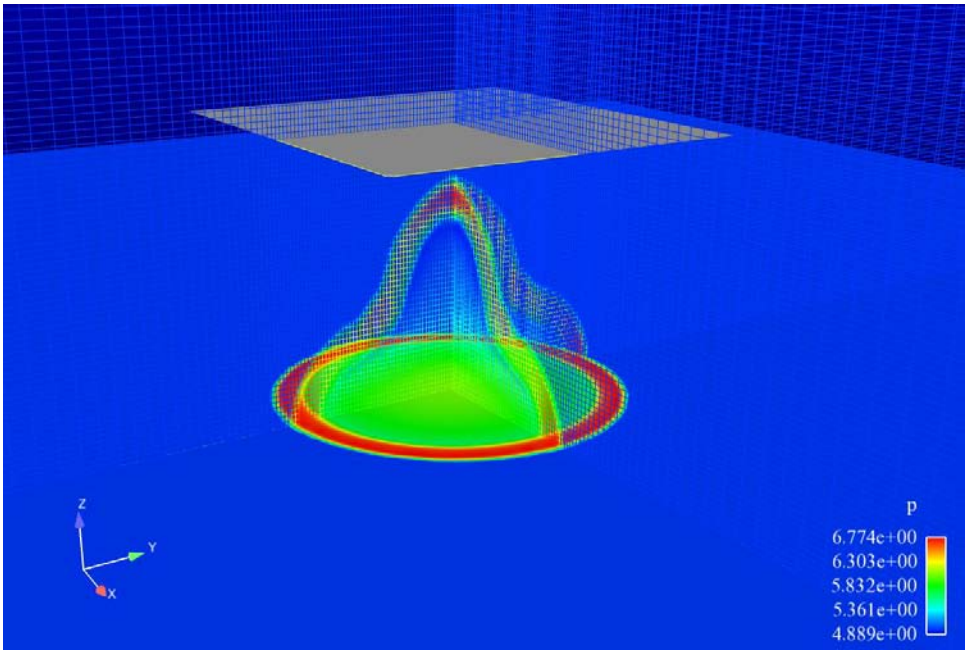

(a) t~0.06ms (view from above plate).

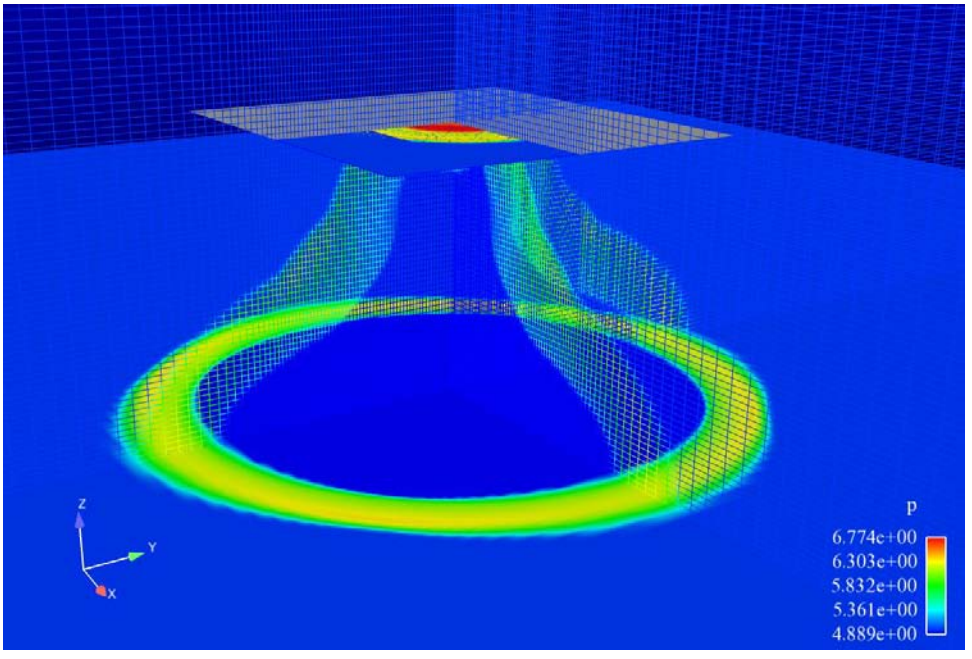

(b) t~0.15ms (view from above plate).

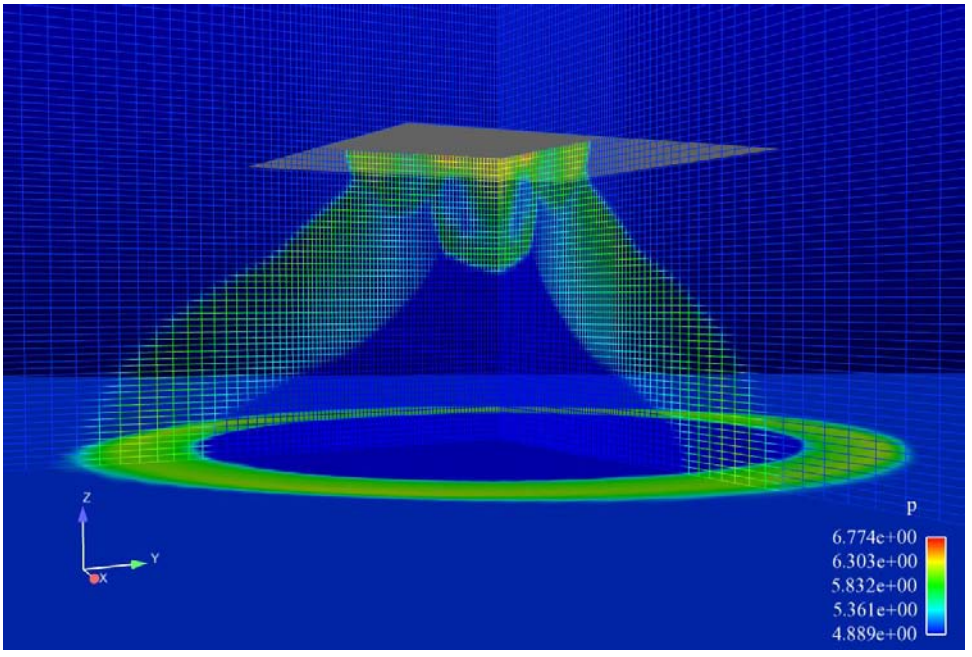

(c) t~0.2ms (view from under plate).

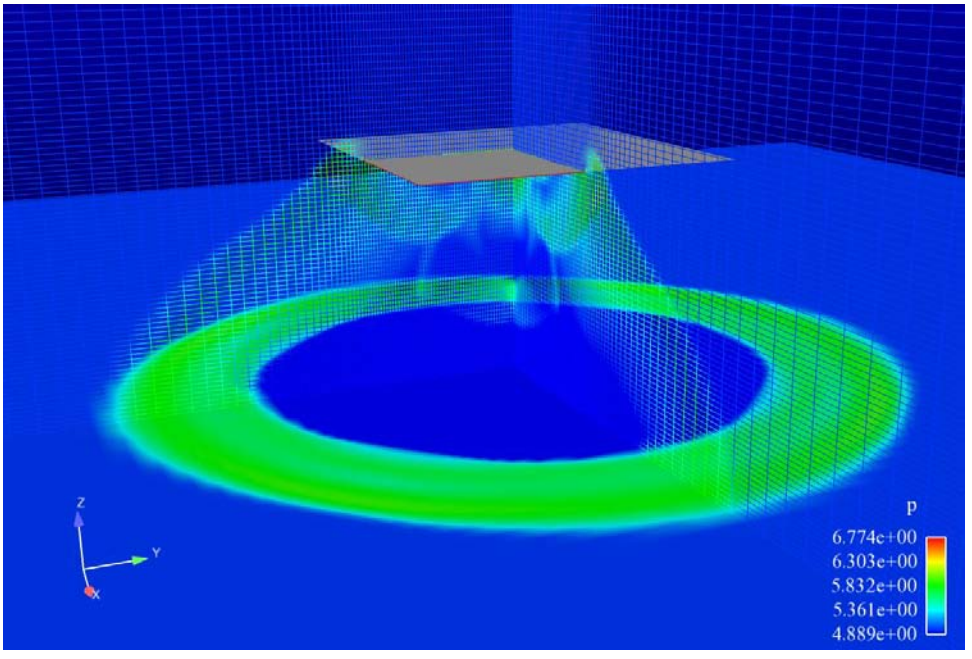

(d) t~0.3ms (view from above plate).

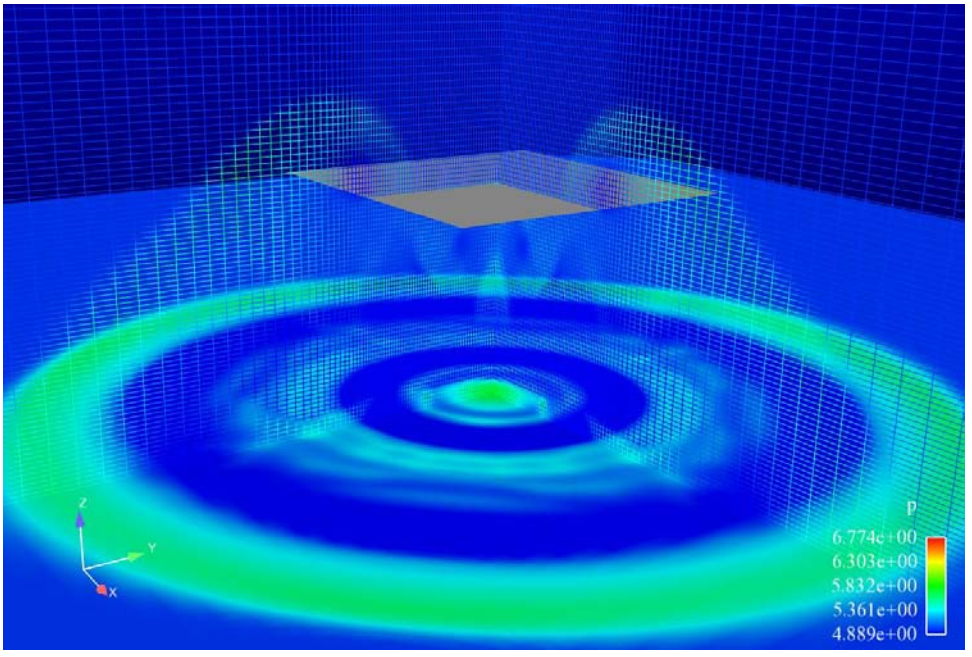

(e) t~0.5ms (view from above plate).

Figure 5.12: Computational solution for 50g TNT.

The plate surface nodes and pressure loads from the Loci/CHEM simulations were converted into a LS-DYNA input file using a developed utility program. This program reads in the extracted data at the user defined time intervals and then creates the appropriate NODE, ELEMENT_SHELL, LOAD_SEGMENT and DEFINE_CURVE cards and inserts them within the input file. The one-way coupled simulations for the current configuration used matched meshes between the fluid and the plate structure. However, the utility can easily be used to convert data for nested, non-matched meshes. The rectangular plate was discretized with 2500 four-noded Belytschko-Tsay shell elements with 5-point through thickness integration. The steel plate is modelled using the plastic-kinematic material option (MAT_003) with isotropic hardening and assumed to be strain-rate insensitive (average strain rates encountered were 50 s^{-1}). The following properties for steel are used: density ρ = 7800 kg/m^3, elastic modulus E = 196 GPa, tangent modulus E_p = 0.2 GPa, Poisson ratio ν = 0.3, and initial yield stress σ_y = 175 MPa. The same properties were utilized by Adamik et al. [Adamik et al., 2004] in a LS-DYNA simulation of this experiment.

Shown in Figure 5.14 are the final steel plate center line deflections for the 50g, 75g, and 100g TNT charges from the experiment of Trzcinski and Cudzilo, the LS-DYNA simulations of Adamik et al., and the present one-way coupling of Loci/CHEM and LS-DYNA. As seen, good agreement with the experiment is observed. The lack of agreement in the 50g TNT case in Figure 5.14a is most likely attributable to imperfections in the experiment. It is obvious that the final deflections in the experiment were not symmetric, whereas for the 75g and 100g TNT cases they were. As noted in Adamik et al., one possible imperfection may be due to plate clamping, and it was found during simulations that varying the boundary condition treatment at the clamped edges had a significant impact on the plate deflections. Although good agreement is observed, the need

for two-way coupling may be justified as the charge weight is increased. This is evident in Figure 5.14c near the plate center where drastic increases in deflection take place.

As a final note, the results from the experiment are comparable to the LS-DYNA simulation of Adamik et al.; however, Adamik et al. discussed the challenge of creating an initial mesh that did not require mesh rezoning and the need to perform the simulation in distinct phases. The need for these phases were primarily driven by numerical problems associated with remote regions (charge and contact air zone) as the simulation proceeded. Adamik et al. summarized that LS-DYNA is a powerful tool for simulating such blast events, but they conceded that considerable expertise is required in its application. On the other hand, the one-way coupling between Loci/CHEM and LS-DYNA was easily implemented for this blast wave fluid-structure interaction.

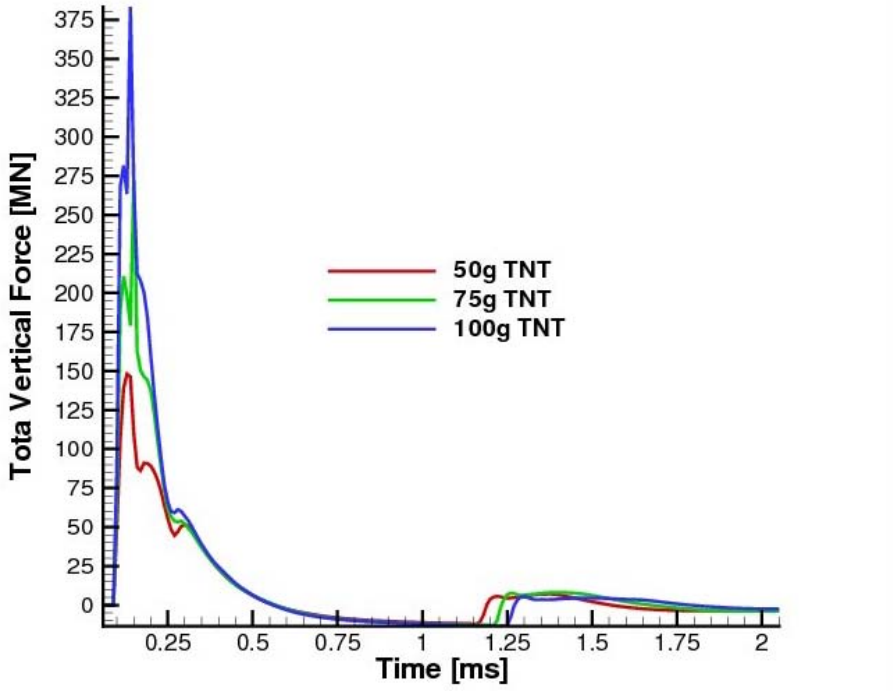

Figure 5.13: Vertical force histories for the 50g, 75g, and 100g TNT charges.

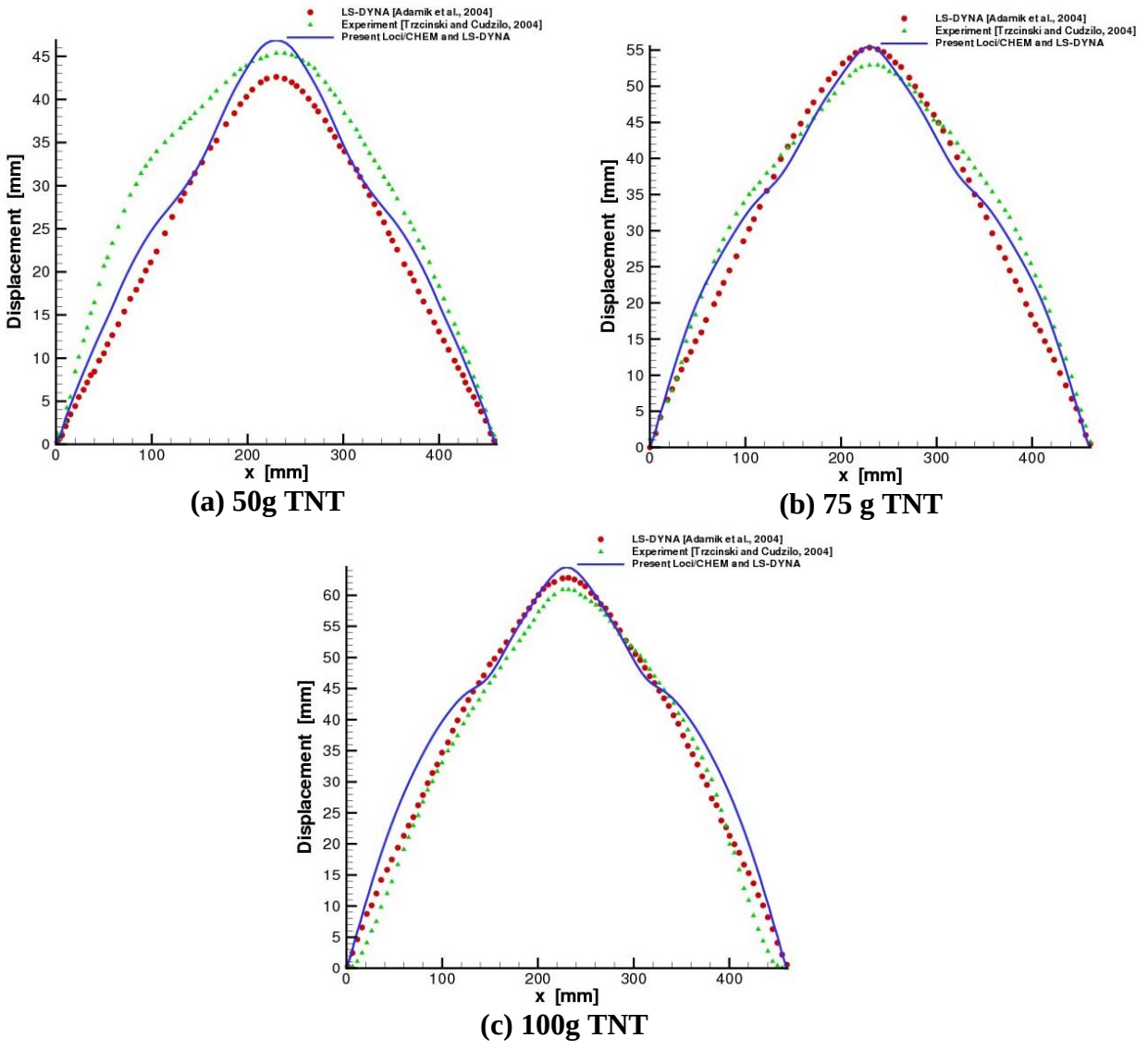

Figure 5.14: Centerline steel plate profile for different charges.

Although no experimental data existed, the current blast-plate was utilized to ascertain the influence of an explosive event from a buried charge. To this end, a 50g TNT charge was placed in soil (dry sand) at the same standoff distance beneath the steel plate previously discussed. The soil had a total depth of 0.15 m, and sat upon a rigid base (reflection plane). The depth of burial was approximately 15 mm beneath the top soil surface. All other parameters remained the same as the 50g TNT air-blast simulation. The total vertical force acting on the plate for both the 50g TNT air-blast and for the soil-blast are shown in Figure 5.15. Here, the soil confines the blast wave and thus the arrival time is significantly delayed. Furthermore, it appears in Figure 5.15 that the blast wave of the gas arrives at a lower pressure, followed by the subsequent impacting of the soil. As seen, the soil imparts a much greater loading on the plate. The combined effect of the gas and soil acts on the plate for a much longer duration. However, the secondary wave (due to reflections within the initial blasting process) appears to impact the plate at approximately the

same time as the air-only blast (~1.2 ms). Figure 5.16a depicts the initial impact of the blast wave, soil and JWL gas on the plate, illustrating the containing and focusing effects the soil imparted to the blast process. Figure 5.16b depicts the final stages of the blast interaction with the plate, illustrating the dispersal of the blast products. The ultimate result of simulating this blast in soil is shown in Figure 5.17 for the final steel plate center-line deflections. This figure demonstrates that the inclusion of soil causes the blast to extend over a much larger portion of the plate, as opposed to localized central deflections seen for the air-blast. Additionally, the final central point deflection is actually greater than those of the 75g TNT air-blast (i.e., 50% more explosive).

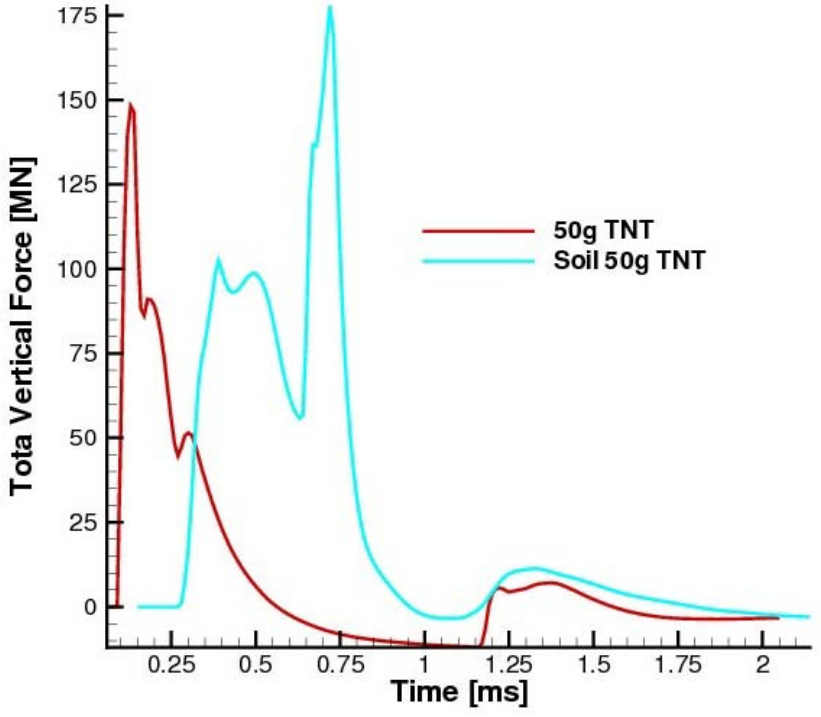

Figure 5.15: Vertical force histories for the 50g TNT charges in air and soil.

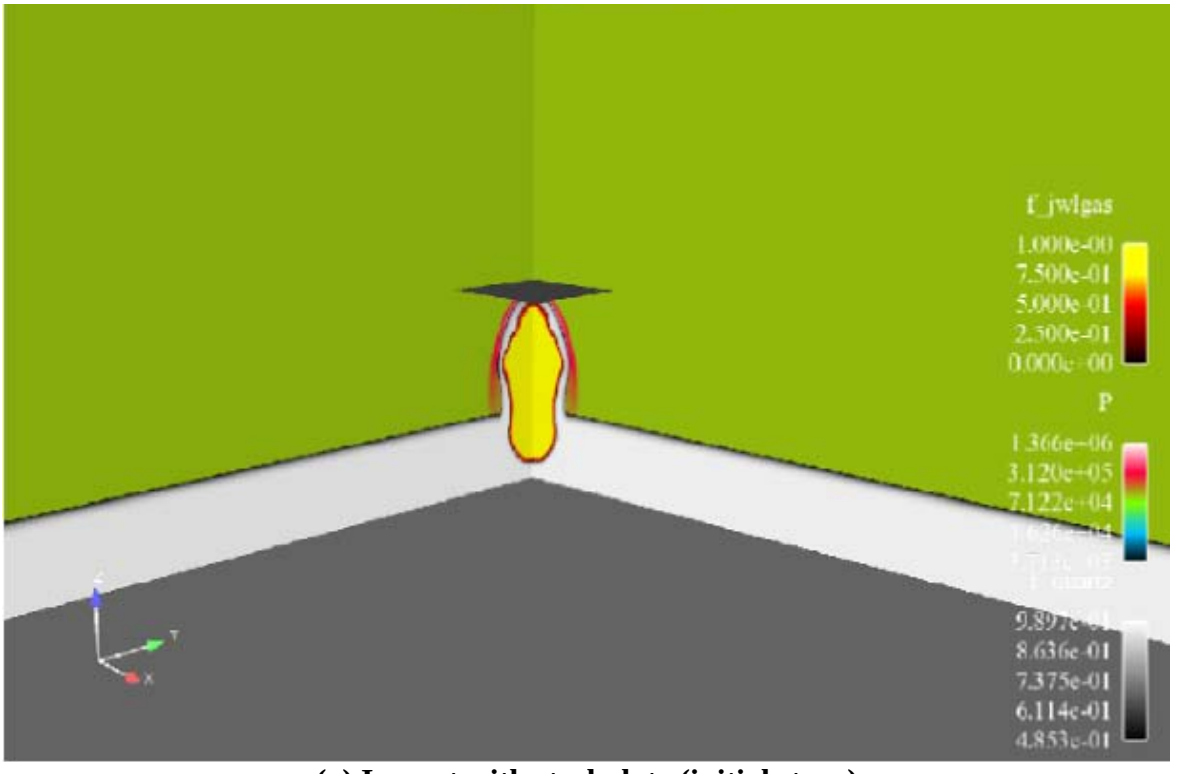

(a) Impact with steel plate (initial stage)

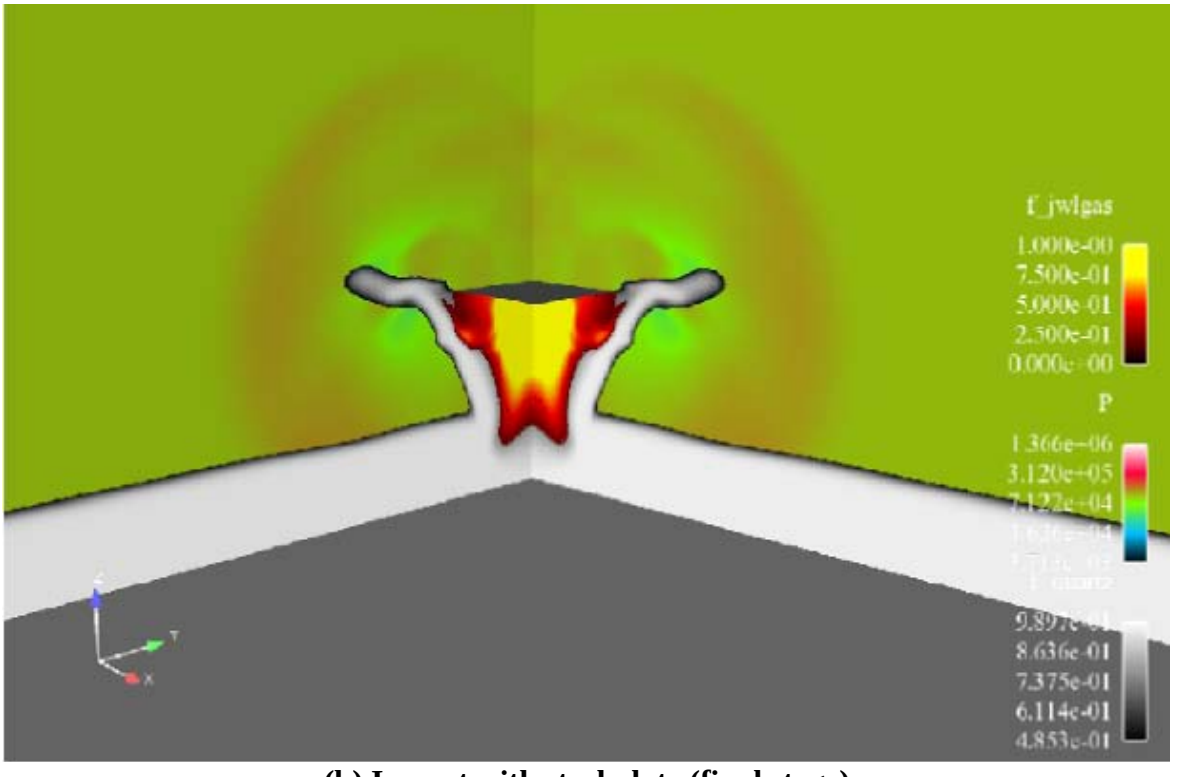

(b) Impact with steel plate (final stage)

Figure 5.16: Computational solutions for the 50g TNT charge in soil (dry sand).

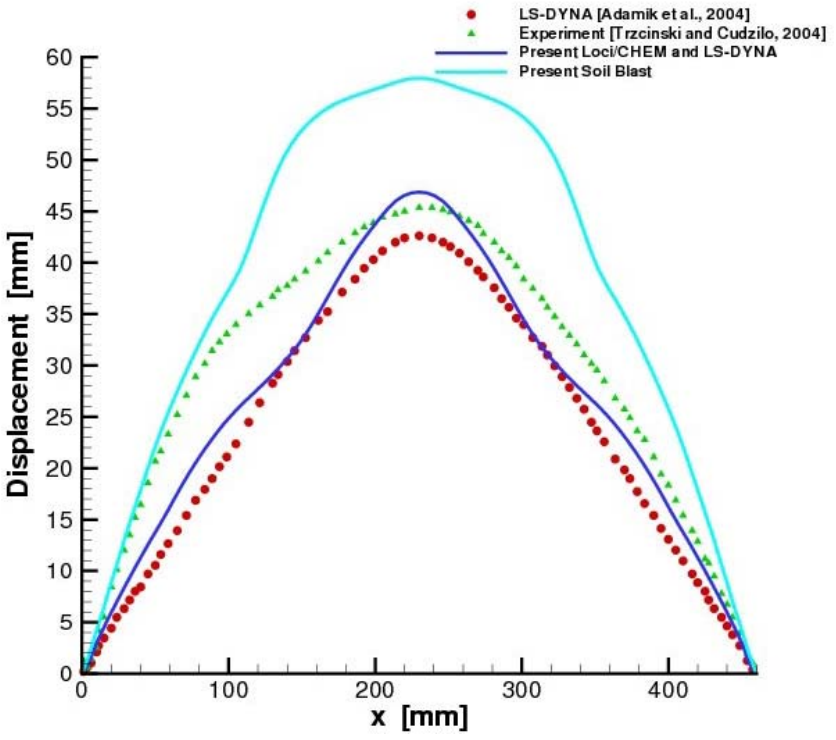

Figure 5.17: Centerline steel plate profile for 50g TNT charges in air and soil.

Section 6: Strategy for simulating blast-vehicle interactions for complex geometries

Modeling the blast-soil interaction problem is a particularly challenging problem due to many factors. Physically, soil can be considered as a three phase mixture composed of liquid (water), gas (air), and solids (quartz, organic matter, etc.). When considering the properties of a soil under a high strain-rate event such as explosive blast, the soil behavior will be significantly different than in low strain-rate events. For example, in typical soil tests, the liquids and gases trapped in the pores of the soil will be free to migrate and so will become part of the measured material strength under typical experimental compression and shear tests. Under high strain-rate events, however, the liquid and gas are trapped in the material pores and do not have sufficient time to migrate through the material. Thus, for explosive events, modeling the soil as a mixture equation-of-state for the constituent components of the three phase material provides a sound starting point for developing a suitable soil model.

In the interaction between the soil and the expanding explosive gases, there are two main regimes: compression and tension. In the initial stages of the explosive/soil interaction, the soil is essentially behaving as a fluid undergoing severe deformation. Our present simulations for shallow buried mines seem to confirm this with very good crater width comparisons for early times in the explosive event. As time proceeds and with increasing depth of burial, we find that the role of strength begins to play a greater role, as evidenced by over-predictions of crater widths at later times in our fluid based simulations. However, the most significant challenge in characterizing the behavior of soil is to differentiate its response to tension in high strain-rate events. Under tension, soil can readily loose cohesion and become an aggregate particulate cloud of soil particles and soil clumps. The effect of water in the soil must also be accounted for in the model. Under compression, water is relatively well-characterized by equations of state such as the Tait EoS used in the presently reported simulations. Water can undergo violent phase change (cavitation) under low pressures. These low pressure conditions are more likely to be found in high moisture content soils where the strength of the relief wave caused by the reflection of the blast wave off of the soil-air surface can produce very low pressures. Similarly, on the outer edge of the crater, expansion waves can produce very low pressures. For most soils these low pressures will likely lead to water cavitation causing soil failure. However, unlike simple tearing of the soil, cavitation is more likely to produce a dense cloud of small particulates that are highly energized by the expanding water vapor. The present models that were used in this study and those that were described in the literature do not model the effects of cavitation of the water contained within the soil.

Understanding the mechanism of soil failure and its subsequent transition to a multiphase particulate laden flow is key to modeling blast soil interactions with physical reality. There are primarily two mechanisms that the soil plays in the blast loading: 1) confinement and focusing effects, and 2) impulse augmentation due to solid particle impact loading. The accurate modeling of both of these effects requires an accurate modeling of the transition from a continuum treatment of the soil before failure to a multiphase treatment of the soil after failure. We note that the efficiency of momentum transfer between the soil and the expanding explosive gases is most efficient when the soil fully contains the explosive gas. As the soil fails, the explosive gases will quickly pass around the soil particles to the surrounding ambient atmosphere. Correctly modeling this process will have a major effect on the partition of blast energy that is deposited to the resulting particulate cloud and the amount of blast energy that remains in the expanding air blast.

This partitioning of energy is controlled by the timing of the failure of the soil and the subsequent expansion of the debris cloud. Based on our studies, once the soil becomes free particulates, the coupling between the explosive gases will be dominated by inviscid and volume fraction effects. In regions of large particle volume fraction gradients, significant momentum transfer can occur between the particles and the expanding gases. In addition, when relative velocities are very large, inviscid effects are dominant. However, based on our studies, viscous effects can be safely neglected for particles that are sand grain-sized or larger. As a result, the distribution of particle sizes will likely play only a small role in the accurate prediction of blast loads.

Once the soil has failed and become a dispersed phase cloud of particles, accurately modeling the transfer of momentum from the expanding cloud of detonation products will be essential to accurately modeling the vehicle blast loading. In part, this is due to the particles being more effective at transferring momentum to the solid surface than to a gas. In the momentum transfer to the particles, there will be three major terms: 1) viscous drag, 2) inviscid wave drag (Mach number corrections), and 3) pressure action due to gradients in volume fractions. The momentum transfer to the particulate phase will either be coherent (all in the same general direction) or randomly distributed. The random distribution will contribute to the granular temperature of the particulate cloud, while the coherent transfer will contribute to the bulk motion. Correctly modeling the balance between these two forms of momentum transfer will play an important role in predicting the distribution of particle trajectories that emanate from the blast crater.

In terms of the physical models, a key concern for modeling the blast-soil interaction accurately will be correctly modeling the process of soil failure and subsequent transfer to a dispersed phase model. Since the solid soil material will be very effective at transferring impulse to the vehicle, the timing of this failure will be critical to accurately predicting blast loading: A transition that is too early will under-predict the transfer of momentum to the particulates, while one that is too late will result in excessive particle velocities and a subsequent over-prediction of blast loading. Immediately after failure, the large volume fractions and high pressure gradients will yield a strong but abating momentum coupling between the gas and particulate phases. Currently, the main challenge with creating such a model will be determining the appropriate phenomenological models for soil failure, the initial energy partition between soil and gas upon failure, the energy partition between coherent kinetic motion of the particles and random particle motion represented by a granular temperature, and finally the model for the momentum coupling between the dispersed and gas phases after soil failure is complete.

6.1 Numerical modeling of soil-blast interactions

For numerical models of the blast soil interaction we have essentially three candidate methodologies: 1) Lagrangian methods, 2) Eulerian methods, or 3) meshless methods. Lagrangian methods simulate material deformations directly by tracking the deformation of the material with the simulation mesh. These methods are usually based on a finite-element formulation and are robust and efficient methods for computing the deformation of solids. For highly plastic or fluid flow problems, they are subject to mesh tangling issues that can cause accuracy and robustness problems. In the case of soil in close proximity to an explosive event, the soil undergoes, for a period of time, severe deformations that can present challenges for a Lagrangian method. In addition, the simulation of the soil using a Lagrangian method will require some sort of fluid-structure-interaction to account for the interaction of the soil with the expanding explosive gases.

An alternative to Lagrangian methods are Eulerian methods that keep the mesh fixed and allow material to move through the mesh. These methods can be implemented using either finite-element or finite-volume formulations and solve the mesh tangling issue. In addition, it is possible to formulate an Eulerian solver such that the soil and explosive are treated in one unified model whereby issues such as conservation of mass, energy, and momentum are trivially satisfied. One downside of the Eulerian techniques is that they have less fidelity in capturing material interface dynamics. However, for blast-soil interactions, the soil interface is unlikely to remain sharply defined, and so such a compromise is reasonable.

A third method that can be highly robust for simulating dynamically evolving interfaces are meshless methods such as Smooth Particle Hydrodynamics (SPH). In these methods, the material is represented by a collection of "particles" that can evolve in time. Particles interact through the use of interpolation functions that average particles within a given smoothing length (which can be adjusted based on local particle densities). It should be noted that such a scheme is still a continuum simulation whereby the "particles" do not actually represent particulates as found in a multiphase flow, but rather are artifacts of this numerical discretization methodology: the underlying numerical model is still solving equations of continuum mechanics. These SPH methods are more expensive than either Lagrangian or Eulerian methods and may provide a more natural way to transition from a continuum to multiphase representation. However, it would seem that the cost of these methods are not justified, as we can always combine the Lagrangian or Eulerian methods with multiphase models which do not require the expensive smoothing function and thus would be much more efficient. We would note that recent work in combining Lagrangian and SPH methods [Johnson et al., 2008] show the potential richness of using SPH to couple soil and blast simulations. We do note that while this paper does use SPH particles to improve robustness of Lagrangian methods, they do not consider the soil transition to a multiphase flow problem.

The modeling capabilities that have been developed thus far include an Eulerian finite-volume solver that is fully conservative for the simulation of blast-soil interactions. This model currently does not include material strength models, nor does it consider the failure of the soil and the subsequent transition to accurate multiphase models. In order to improve the modeling of blast loads due buried explosive devices, we suggest that our current model should be extended to include material strength. In addition we need to extend our present model such that we couple soil failure to a multiphase model of the resulting debris cloud.

Once the basic model is in place that can accurately capture the blast-soil interaction and the multiphase debris cloud, the next important focus is to determine the appropriate model for soil failure: What are the mechanisms for soil failure? What role does cavitation play in soil failure? How should cavitation be modeled? When failure happens, how important is capturing the transfer of energy to the granular kinetic energy of the particulate cloud? How is this partition of blast energies accurately modeled?

6.2 Numerical modeling of blast-structural interactions

The accurate, robust, and efficient simulation of fluid-structural interactions for complex geometries involving even modest physical models represents a significant challenge as well. The phenomena associated with explosive events, and the resulting interactions between the various materials and states, along with the potential for fragmentation and fracture, make this task even more daunting. This problem becomes more tractable when high-fidelity simulations codes are available to model the relevant physics associated with the various disciplinary domains, and then

compatibility/equilibrium is enforced at the interfacial boundaries. However, enforcement of this compatibility represents yet another challenge towards accuracy, robustness and efficiency. To this end, numerous methods have been developed and devised to tackle these issues, with each having specific advantages and disadvantages. Although a comprehensive review of these methods will not be presented within this report, some of the various attributes shall be discussed. Furthermore, many common features exist between modeling the soil-blast and the blast-structural interactions, and can possibly be exploited. These discussions shall put into context the candidate methodologies for simulating blast-vehicle interactions using Loci/CHEM and LS-DYNA.

As presented in Section 6.1 for soil-blast interactions, it is well known that when using a purely Lagrangian approach that mesh tangling becomes a significant issue when large deformations are encountered and create the need for costly remeshing, potential introduction of errors, and lack of robustness when dealing with topological changes. In Eulerian approaches numerical diffusion (due to advection of the solid stress or strain) may result in substantial inaccuracies and additionally has the burden of locating material interfaces. Many techniques have been developed in an attempt to mitigate these deficiencies for specific problem classes. One such approach, for example, is the material point method (MPM) extended for multiphase flows [Zhang et al., 2008]. That technique was developed to use both an Eulerian mesh and Lagrangian material points. The velocity of each phase is computed on the Eulerian mesh, thus eliminating mesh tangling problems. The deformation (and thus stress history) of the material points are tracked by the Lagrangian nodes. That particular method avoids most of the pitfalls associated with the Eulerian and Lagrangian formulations, but retains their respective advantages. However, the computational costs are higher and there is need to interpolate information between the mesh nodes and material points at each time step. Additionally, this method suffers from errors (particularly at sharp interfaces) due to the inability to satisfy the continuity equation in terms of the volume fractions identically, and is only satisfied in the sense of a weak solution.

At this point, the issue related to transition within the soil-blast interaction and the blast-structural interactions becomes more apparent. In the early stages of the soil-blast evolution, a continuous multiphase flow is appropriate to model the large fragments associated with the interaction. As the soil breaks apart into smaller fragments, it transitions to a dispersed multiphase flow. For the fluid-vehicle structure interaction, the simulation is similar to that of the early stages of the soil-blast model, and may be represented with the same continuous multiphase flow approximation.

As is apparent from the discussions thus far, we wish to develop a method that avoids the pitfalls of the various approaches, may be readily implemented within Loci/CHEM, and is ultimately two-way coupled with LS-DYNA. Although many details require further research, one candidate methodology is to use Loci/CHEM as an Eulerian predictor followed by using LS-DYNA as a Lagrangian corrector step. For such an algorithm, implementation of a strength model into Loci/CHEM would be required. However, development of strength models in the context of a Godunov type solver similar to the algorithm employed within Loci/CHEM has been developed [Miller and Colella, 2001]. Miller and Colella reformulate the equations of solid mechanics as a first-order system of hyperbolic equations and solve the system via an explicit second-order Godunov method. In particular that solution algorithm is a predictor-corrector scheme that solves the conservative fluxes representing elastic flow as the predictor followed by a corrector step accounting for plasticity within a source term. This method conserves mass, momentum, and energy exactly, but does not conserve the deformation gradient. Within the Eulerian grid approaches, the immersed boundary is usually established and tracked via some

form of interface markers or advected as a solution variable such as a level-set. Utilizing LS-DYNA as the Lagrangian corrector step, the update represents the true location of the interface within the Eulerian grid, and conservation of the deformation gradient is no longer an issue. The Eulerian solution would then require subsequent correcting to establish consistency between the two formulations. At the interface this requires that kinematic and force equilibrium is maintained.

To achieve the aforementioned coupling, several challenges still require investigation. For example, two-way coupling with LS-DYNA appears achievable through the external user defined loading routines, especially for an ALE approach. However, within the corrector step, the transfer of loading information may require additional solution control options such that equilibrium is achieved during each iteration. Since both solution algorithms are explicit, and thus limiting the propagation of information within each domain, local strategies should be investigated to enforce equilibrium. In the presence of fracture, any void or crack within the structure will not be resolved at sufficient resolution to accurately model the resulting fluid behavior. Detailed studies, and potential use of phenomenological models, need to be explored in such instances. Additionally the use of local mesh adaptation should be considered when phenomenological models are inappropriate.

Finally, we would note that for blasts that are a moderate distance from the explosive, it is reasonable for the gas phase coupling to be performed using a one-way coupling approach. The validity of using a one-way coupling approach is largely due to the dramatic differences between the gas and structure material densities: Even with perfect momentum transfer, a factor of 100 difference in densities would imply a similar factor difference in the resulting material velocities. For the gas phase coupling, it is possible to estimate the error involved in making a one-way coupling assumption. Such a tool would allow an engineer to first perform a one-way coupled simulation and then assess from this simulation if a more expensive two-way coupling approach is needed. We would also note that while the gas phase densities drop dramatically with distance from the explosive event, the multiphase problem does not. Therefore, a compromise $1\frac{1}{2}$ way coupling may be reasonable in many cases. In this mode, the gas phase coupling would be treated one-way, while the particulate loading would be aware of the dynamic changes of the LS-DYNA simulation of the vehicle. If these techniques were combined with a robust tool for estimating approximation errors, engineers could quickly turn around risk assesments and determine if the approximations yielded too large an increase in uncertainties associated with predictions.

Disclaimer: Reference herein to any specific commercial company, product, process, or service by trade name, trademark, manufacturer, or otherwise, does not necessarily constitute or imply its endorsement, recommendation, or favoring by the United States Government or the Department of the Army (DoA). The opinions of the authors expressed herein do not necessarily state or reflect those of the United States Government or the DoA, and shall not be used for advertising or product endorsement purposes.

References

[3dcadbrowser.com_a] http://www.3dcadbrowser.com/preview.aspx?ModelCode=509

[3dcadbrowser.com_b] http://www.3dcadbrowser.com/preview.aspx?ModelCode=12486

[Adamik et al., 2004] Adamik, V., Trzcinski, W.A., and Vagenknecht, J. (2004). Investigation of the Behavior of Steel and Laminated Fabric Plates Under Blast Wave Load, Part II – Numerical Approach; 5th International Armament Conference, Waplewo, October 6-8, 2004.

[Baer and Nunziato, 1986a] Baer, M. and Nunziato, J. (1986a). A two-phase mixture theory for the deflagration-to-detonation transition (ddt) in reactive granular materials. *International Journal fo Multiphase Flow*, 12(6):851–889.

[Baer and Nunziato, 1986b] Baer, M. R. and Nunziato, J. W. (1986b). A two-phase mixture theory for the deflagration-to-detonation transition (ddt) in reactive granular materials. *Int J Multiphase Flow*, 12:861–889.

[Baum, et al., 2003] Baum, J.D. Mestreau, E. Luo, H. Löhner, R. Pelessone, D. and Charman, Ch. (2003). Modeling Structural Response to Blast Loading Using a Coupled CFD/CSD Methodology. *Proc. Des. An. Prot. Struct. Impact/ Impulsive/ Shock Loads (DAPSIL)*, Tokyo, Japan.

[Baum, et al., 2004a] Baum, J.D. Mestreau, E.L. Luo, H. Löhner, R. and Pelessone, D. (2004). Coupled cfd/csd modeling of weapon detonation/fragmentation in a tunnel. *Proc. MABS-18 Conf.*, Bad Reichenhall, Germany.

[Baum, et al., 2004b] Baum, J.D. Mestreau, E. Luo, H. Löhner, R. Pelessone, D. and Charman, Ch. (2004). Recent development of a coupled cfd/csd methodology using an embedded approach. *Proc. 24th Inter. Shock wave Symposium*, Beijing, China.

[Baum and Löhner, 2006] Baum, J.D. and Löhner, R. (2006). Coupled cfd/csd/dpm modeling of a cased charge detonation and fragmentation. *Proc. MABS-19 Conf.* Calgary, Canada.

[Baum, et al., 2006] Baum, J.D. Mestreau, E. Luo, H. Löhner, R. Pelessone, D. Giltrud, M.E. and Gran, J.K. (2006). Modeling of near-field blast wave evolution. *AIAA*-06-0191.

[Baum, et al., 2008] Baum, J.D. Soto, O.A. Giltrud, M.E. Löhner, R. Charman, C. Wolfson, J. Hegemeier G. and Arnett K. (2008). Modeling of steel plate response to blast loading using a coupled cfd/csd methodology. *Proc. MABS-20 Conf.*, Oslo, Norway.

[Baylot and Bevins, 2007] Baylot, J. T. and Bevins, T. L. (2007). Effect of responding and failing structural components on the airblast pressures and loads on and inside of the structure. *Computers & Structures*, 85(11-14):891–910.

[Bdzil et al., 1999] Bdzil, J. B., Menikoff, R., Son, S. F., Kapila, A. K., and Stewart, D. S. (1999). Two-phase modeling of deflagration-to-detonation transition in granular materials: A critical examination of modeling issues. *Physics of Fluids*, 11(2):378–402.

[Bergeron et al., 1998] Bergeron, D. M., Walker, R., and Coffey, C. (1998). Detonation of 100g anti-personnel mine surrogate charges in sand: A test case for computer code validation. Technical report DRES-SR-668, Defence Research Establishment Suffield, Canada.

[Blades and Newman, III, 2007a] Blades, E.L. and Newman III, J.C. (2007). Aeroelastic effects of spinning missiles. Proc. *of the 48th AIAA/ASME/ASCE/AHS/ASC Structures, Structural Dynamics, and Materials Conf.*, AIAA Paper 07-2243, Waikiki, HI.

[Blades and Newman, III, 2007b] Blades, E.L. and Newman III, J.C. (2007). Computational aeroelastic analysis of an unmanned aerial vehicle using U^2NCLE. *Proc. of the AIAA Dynamics Specialists Conf.*, AIAA Paper 07-2237, Waikiki, HI.

[Bonorchis and Nurick, 2009] Bonorchis, D. and Nurick, G.N. (2009). The influence of boundary conditions on the loading of rectangular plates subjected to localised blast loadings: Importance to numerical simulations. *Int. J. of Impact Engineering*, 36, 40-52.

[Borland, 1990] Borland, C.J. (1990). A multidisciplinary approach to aeroelastic analysis. *Computing Syst. Engr.*, 1, 197-209.

[Britan et al., 1995] Britan, A., Elperin, T., Igra, O., and Jiang, J.P. (1995). Acceleration of a sphere behind planar shock waves. *Experiments in Fluids*, 20:84–90.

[Buning et al., 2004] Buning, P.G., Gomez, R.J., and Scallion, W.L. (2004). CFD applications for simulation of wing-body stage separation. AIAA Paper 04-4838.

[Cebral and Löhner, 1997] Cebral, J.R. and Löhner, R. (1997). Conservative load projection and tracking for fluid–structure problems. *AIAA J.*, 35, 687-692.

[Chan, 2004] Chan, S. (2004). *Nonlinear fluid-structure interaction in a flexible shelter under blast loading*. PhD Dissertation, Virginia Polytechnic Institute and State University.

[Chen et al., 2008] Chen, H.C., Lee, S.K., and Seah, A.K. (2008). Overset grid CFD applications for challenging offshore hydrodynamic problems, ABS Technical Paper.

[Clutter and Belk, 2002] Clutter, J. and Belk, D. (2002). Simulation of detonation wave interaction using an ignition and growth model. *Shock Waves*, 12(3):251–263.

[Clutter and Stahl, 2004] Clutter, J. K. and Stahl, M. (2004). Hydrocode simulations of air and water shocks for facility vulnerability assessments. *Journal of Hazardous Materials*, 106A:9–24.

[Coffey et al., 1998] Coffey, C. G., Roseveare, J., and Torrance, K. (1998). Development of the DRES large scale facility. Technical Report DRES CR 2000-102, Defence Research Establishment Suffield, Canada.

[Colella and Glaz, 1985] Colella, P. and Glaz, H. (1985). Efficient solution algorithms for the Riemann problem for real gases. *Journal of Computational Physics*, 59:264–289.

[Einfeldt, 1988] Einfeldt, B. (1988). On godunov-type methods for gas dynamics. *Journal of Computational Physics*, 25:294-318.

[Ergun, 1952] Ergun, S. (1952). Fluid flow through packed columns. *Chem. Engr. Prog.*, 48:89.

[Fairlie and Bergeron, 2002] Fairlie, G. and Bergeron, D. (2002). Numerical simulation of mine blast loading on structures. In *17th Military Aspects of Blast Symposium*, Las Vegas, Nevada.

[Fallet, 2008] Fallet, R. (2008). Mine explosion and blast effect on vehicle analysis of the potential damage on passengers. In *2nd European HyperWorks Technology Conference*, Strasbourg.

[Fan et al., 2007] Fan, B. C., Chen, Z. H., Jiang, X. H., and Li, H. Z. (2007). Interaction of a shock wave with a loose dusty bulk layer. *Shock Waves*, 16:179–187.

[Farhat, et al., 1998] Farhat, C., Lesoinne, M. and LeTallec, P. (1998). Load and motion transfer algorithms for fluid/structure interaction problems with nonmatching discrete interfaces:

Momentum and energy conservation, optimal discretization and application to aeroelasticity. *Comput. Methods Appl. Mech. Engrg*., 157, 95-114.

[Fiserova, 2006] Fiserova, D. (2006). *Numerical analysis of buried mine explosions with emphasis on effect of soil properties on loading*. PhD thesis, Cranfield University.

[Freiwald and Axford, 1975] Freiwald, D. and Axford, R. (1975). Approximate spherical blast theory including source mass. *Journal of Applied Physics*, 46(3):1171–1174.

[Frost et al., 2007] Frost, D. L. ., Omthanalai, C., Zarei, Z., Tanguay, V., and Zhang, F. (2007). Particle momentum effects from the detonation of heterogeneous explosive. *Journal of Applied Physics*, 101:101.

[Galiev, 1996] Galiev, U. (1996). Experimental observations and discussions of counter-intuitive behavior of plates and shallow shells subjected to blast loading. *Int. J. of Impact Engineering*, 18, 783-802.

[Gidaspow, 1994] Gidaspow, D. (1994). *Multiphase Flow and Fluidization*. Academic Press.

[Grujicic et al., 2006] Grujicic, M., Pandurangan, B., and Cheeseman, B. A. (2006). The effect of degree of saturation of sand on detonation pheno mena associated with shallow-buried and ground-laid mines. *Shock and Vibration*, 13:41–61.

[Grujicic et al., 2007a] Grujicic, M., Pandurangan, B., Haque, I., Cheeseman, B., Roy, W., and Skaggs, R. (2007a). Computational analysis of mine blast on a commercial vehicle structure. *Multidiscipline Modeling in Materials and Structures*, 3(4):431–460.

[Grujicic et al., 2007b] Grujicic, M., Pandurangan, B., Huang, Y., n, B. A. C., Roy, W. N., and Skaggs, R. R. (2007b). Impulse loading resulting from shallow buried explosives in w ater-saturated sand. *Proceedings of the Institution of Mechanical Engineers, Part L: Journal of Materials: Design and Applications*, 221(1):21–35.

[Grujicic et al., 2008a] Grujicic, M., Arakere, G., Nallagatla, H. K., Bell, W. C., and Haque, I. (2008a). Computational investigation of blast survivability and off-road performance of an up-armored high-mobility multi-purpose wheeled vehicle (hmmwv). *Journal of Automobile Engineering* (in press).

[Grujicic et al., 2008b] Grujicic, M., Bell, W. C., Arakere, G., and Haque, I. (2008b). Finite element analysis of the effect of up-armoring on the off-road braking and sharp-turn performance of a high-mobility multi-purpose wheeled vehicle (hmmwv). *Journal of Automobile Engineering* (in press).

[Grujicic et al., 2008c] Grujicic, M., Bell, W. C., Marvi, H., Haque, I., Cheeseman, B. A., Roy, W. N., and Skaggs, R. R. (2008c). A computational analysis of survivability of a pick-up truck subjected to mine detonation loads. *Multidiscipline Modeling in Materials and Structures* (in press).

[Grujicic et al., 2008d] Grujicic, M., Pandurangan, B., Mocko, G., an d B. A. Cheeseman2, S. H., Roy, W. N., and Skaggs, R. R. (2008d). A combined multi-material euler/lagrange computational analysis of blast loading resulting from detonation of buried landmines. *Multidiscipline Modeling in Materials and Structures*, 4(2):105–124.

[Gupta, 1999] Gupta, A. (1999). Estimation of vehicle floor plate loading and response to detonation of a mine shallow-buried in dry sand and wet tuff. In *US Army Ground Vehicle Survivability Symposium*, Monterey, California.

[Gupta, 2001] Gupta, A. D. (September 2001). Modeling and analysis of a 3-d asymmetric mine-soil-hull floor interaction problem with mine buried in dry and wet sand. Technical report, Army Research Laboratory.

[Harris and Amsden, 1994] Harris, S. E. and Amsden, A. A. (1994). Slitons, solitary wave, and voidage disturbances in gas-fluidized beds. *J. Fluid Mech.*, 266:243.

[Hayhurst et al., 1996] Hayhurst, C. J., Clegg, R. A., Francis, N. J., Birnbaum, N. K., and van den Berg, B. (1996). Numerical simulation of explosive and impact loading and response using autodyn-3d and autoreagas. In *Asia-Pacific Conference on Shock and Impact Loads in Structures*, Singapore.

[Hlady, 2004] Hlady, S. (2004). Effect of soil parameters on land mine blast. In *18th Military Aspects of Blasts and Shock Conference*.

[Honlinger et al., 1996] Honlinger, M., Glauch, U., and Steger, G. (1996). Modeling and simulation in the design process of armored vehicles. In *RTO AVT Symposium on Reduction of Military Vehicle Acquisition Time and Cost through Advanced Modeling and Virtual Simulation*, Paris, France.

[Hyde, 1991] Hyde, D. W. (1991). Conwep: Conventional weapons effects program. Technical report, Waterways Experiment Station, Vicksburg.

[Ingra and Takayama, 1993] Ingra, O., and Takayama, K. (1993). Shock tube study of the drag coefficient of a sphere in a non-stationary flow. *Proc. R. Soc*., 143:231–247.

[Jacinto, et al., 2001] Jacinto, A.C. Ambrosini, R.D. and Danesi, R.F. (2001). Experimental and computational analysis of plates under air blast loading. *Int. J. of Impact Engineering*, 25, 927-947.

[Jacinto et al., 2002] Jacinto, A. C., Ambrosini, R. D., and Danesi, R. F. (2002). Dynamic response of plates subjected to blast loading. *Structures and Buildings*, 152(3):269–276.

[Jaiman, et al., 2006] Jaiman, R. K., Jiao, X., Geubekke, P.H., and Loth, E. (2006). Conservative load transfer along curved fluid-solid interface with non-matching meshes. *J. of Computational Physics*, 218, 372-397.

[Janus, 1989] Janus, J. Mark (1989), *Advanced 3d cfd algorithm for turbomachinery*, PhD Dissertation, Mississippi State University.

[Janus and Newman, 2000] Janus, J.M., and Newman III, J.C. (2000). Aerodynamic and thermal design optimization for turbine airfoils. AIAA Paper 00-0840, Reno, NV.

[Johnson et al., 2008] Johnson, G., Gerlach, C., T.J. Holmquist, K. D., Williams, E., and Fox, D. (2008). Lagrangian computational approach for modeling air, soil, fragmentation, and structural interactions due to blast loading. In *Military Aspects of Blast and Shock, MABS20*, Oslow, Norway.

[Kambouchev et al., 2006] Kambouchev, N., Noels, L., and Radovitzky, R. (2006). Nonlinear compressibility effects in fluid-structure interaction and their implication on the air-blast loading of structures. *Journal of Applied Physics*, 100(063519).

[Kambouchev et al., 2007a] Kambouchev, N., Noels, L., and Radovitzky, R. (2007a). Numerical simulation of the fluid-structure interaction between air blast waves and free-standing plates. *Computers & Structures*, 85(11-14):923–931.

[Kambouchev et al., 2007b] Kambouchev, N., Radovitzky, R., and Noels, L. (2007b). Fluid-structure interaction effects in the dynamic response of free-standing plates to uniform shock loading. *Journal of Applied Mechanics*, 74(2):1042–1045.

[Kim and Han, 2006] Kim, D. K. and Han, J. H. (2006). Establishment of gun blast wave model and structural analysis for blast load. *Journal of Aircraft*, 43(4):1159–1168.

[Langdon and Suhleyer, 2005] Langdon, G.S. and Suhleyer, G.K. (2005). Inelastic deformations of profiled stainless steel blast wall panels: Experimental investigation. *Int. J. of Impact Engineering*, 31, 341-369.

[Lee and Tarver, 1980] Lee, E. and Tarver, C. (1980). Phenomenological model of shock initiation in heterogeneous explosives. *Physics of Fluids*, 23(12):2362–2372.

[Liang and Hsu, 2001] Liang, S.M. and Hsu, J.L. (2001). Numerical study of cylindrical blast wave propagation and reflection. *AIAA Journal*, 39, 1152-1158.

[Lijewski and Suhs, 1994] Lijewski, L.E., and Suhs, N.E. (1994). Time-accurate computational fluid dynamics approach to transonic store separation trajectory prediction, *Journal of Aircraft*, 41(4):886–891.

[Liou and Takayama, 2004] Liou, M. and Takayama, K. (2004). High mach and low Reynolds numbers flow past micro spheres. In *Symposium on Interdisciplinary Shock Wave Research, Sendai, Japan*, pages 310–323.

[Löhner and Baum, 1992] Löhner, R. and Baum, J.D. (1992). Adaptive h-refinement on 3-d unstructured grids for transient problems. *Int. J. Num. Meth. Fluids*, 8,1135-1149.

[Löhner et al., 1999] Löhner, R., Yang, C., Baum, J., Luo, H., Pelessone, D., and Charman, C. (1999). The numerical simulation of strongly unsteady flow with hundreds of moving bodies. *Int. J. Numer. Meth. Fluids*, 31:113–120.

[Löhner, 2004a] Löhner, R. (2004a). Blast mitigation: A co-evolutionary approach. paper presented at the Built Infrastructure Security Workshop (BIS'2004), Arlington, VA.

[Löhner, et al., 2004b] Löhner, R. Baum, J.D. Charman, C. and Pelessone, D. (2004b). Prediction of blast effects on structures using coupled, first-principle cfd and csd codes. *J. of the Japan Society for Computational Engineering and Science (JSCES)* 9, 3, 30-37. [in Japanese]

[Löhner, et al., 2004c] Löhner, R. Baum, J.D. and Rice, D. (2004c). Comparison of coarse and fine mesh 3-d euler predictions for blast loads on generic building configurations. *Proc. MABS-18 Conf.*, Bad Reichenhall, Germany.

[Löhner et al., 2008] Löhner, R., Cebral, J. R., Camelli, F. E., Appanaboyina, S., Baum, J. D., Mestreau, E. L., and Soto, O. A. (2008). Adaptive embedded and immersed unstructured grid techniques. *Computer Methods in Applied Mechanics and Engineering*, 197(25-28):2173–2197.

[Louca and Pan, 1998] Louca, L.A. and Pan, Y.G. (1998). Response of stiffened and unstiffened plates subjected to blast loading. *Engineering Structures*, 20, 12, 1079-1086.

[Lottati et al., 1996] Lottati, I., Eidelman, S., Dillon, J., Sergi, S., and Sousk, S. (1996). Design of blast deflectors for a mine resistant vehicle by cfd/csd simulations. *ASME Publications Pressure Vessels and Piping Division, Structures under Extreme Loading Conditions*, 325:51–61.

[LS-DYNA User Manual, 2007] LS-DYNA User Manual, Version 971, Livermore Software Technology Corporation, May 2007.

[Lu and Wang, 2006] Lu, Y. and Wang, Z. (2006). Characterization of structural effects from above-ground explosion using coupled numerical simulation. *Computers & Structures*, 84(28):1729–1742.

[Luke and Cinnella, 2007] Luke, E. and Cinnella, P. (2007). Numerical simulations of mixtures of fluids using upwind algorithms. *Computers and Fluids*, 36:1547–1566.

[Mader, 1979] C.L. Mader, *Numerical Modeling of Detonations*, University of California Press, California, 1979

[Martin and Link, 2003] Martin, L. and Link, R. (2003). Numerical characterization of mine blast loading. Technical report, Defence Research and Developement Canada.

[Menikoff, 2006] Menikoff, R. (2006). Comparison of constitutive models for pbx 9501. Technical report, Los Alamos National Lab. Rep. No. LA-UR-06-2355.

[Miller and Colella, 2001] Miller, G. and Colella, P. (2001). A high-order eulerian Godunov method for elastic-plastic flows in solids. *Journal of Computational Physics*, 167:131–176.

[Murman et al., 2003] Murman, S.M., Aftosmis, M.J., and Berger, M.J. (2003). Simulation of 6-DOF motion with a Cartesian method. AIAA Paper 03-1246.

[Neuberger, et al., 2009] Neuberger, A. Peles, S. and Hel D.R. (2009) . Springback of circular clamped armor steel plates subjected to spherical air-blast loading. *Int. J. of Impact Engineering*, 36, 53-60.

[Newman, III, 1997] Newman III, J.C. (1997). *Integrated multidisciplinary design optimization using discrete sensitivity derivatives for geometrically complex aeroelastic configurations*. PhD Dissertation, Virginia Polytechnic Institute and State University.

[Ofengeim and Drikakis, 1997] Ofengeim, D. Kh., and Drikakis, D. (1997). Simulation of blast wave propagation over a cylinder. *Shock Waves*, 7, 305-317.

[Pan and Louca, 1999] Pan, Y.G. and Louca, L.A. (1999). Experimental and numerical studies on the response of stiffened plates subjected to gas explosions. *J. of Construction Steel Research*, 52, 171-193.

[Pelessone and Charman, 1998] Pelessone, D. and Charman, C.M. (1998). A general formulation of a contact algorithm with node/face and edge/edge contacts. *1998 ASME Pressure Vessel and Piping Conf.*, San Diego, Ca.

[Pember et al., 1995] Pember, R.B., Bell, J.B., Colella, P., Crutchfield, W.Y., and Welcome, M.L. (1995). An adaptive Cartesian grid method for unsteady compressible flow in irregular regions, *J. Comp. Phys.*, 120(1):278–304.

[Powers et al., 1990] Powers, J. M., Stewart, D. S., and Krier, H. (1990). Theory of two-phase detonations part i: Modeling. *Combust. Flame*, 80:264–279.

[Remennikov and Rose, 2005] Remennikov, A. M. and Rose, T. A. (2005). Modeling blast load on building in complex city geometries. *Computers & Structures*, 83(27):2197–2205.

[Rice, et al., 2006] Rice, D. Baum, J.D. Löhner, R. and Pelessone, D. (2006). Coupled cfd/csd/dpm modeling of wall response to blast loading. *Proc. MABS-19 Conf.* Calgary, Canada.

[Rogue et al., 1998] Rogue, X., Rodriguez, G., Haas, J. F., and Saurel, R. (1998). Experimental and numerical investigation of the shock-induced fluidization of a particles bed. *Shock Waves*, 8:29–45.

[Rose et al., 2005a] Rose, T. A., Smith, P. D., and Brittle, M. (2005a). Analysis of a generic cityscape using an adaptive cfd code. In *12th International Symposium on Interaction of the Effects of Munitions with Structures*, New Orleans, LA.

[Rose et al., 2005b] Rose, T. A., Smith, P. D., and Forth, S. A. (2005b). Development of an adaptive mesh cfd code for high explosive blast simulation. In *12th International Symposium on Interaction of the Effects of Munitions with Structures*, New Orleans, LA.

[Saito et al., 2003] Saito, T., Marumoto, M., and Takayama, K. (2003). Numerical investigations of shock waves in gas-particle mixtures. *Shock Waves*, 12:299–322.

[Saurel et al., 1992] Saurel, R., Larini, M., and Loraud, J. C. (1992). Ignition and growth of a detonation by high energy plasama. *Shock Waves*, 2:19.

[Saurel and Massoni, 1998] Saurel, R. and Massoni, J. (1998). On Riemann-problem-based methods for detonations in solid energetic materials. *International Journal for Numerical Methods in Fluids*, 26(1):101–121.

[Sheta, et al., 1999] Sheta, E.F. Siegel, J.M. Golos, F.N. and Harrand, V.J. (1999). Twin-tail buffet simulation using a multi-disciplinary computing environment (mdice). CEAS/AIAA/ICASE/NASA International Forum on Aeroelasticity and Structural Dynamics, Williamsburg, VA.

[Showichen et al., 2005] Showichen, A., Hameed, A., Iremonger, M. J., and Hetherington, J. G. (2005). Simulation of plate structure subjected to anti-tank mine blast. *Journal of Battlefield Technology*, 8(1):1–7.

[Silver, 2006] Silver, P. L. (2006). Blast overpressure measurement for cfd model validation in the development of large caliber gun systems. In *41st Annual Armament Systems: Guns and Missile Systems Conference and Exhibition*.

[Smith et al., 2000] Smith, P. D., Whalen, G. P., Feng, L. J., and Rose, T. A. (2000). Blast loadings on buildings from explosions in city streets. *Structures & Buildings*, 146(1):47–55.

[Soto, et al., 2008] Soto, O.A. Baum, J.D. Giltrud, M.E. and Löhner, R. (2008). Modeling of an explosively formed projectile (efp) using a coupled cfd/csd methodology. *Proc. MABS-20 Conf.*, Oslo, Norway.

[Sun et al., 2004] Sun, M., Saito, T., Takayama, K., and Tanno, H. (2004). Unsteady drag on a sphere by shock wave loading. *Shock Waves*.

[Susuki et al., 2005] Suzuki, T., Sakamura, Y., Igra, O., Adachi, T., Kobayashi, S., Kotani, A., Funawatashi, Y. (2005). Shock tube study of particles' motion behind a planar shock wave. *Meas. Sci. Technol*., 16:2431–2436.

[Swensen et al., 2006] Swensen, D. A., Denison, M. K., Guilkey, J., Harman, T., and Goetz, R. (2006). A software framework for blast event simulation. Technical report, Reaction Engineering International. ADM002075.

[Tai et al., 2007a] Tai, C. H., Liew, K. M., and Zhao, Y. (2007a). Numerical simulation of 3d fluid-structure interaction flow using an immersed object method with overlapping grids. *Computers & Structures*, 85(11-14):749–762.

[Tai et al., 2007b] Tai, C. H., Teng, J. T., Lo, S. W., and Liu, C. W. (2007b). A numerical study in the interaction of blast wave with a wheeled armoured vehicle. *International Journal of Vehicle Design*, 45(1-2):242–265.

[Tang, 2007] Tang, J. (2007). Cfd simulation of blast in an internal geometry using a cartesian cell code. In *16th Australasian Fluid Mechanics Conference*, Gold Coast, Australia.

[Tanno et al., 2003] Tanno, H., Itoh, K., Saito, T., Abe, A., and Takayama, K. (2003). Interaction of a shock with a sphere suspended in a vertical shock tube. *Shock Waves*, 13:191–200.

[Tanno et al., 2004] Tanno, H., Itoh, K., Saito, T., Abe, A., and Takayama, K. (2004). Shock wave interaction with a sphere in a shock tube. In *Symposium on Interdisciplinary Shock Wave Research*, Sendai, Japan. http://rainbow.ifs.tohoku.ac.jp/ iswi/ISISW/ISISWtanno.pdf.

[Tarver et al., 1997] Tarver, C., Kury, J., and Breithaupt, R. (1997). Detonation waves in triaminotrinitrobenzene. *Journal of Applied Physics*, 82(8):3771–3782.

[Taylor, 1950a] Taylor, G. (1950a). The formation of a blast wave by a very intense explosion. i. Theoretical discussion. *Proceedings of the Royal Society of London. Series A, Mathematical and Physical Sciences*, 201(1065):159–174.

[Taylor, 1950b] Taylor, G. (1950b). The formation of a blast wave by a very intense explosion. ii. The atomic explosion of 1945. *Proceedings of the Royal Society of London. Series A, Mathematical and Physical Sciences*, 201(1065):175–186.

[the3dstudio.com] http://www.the3dstudio.com/product_details.aspx?id_product=9453

[Trzcinski and Cudzilo, 2004] Trzcinski, W.A. and Cudzilo, S. (2004). Investigation of the behavior of steel and laminated fabric plates under blast wave load, part i: Experimental approach. *Vth International Armament Conf.*, Waplewo.

[Wang 2001] Wang, J. (2001). Simulation of landmine explosion using LS-DYNA-3D software: Benchmark work of simualtion of explosion in soil and air. Technical report DSTO-TR-

1168, DSTO, Aeronautical and Maritime Research Laboratory, Melbourne, Australia, June 2001.

[Wang et al., 2004] Wang, Z., Hao, H., and Lu, Y. (2004). A three-phase soil model for simulating stress wave propagation due to blast loading. *International Journal fro Numerical and Analytical Methods in Geomechanics*, 28:33–56.

[Weston, et al., 1994] Weston, R.P. Townsend, J.C. Eidson, T.M. and Gates, R.L. (1994). A distributed computing environment for multidisciplinary design. AIAA Paper 94-4372.

[Whirley and Hallquist, 1991] Whirley, R.G. and Hallquist, J.O. (1991). DYNA3D: A nonlinear explicit, three-dimensional finite element code for solid and structural mechanics – user manual. UCRL-MA-107254.

[Williams, 2002a] Williams, K. (2002a). Numerical simulation of light armoured vehicle occupant vulnerability to anti-vehicle mine blast. In *7th International LS-DYNA Users Conference*, Dearborn, Michigan.

[Williams, 2002b] Williams, K. (2002b). Validation of a loading model for simulating blast mine effects on armoured vehicles. In *7th International LS-DYNA Users Conference*, Dearborn, Michigan.

[Woodson and Hall, 2008] Woodson, Stanley (DHS Blast Mitigation Research Program Manager) and Hall, Robert (Chief, Geosciences and Structures Division) (2008) – private comunication, ERDC, Vicksburg, MS.

[Wu et al., 2004] Wu, C., Hao, H., Lu, Y., and Sun, S. (2004). Numerical simulation of structural responses on a sand layer t o blast induced ground excitations. *Computers and Structures*, 82:799–814.

[Xu and Lu, 2006] Xu, K. and Lu, Y. (2006). Numerical simulation study of spallation in reinforced concrete plates subjected to blast loading. *Computers & Structures*, 84(5-6):431 – 438.

[Zhang et al., 2001] Zhang, F., Frost, D. L., Thibault, P. A., and Murray, S. B. (2001). Explosive dispersal of solid particles. *Shock Waves*, 10:431–443.

[Zhang et al., 2008] Zhang, D.Z., Zou, Q., VanderHeyden, W.B., Ma, X. (2008). Material point method applied to multiphase flow, *J. Comp. Physics*, 227:3159-3173.